Nonlinear Dynamics of Circular Plates under Electrical Loadings for Capacitive Micromachined Ultrasonic Transducers (CMUTs)

Gregory W. Vogl

Dissertation submitted to the Faculty of the Engineering Science and Mechanics Department of Virginia Polytechnic Institute and State University in partial fulfillment of the requirements for the degree of

Doctor of Philosophy
in
Engineering Mechanics

Ali H. Nayfeh, Chairman
Scott L. Hendricks
Daniel J. Inman
Liviu Librescu
Saad A. Ragab

December 5, 2006
Blacksburg, Virginia

Keywords: CMUT, Macromodel, Pull-in, Primary Resonance, Nonlinear Dynamics

Nonlinear Dynamics of Circular Plates under Electrical Loadings for Capacitive Micromachined Ultrasonic Transducers (CMUTs)

Gregory W. Vogl

(ABSTRACT)

We created an analytical reduced-order model (macromodel) for an electrically actuated circular plate with an in-plane residual stress for applications in capacitive micromachined ultrasonic transducers (CMUTs). After establishing the equations governing the plate, we discretized the system by using a Galerkin approach. The distributed-parameter equations were then reduced to a finite system of ordinary-differential equations in time.

We solved these equations for the equilibrium states due to a general electric potential and determined the natural frequencies of the axisymmetric modes for the stable deflected position. As expected, the fundamental natural frequency generally decreases as the electric forcing increases, reaching a value of zero at pull-in. However, strain-hardening effects can cause the frequencies to increase with voltage. The macromodel was validated by using data from experiments and simulations performed on silicon-based microelectromechanical systems (MEMS). For example, the pull-in voltages differed by about 1% from values produced by full 3-D MEMS simulations.

The macromodel was then used to investigate the response of an electrostatically actuated clamped circular plate to a primary resonance excitation of its first axisymmetric mode. The method of multiple scales was used to derive a semi-analytical expression for the equilibrium amplitude of vibration. The plate was found to always transition from a hardening-type to a softening-type behavior as the DC voltage increases towards pull-in.

Because the response of CMUTs is highly influenced by the boundary conditions, an updated reduced-order model was created to account for more realistic boundary conditions. The electrode was still considered to be infinitesimally thin, but the electrode was allowed to have general inner and outer radii. The updated reduced-order model was used to show how sensitive the pull-in voltage is with respect to the boundary conditions. The boundary parameters were extracted by matching the pull-in voltages from the macromodel to those from finite element method (FEM) simulations for CMUTs with varying outer and inner radii.

The static behavior of the updated macromodel was validated because the pull-in voltages for the macromodel and FEM simulations were very close to each other and the extracted boundary parameters were physically realistic.

A macromodel for CMUTs was then created that includes both the boundary effects and an electrode of finite thickness. Matching conditions ensured the continuity of displacements, slopes, forces, and moments from the composite to the non-composite regime of the CMUT. We attempted to validate this model with results from FEM simulations. In general, the center deflections from the macromodel fell below those from the FEM simulation, especially for relatively high residual stresses, but the first natural frequencies that accompany the deflections were very close to those from the FEM simulations. Furthermore, the forced vibration characteristics also compared well with the macromodel predictions for an experimental case in which the primary resonance curve bends to the right because the CMUT is a hardening-type system.

The reduced-order model accounts for geometric nonlinear hardening, residual stresses, and boundary conditions related to the CMUT post, allows for general design variables, and is robust up to the pull-in instability. However, even more general boundary conditions need to be incorporated into the model for it to be a more effective design tool for capacitive micromachined ultrasonic transducers.

Dedication

In loving memory of my grandpa, William H. Gibbs

Acknowledgments

Although this section is titled 'Acknowledgments', I am not going to just acknowledge the people who helped me to complete this dissertation. No. My advisor, committee, family, and friends deserve more than that; they all deserve my deepest thanks.

I wish to thank Dr. Ali H. Nayfeh, my advisor, who probably believed in me more than I did during this work. He was extremely patient with me during those private ordeals in my life when his kind-heartedness and understanding was needed much more than he knew. Yes, Dr. Nayfeh was always willing to help me with my work, but more importantly, he served as an example. People may see Dr. Nayfeh as a prolific writer and accomplished man, a genius whose work supercedes that of the combined efforts of many others. It is true. However, I see Dr. Nayfeh as a great man, not because of his works alone, but mainly because of his gentleness, patience, generosity, and self-control. He has been an example of how these fruits can bear forth in a life of discipline and honor. Thank you, Dr. Nayfeh.

I also wish to thank my other advisory committee members, Drs. Scott L. Hendricks, Daniel J. Inman, Liviu Librescu, and Saad A. Ragab, for their encouragement and assistance. Particularly, I wish to thank Drs. Hendricks, Librescu, and Ragab for teaching me with such commitment, congeniality, and care during my many years here in the ESM Department at Virginia Tech.

In fact, I have to extend my thanks to all professors, but especially to Drs. Glenn Kraige and Mark S. Cramer, my senior thesis and Master's advisors, respectively. I was blessed to have been taught very technical subjects by the most brilliant professors. However, Dr. Kraige and Dr. Cramer are more than professors; they are friends who deserve my thanks for guiding me in my career and private life.

Special thanks go to all other students who have studied with me under Dr. Nayfeh in the Nonlinear Dynamics Lab, namely his former students (Drs. Khalid Alahaza, Konda Chevva, Mohammed Daqaq, Waleed Faris, Pramod Malatkar, Nader Nayfeh, Mohammad Younis, and Xiaopeng Zhao), former postdocs (Drs. Eihab Abdel-Rahman and Haider Arafat) and current students (Messrs. Imran Akhtar, Bashar Hammad, and Osama Marzouk). I have enjoyed countless conversations with them and appreciate their support and friendship. And of course, nothing would be organized or accomplished if it were not for the expertise of Mrs. Sally Shrader. Thanks, Sally, for all the help.

My other friends who have supported me during my life in Blacksburg deserve many thanks, especially Dr. Leslie A. Garay for his friendship, unbounded generosity, and support, particularly in my darkest moments, and Mrs. Margaret Olsen for her unwavering kindness and for being my grandmother here in Blacksburg. They are more than friends; they are family. I could not have finished this work without their love always catching me when I was falling.

Lastly, my family deserves so much thanks that I cannot express it in words but perhaps in tears. To my Mom and Dad, Mr. and Mrs. Walter and Faith Vogl, you have always given me everything without asking for anything in return. Thank you for your sacrificial and unbounded love, prayers, and emotional and financial support that has sustained me. To my brothers and sister, Matt, Grant and Alexis, what would life be without you all? I do not want to know. To my grandparents, Mrs. Marjorie Gibbs and Mrs. Berta Vogl, and to all my family, I love you and thank you for your love.

Contents

List of Figures

List of Tables

Chapter 1

Introduction and Literature Review

1.1 Motivation

Microplates are commonly piezoelectrically or electrostatically actuated for various resonance applications. For example, piezoelectric resonance applications have ranged from micropumps (Saggere et al., 2000) and micromachined ultrasonic transducers (Perçin and Khuri-Yakub, 2001) to fluid density sensors (Crescini et al., 1998). Micromachined ultrasonic transducers (MUTs) have many applications, such as generating and detecting ultrasound for 3-D imaging (Caronti et al., 2002b). Electrostatic (or capacitive) actuation has been used more extensively than piezoelectric actuation for MUTs, with capacitive micromachined ultrasonic transducers (CMUTs) created for both air (Caliano et al., 2000; Caronti et al., 2002b; Ergun et al., 2002; Haller and Khuri-Yakub, 1994, 1996; Huang et al., 2003a,b; Ladabaum et al., 1995; Oppenheim et al., 2003; Suzuki et al., 1989; Yaralioglu et al., 2003) and immersion applications (Huang et al., 2002; Jin et al., 1998b; Xuecheng Jin et al., 2001).

MUTs based on electrostatic actuation are more advantageous than piezoelectrically actuated transducers. First, piezoelectric materials have mechanical impedances much larger than the acoustic impedance of air, making piezoelectric air transducers inefficient (Ladabaum et al., 1995). On the other hand, the mechanical impedances of thin membranes in electrostatic devices are much smaller than those of fluids in a wide frequency range. Consequently, electrostatic actuation enables better coupling with air and converts otherwise resonant CMUTs into wideband frequency transducers for immersion applications in which

acoustical loading overdamps the membranes (Huang et al., 2003b). Second, CMUTs can be produced with standard integrated circuit (IC) processes with an accuracy that is difficult to attain with lead zirconium titanate transducers (PZTs) (Eccardt et al., 1996). Therefore, CMUTs have the advantages of IC processing technology, like parallel processing and batch fabrication (Ergun et al., 2002). It is then easier to make transducer arrays from CMUTs than from PZTs. CMUTs can also operate in a temperature range wider than that in which piezoelectric devices can operate (Eccardt et al., 1996). In general, micromachined transducers with electrostatic actuation can have low impedance mismatch, low energy density, and low cost relative to piezoelectric transducers (Caliano et al., 2000).

Furthermore, circular microplates are commonly electrically actuated in CMUTs utilized in both air (Caronti et al., 2002b; Haller and Khuri-Yakub, 1994, 1996; Hansen et al., 2000; Huang et al., 2003a; Jin et al., 1998a; Ladabaum et al., 1995; Yaralioglu et al., 2001, 2003) and liquids (Ergun et al., 2002; Jin et al., 1998a; Ladabaum et al., 1996; Xuecheng Jin et al., 2001). The circular microplate is typically composed of a single silicon crystal or silicon nitride (SiNi) and is suspended above a heavily doped silicon bulk material, as seen in Figure 1.1(a). When a bias voltage is applied between a deposited conductive material (the top electrode) on the microplate and the bulk base (the bottom electrode), the attractive electrostatic forces cause the microplate to deflect downward. If a small alternating voltage is added to the bias voltage, relatively large displacements can be created when the frequency is near resonance, causing significant sound generation (Ladabaum et al., 1995), especially when multiple cells are used in an array, such as the device in Figure 1.1(b).

The CMUT converts electrical energy into mechanical energy and vice versa (Yaralioglu et al., 2003), and a good design requires a large displacement from the bias voltage for efficient energy coupling between the circular microplate and the air (Haller and Khuri-Yakub, 1994). The microplate can also be deflected by ambient pressure if the cavity beneath the microplate is vacuum sealed (Huang et al., 2003a), which is necessary for immersion applications. However, optimum energy coupling is achieved when the plate is near the structural instability known as 'pull-in' (Yaralioglu et al., 2003), where the largest stable plate deflection occurs. Beyond this point, the plate snaps onto the substrate.

Many resonance applications demand better understanding of CMUT behaviors, espe-

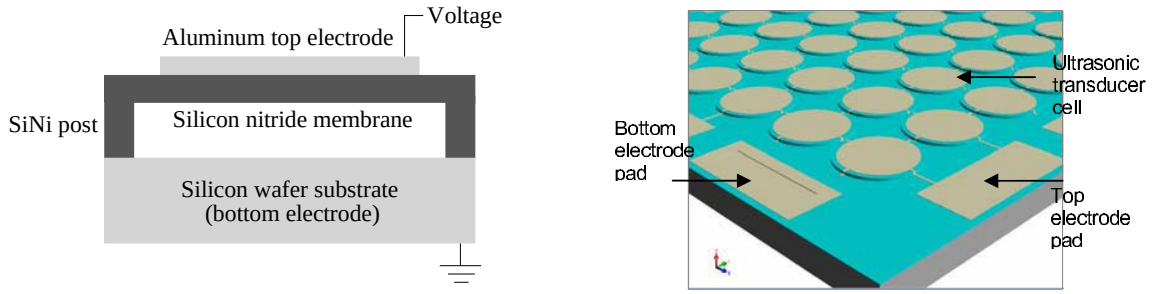

(a) Typical electrostatic cell

(b) Cell array (from Teng and Hariz (2006))

Figure 1.1: Schematics of a few CMUT devices.

cially near the 'pull-in' instability. Most researchers use finite element method (FEM) simulations, analytical plate or membrane models, or lumped-element models to analyze resonating circular microstructures. These approaches have their respective flaws. Most FEM simulations are computationally inefficient or breakdown near pull-in of electrostatically actuated structures, and membrane models ignore plate bending, which is needed for bending-dominated microstructures. Furthermore, analytical plate or plate-membrane models usually ignore nonlinearities (Yu and Balachandran, 2005), such as those created by large plate deflections, so linear theories may produce inaccurate results. Then, a geometrically nonlinear elastic analysis needs to be utilized (Li and Aluru, 2001).

1.2 Literature Review of CMUTs

A brief review follows of the various recent investigations of CMUTs.

1.2.1 Experimental Investigations

There are many cells in a transducer array, and the elements are used to make CMUT arrays. The basic physical structure of an immersion CMUT is a solid silicon plate, with fluid on either one or both sides, that is bonded to a solid integrated circuit silicon plate. Many applications, especially immersion imaging applications, require improved CMUTs in terms of individual device performance and array behavior. Cross coupling between elements is one of the most important factors affecting the performance of an imaging array (Larson, 1981).

Xuecheng Jin et al. (2001) experimentally characterized a 275-μm$\times$ 5600-μm 1-D CMUT array element and the results were found to be in agreement with theoretical predictions from an equivalent circuit model. The transducer had a 0.28-fm/$\sqrt{\text{Hz}}$ displacement sensitivity as a receiver and produced 5 kPa/V of output pressure with a 100% fractional bandwidth at 3 MHz as a transmitter with a 35 bias voltage. Xuecheng Jin et al. also observed Lamb waves propagating in the silicon wafer and Stoneley-type waves propagating at the fluid-silicon wafer interface. Lamb waves, which refer to the elastic modes of propagation in a solid plate with free boundaries, were excited by the stresses applied on the silicon surface at the edges where the CMUT membranes are anchored, while Stoneley waves traveled along the front surface of the CMUT arrays in all media.

Caliano et al. (2002) changed an active piezoelectric array into a CMUT array by simply adding a polarization voltage and using components normally employed in a commercial echographic system, like Technos (ESAOTE S.p.A.). Using low temperature, surface micromachined technology, the researchers produced a 64-element CMUT array transducer that can operate as both a linear array at 3.5 MHz and a phased array at 7 MHz due to the inherently large bandwidth. The SiNi circular membranes are about 50 μm in diameter and the electrode gap is nominally 0.4 μm. Both of the electrodes (and their interconnections that link each transducer cell in parallel with its neighbor cells) and the fixed bottom metalization are patterned by optical lithography and wet etching. Parasitic capacitance was reduced by patterning the top interconnections such that the overlap with the bottom electrode interconnections was avoided.

Noble et al. (2002) fabricated a CMUT array in a low temperature, PECVD silicon nitride process and showed successful control and uniformity in the design parameters, like intrinsic membrane stress, resulting in a less-than-5% variation in the capacitances of deflected CMUT membranes. Amplifiers with gains between two (2) and ten (10) were then successfully employed for "post-processing" CMUTs directly onto analog electronics. Resistive and capacitive feedback circuits were integrated with typical 1 mm CMUTs and evaluated. Full PSpice (Cadence Design Systems, Inc.) simulations were also generated and used to ensure the lowest noise in the amplifier while attempting to maximize feedback components and gain, amplifier bandwidth up to 10 MHz, and stability against power supply variations. No-

ble et al. achieved a fully integrated device with a normal 1.3 MHz center frequency and 100% bandwidth and a good 70:1 signal-to-noise ratio.

Mills and Smith (2003) applied CMUT technology to medical ultrasound imaging. They created real-time *in-vivo* images of a carotid artery using an immersed CMUT linear array and compared them to images from a PZT array. The CMUT array had a -6 dB bandwidth of 110%, which is greater than the typical bandwidths of 70-80% for piezoelectric ceramic-based probes. Mills and Smith also found out that the CMUT array had a slightly better axial resolution than the PZT array, but the PZT array had a greater sensitivity. The results support their hypothesis that CMUTs are showing real potential in terms of improved axial resolution and extremely broad bandwidth operation.

1.2.2 FEM Simulations

Eccardt et al. (1996) built arrays of hexagonally-shaped transducers with 0.4 μm-thick polysilicon membranes of 40 μm-sidelength and an effective gap of 0.45 μm. One phased array consisted of 30 $\times$ 30 membranes that were all electrically excited, while another test structure array of 38 membranes was not phased with most membranes being excited only through fluid coupling with the few excited membranes. The transducers were driven by an AC voltage of 1 V with a DC offset of 21 V in either water or low-viscosity oil. FEM simulations from ANSYS agreed with the experimental results except for an experimental peak due to standing waves between the surface and the liquid level of 7 mm. Their arrays in water had resonance frequencies around 10 MHz and bandwidths of about 10 MHz.

Bozkurt et al. (1998) used FEM simulations and normal mode theory to investigate the radiation of energy from a 1.0 μm-thick circular silicon nitride membrane to the surrounding silicon wafer, which is claimed to be the main loss mechanism of a CMUT. They used a lossy medium (Cerjan et al., 1985) of considerable length outside of the membrane to absorb the radiation energy. This energy is coupled to the propagating modes of the silicon wafer at the membrane-substrate junction, and for the frequency range of interest (1-3.5 MHz), the only propagating modes are the two lowest-order antisymmetric and symmetric Lamb wave modes. Bozkurt et al. found out that the dominant mode is the antisymmetric mode, which carries 90% of the total radiated power. The symmetric Lamb wave becomes more important,

but still not dominant, at higher frequencies.

The electrostatic force should be applied only where it is most effective, such as at the center of a circular membrane. Electrode patterning has been used for selective mode excitation of resonators (Prak et al., 1992) and in the optimization of capacitive pressure transducers and microphones (Voorthuyzen et al., 1991). Bozkurt et al. (1999) used electrode patterning in FEM simulations with ANSYS to optimize the performance of a circular membrane with a centered circular electrode. They found out that the bandwidth of the optimally metalized transducer is twice that of the fully metalized device, with the electrode radius ranging between 40 and 50% of the membrane radius.

Bayram et al. (2001) performed FEM simulations with ANSYS to determine how sizes and locations of embedded, centered electrodes affect the collapse voltage of a circular SiNi membrane for possible applications in CMUTs. They determined that the collapse voltage increases in proportion to the metal thickness for constant membrane thickness. For thin electrodes, the collapse voltage decreases monotonically as the plate moves closer to the membrane bottom, but for thicker electrodes, the collapse voltage decrease is not monotonic because an intermediate maximum value exists. The collapse voltage also increases asymptotically as the outer electrode radius decreases, but decreases initially for electrodes of finite thickness. In fact, most of the increase is after the outer electrode radius has decreased by more than half. Specifically, Bayram et al. found out that, if the outer radius of the electrode is half of the radius of the membrane, the collapse voltage is only 15% larger than that for the fully-metalized membrane.

Bayram et al. (2003) applied voltages between the collapse and snapback voltages. In this operation regime, the center of the membrane was always in contact with the substrate. Their FEM simulations showed that a CMUT operating in the new regime between collapse and snapback voltages possesses a coupling coefficient (k_T^2) higher than a CMUT operating in the conventional regime below its collapse voltage. For their collapsed circular membrane, Bayram et al. found out that the average k_T^2 value for a large AC signal (100 ± 30V) is 0.3 in the conventional regime and 0.6 in the new regime. This increase of 100% is advantageous for the CMUT as both a receiver and a trasmitter, because there could be increases in sensitivity, peak output pressure, and total acoustic energy through operation in the new regime.

1.2.3 Analytical Plate or Membrane Models

Ladabaum et al. (1996) created an equivalent circuit model of the MUT in order to facilitate design. As first suggested by Mason (1948), the mechanical impedance of a membrane with no damping is found and then inserted into a transformer equivalent circuit. Ladabaum et al. used the same type of equation for membrane motion as Mason that includes plate and membrane terms, being based on the assumption that the tension generated by membrane displacement is small compared to the tension. They solved the equation of motion for a clamped circular membrane undergoing harmonic motion using Bessel functions and then determined the mechanical impedance, which is the ratio of pressure to the average membrane speed. After approximating the MUT as a parallel plate capacitor, Ladabaum et al. finally created the electrical equivalent circuit of the MUT. They demonstrated that immersion MUTs can transmit ultrasound in water from 1 to 20 MHz and can send and receive airborne ultrasound at 6 MHz.

Ahrens et al. (2002) fabricated CMUTs that have conductive polysilicon membranes above a structured sacrificial layer. They used an electrical circuit equivalent for model simulation. Nearly all of the publications dealing with equivalent circuits for this kind of CMUT rely on the equation of motion introduced by Mason (1948), which relies on assumptions such as small deflections at the operating point. Ahrens et al. solved Mason's model in terms of Bessel functions for the shape function of a circular membrane that undergoes harmonic excitation. The shape function was used to find the membrane impedance, being necessary for the equivalent circuit. In order to use the model for non-circular membranes, they equated areas and boundary conditions for the square and hexagonal membranes with the circular membranes. Then, they performed experiments to obtain the transducer impedances for square, hexagonal, and circular membranes as a function of frequency. The DC voltages ranged from 15 to 18 V, the AC voltage was 1 V, and the frequencies ranged from 1 to 4.5 MHz. Ahrens et al. found good agreement in terms of the resonance frequencies with experimental values for the circular and hexagonal membranes, concluding that the equivalent circuit is a powerful tool in analyzing the impact of basic design and process parameters.

1.2.4 Lumped-Element Models

Eccardt et al. (1997) treated the membrane as a plate with a spring and derived an analytical expression for the electromechanical coupling factor, showing that low parasitic capacitances lead to higher coupling factors. In fact, coupling factors like those of piezoelectric transducers ($k \approx 0.7$) are achievable only at static deflections near pull-in. They also showed that the noise factor depends significantly on the phase angle of the transducer impedance, which is mainly dominated by the coupling factor and the mechanical quality factor Q. A high coupling factor increases transmitter sensitivity and decreases transmitter electrical energy loss and receiver noise. Eccardt et al. generated pulses using previously fabricated arrays (Eccardt et al., 1996) and found out that, with a DC voltage of 16 V and an AC voltage of 9 V, the large 30 $\times$ 30 array produces a sound pressure of 500 Pa at a distance of 20 mm. Thus, micromachined capacitive transducers can produce almost the same sound pressure as piezoelectric transducers of similar size. They also found out that an extra 0.8 μm-thick aluminum electrode on a 0.4 μm-thick polysilicon membrane more than doubles the resonance frequencies through membrane stiffening (Eccardt et al., 1997).

Ladabaum et al. (1998) fabricated MUTs with 0.6 μm-thick SiNi hexagonal membranes for both air and water transmission. The air-coupled transducer was excited with a bias voltage of 30 V and an AC voltage of 16 V at 2.3 MHz. The receiver was 1 cm from the transmitter and a 1.9 mm aluminum slab was between the two transducers. A transducer dynamic range of 110 dB was observed. A vacuum-sealed pair of transducers was also operated 0.5 cm apart in water with frequencies from 1 to 20 MHz, with a measured 60 dB signal-to-noise ratio at 3 MHz. Ladabaum et al. also developed an equivalent circuit model for circular membranes by assuming small signals and ignoring electrical fringing fields. The membrane tension was also assumed to be uniform and independent of displacement and dissipation was ignored. Ladabaum et al. then solved for the mechanical impedance of the circular membrane, which is necessary for the equivalent circuit model. They fit the theory to the experiment by adding a loss term to the circuit model, allowing the experiment to validate the theory. The aluminum transmission experiments showed that MUTs are feasible for such practical air-coupled applications as nondestructive testing, and the water transmission experiments

showed that MUTs have the potential to approach the performance of piezoelectrics in liquids.

1.2.5 Other Models

Perçin and Khuri-Yakub (2001) fabricated a novel ultrasonic transducer composed of 2-D arrays of 100 μm-diameter, 0.3 μm-thick clamped silicon-nitride circular microplates that are actuated by 0.3 μm-thick annular coatings of piezoelectric zinc oxide. The devices have operating resonance frequencies ranging from 0.45 to 4.5 MHz. The ring shape of the piezoelectric necessitated the use of either the finite element method or complex analytical models for analysis. Perçin and Khuri-Yakub initially used finite element analysis to optimize the transducer design, but later used classical thin plate theory and Mindlin plate theory to derive two-dimensional plate equations for a step-wise laminated circular plate (Perçin and Khuri-Yakub, 2002). Ultrasonic transmission was demonstrated in air and water. They discovered that the third mode has a relatively small coupling to the surrounding medium but still a relatively large displacement, and thus this mode is more suitable for fluid ejection applications (Perçin and Khuri-Yakub, 2001).

Lohfink et al. (2003) derived a 1D nonlinear model for CMUT arrays from FEM simulations using piston radiator and plate capacitance theory. Their model is 1D in the sense that membrane displacement of a CMUT cell is the product of the membrane center displacement (as a function of time) and a constant shape function (as a function of radius). For an array of parallel driven cells, the acoustical parameters were derived as a complex mechanical fluid impedance depending on the membrane shape form. The real and imaginary parts correspond to damping and an additional mass, respectively. These terms along with parameters resulting from FEM simulations were included in their 1D model, which is two coupled differential equations (a force balance and a current balance equation). Lohfink et al. solved them with MATLAB and Simulink and found out that, for the transmit case, the sound pressures obtained with the nonlinear model could be three times those obtained with the comparable linear model.

1.3 Dissertation Objectives

Analysis through reduced-order modeling is atypical for electrostatically actuated circular plates. As previously stated, many researchers use FEM simulations, analytical membrane models, or lumped-element models to analyze resonating circular microstructures. These approaches have their respective flaws. Most FEM simulations are computationally inefficient or breakdown near pull-in of electrostatically actuated structures, and membrane models ignore plate bending, which is needed for bending-dominated microstructures.

Because of the numerous applications of CMUTs, we will investigate the dynamics of electrostatically actuated circular plates with an analytical reduced-order model (macromodel). Consequently, one objective is to model CMUTs with a reduced-order model that

- accounts for residual stresses,
- allows for general material and geometric design variables,
- allows for large deformations by including the first geometric nonlinearity of the von Kármán type,
- allows for general boundary conditions that affect the CMUT static and dynamic responses,
- accounts for stress-dependent boundary conditions,
- is robust up to the pull-in instability, and
- is general enough to be an effective design tool.

Consequently, the proposed reduced-order model captures the complex multi-energy-domain physics in a relatively simple and compact model. After the macromodel is developed, the method of multiple scales is used to derive a semi-analytical expression for the steady-state amplitude of vibration for primary resonance excitation of the first axisymmetric mode. Therefore, we wish to use the macromodel to

- calculate the CMUTs resonance frequencies at equilibrium,

- approximate the responses of CMUTs excited by primary resonance excitations,
- investigate the transitions, if any, in system behavior as the DC voltage increases towards pull-in, and
- calculate the amplitudes of vibrations up to the pull-in instability.

1.4 Dissertation Outline

The organization of the Dissertation is as follows:

In Chapter 2, we present a new approach to the modeling and simulation of CMUTs under the effects of in-plane residual loading, the inherent electrostatic forces, and pressure differences. The nonlinear governing equations are derived for a circular plate with an infinitesimally thin electrode; thus include the first geometric nonlinearity of the von Kármán type.

In Chapter 3, we nondimensionalize the governing equations, establish the boundary conditions for a clamped-clamped plate, and discretize the system by using a Galerkin approach. The distributed-parameter equations are then reduced to a finite system of ordinary-differential equations in time. We solve these equations for the equilibrium states due to a general electric potential and determine the natural frequencies of the axisymmetric modes for the stable deflected positions. As expected, the fundamental natural frequency generally decreases as the bias voltage increases, reaching a value of zero at pull-in. However, strain-hardening effects can cause the frequencies to increase with voltage. The macromodel is validated by using data from experiments and simulations performed on silicon-based microelectromechanical systems (MEMS). For example, the pull-in voltages differ by about 1% from values produced by full 3-D MEMS simulations.

In Chapter 4, the macromodel is used to investigate the response of an electrostatically actuated clamped circular plate to a primary resonance excitation of its first axisymmetric mode. The method of multiple scales is used to derive a semi-analytical expression for the equilibrium amplitude of vibration. Furthermore, expressions for the possible inflection point and saddle-node bifurcations on the frequency-response curve are derived.

In Chapter 5, the frequency-response equation from Chapter 4 is used to investigate the nonlinear behavior of the CMUT plate. The plate is found to always transition from

a hardening-type to a softening-type behavior as the DC voltage increases towards pull-in. Also, at least three modes are found necessary in the reduced-order model to characterize the responses of air-immersed CMUTs to primary resonance excitations. Furthermore, design curves are generated to approximate the effective nonlinearity and hence determine the transition from hardening- to softening-type for any system parameters for the common case of zero pressure difference across the CMUT plate.

In Chapter 6, non-clamped boundary conditions are incorporated into the macromodel for it to be a more effective design tool for CMUTs. We assume that the boundary force and moment affect the slope of the plate at the boundary in a linear manner. The electrode is still considered to be infinitesimally thin, but the electrode is allowed to have general inner and outer radii. The Galerkin approach is then utilized with an additional static solution. The updated reduced-order model is then used to show the sensitivity of the pull-in voltage to the boundary conditions. Boundary parameters are extracted by matching the pull-in voltages of the macromodel to those obtained from FEM simulations for CMUTs with varying outer and inner radii. The static behavior of the updated macromodel is validated in that the pull-in voltages for the macromodel and FEM simulations are very close to each other and the extracted boundary parameters are physically realistic.

In Chapter 7, a macromodel for CMUTs is created that includes boundary effects and finite-thickness electrodes. Matching conditions ensure the continuity of displacements, slopes, forces, and moments from the composite to the non-composite regime of the CMUT. We attempt to validate this model with results from FEM simulations. In general, the center deflections obtained with the macromodel fall below those obtained from the FEM simulation, especially for relatively high residual stresses, but the predicted first natural frequencies that accompany the deflections are very close to those obtained with the FEM simulations. Furthermore, the forced vibration characteristics predicted with the macromodel compare well with those obtained experimentally in which the primary resonance curve bends to the right because the effective nonlinearity of the particular CMUT is of the hardening-type.

Finally, we present a summary of the work in Chapter 8 along with conclusions and recommendations for future work.

Chapter 2

General von Kármán Formulation of Circular Plates under Electrostatic and Residual Stress Loadings

2.1 Basic Assumptions

The derivation in this chapter is for a homogeneous and isotropic von Kármán plate. We first list the assumptions underlying the Kirchhoff classical plate theory (CPT) and the von Kármán plate theory. The Kirchhoff plate theory assumptions are (Ventsel and Krauthammer, 2001):

- The deflection of the midplane is small compared with the thickness of the plate. The slope of the deflected surface is therefore very small and the square of the slope is negligible in comparison to unity.
- The midplane remains unstrained subsequent to bending.
- A straight line (filament) initially normal to the midplane remains straight and normal to that surface during the deformation.

- The stress σ_z normal to the midplane is small compared with the other stress components and may be neglected in the stress-strain relations.

For the von Kármán plate theory, the deflection is on the order of the plate thickness, though it is still smaller than the other plate dimensions. Consequently, the first and second assumptions in the CPT do not hold anymore, but the other assumptions still hold.

2.2 Problem Formulation

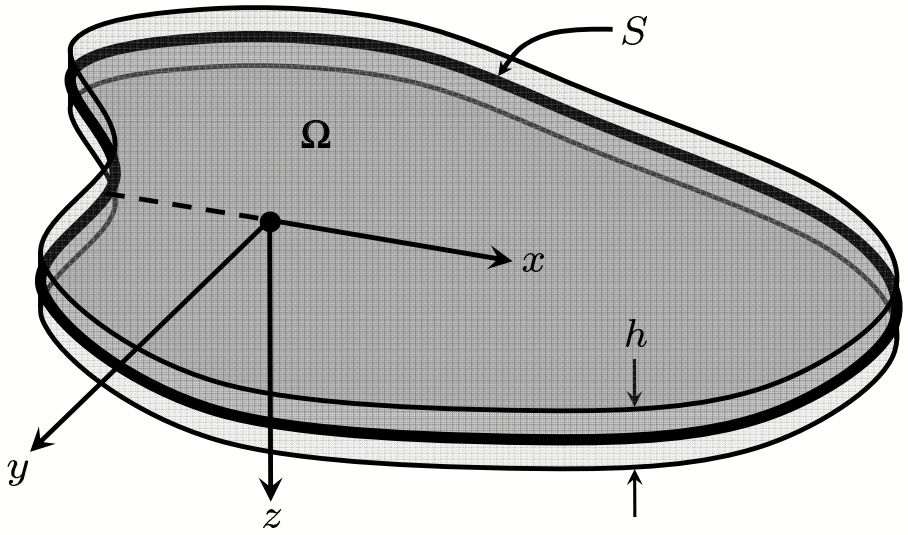

Figure 2.1: An undeformed plate with a Cartesian coordinate frame.

We derive the governing equations that depend on cylindrical coordinates by first deriving the equations using Cartesian coordinates and then making variable transformations between the two coordinate sets. The flat plate seen in Figure 2.1 has a density ρ and a thickness h and the following displacement field (Ventsel and Krauthammer, 2001):

$$u_x(x,y,z,t) = u_0(x,y,t) - z\frac{\partial w}{\partial x} \tag{2.1a}$$

$$u_y(x,y,z,t) = v_0(x,y,t) - z\frac{\partial w}{\partial y} \tag{2.1b}$$

$$u_z(x,y,z,t) = w(x,y,t) \tag{2.1c}$$

where u_0, v_0, and w are the displacements of the midplane at time t in the $x-$, $y-$, and $z-$

directions, respectively, and u_x, u_y, and u_z constitute the displacement field of the medium. The three general nonlinear strains according to von Kármán are

$$\epsilon_{xx} = \frac{\partial u_x}{\partial x} + \frac{1}{2}\left(\frac{\partial u_z}{\partial x}\right)^2 \tag{2.2a}$$

$$\epsilon_{yy} = \frac{\partial u_y}{\partial y} + \frac{1}{2}\left(\frac{\partial u_z}{\partial y}\right)^2 \tag{2.2b}$$

$$\epsilon_{xy} = \frac{1}{2}\left(\frac{\partial u_x}{\partial y} + \frac{\partial u_y}{\partial x}\right) + \frac{1}{2}\frac{\partial u_z}{\partial x}\frac{\partial u_z}{\partial y} \tag{2.2c}$$

which reduce to

$$\epsilon_{xx} = \frac{\partial u_0}{\partial x} - z\frac{\partial^2 w}{\partial x^2} + \frac{1}{2}\left(\frac{\partial w}{\partial x}\right)^2 \tag{2.3a}$$

$$\epsilon_{yy} = \frac{\partial v_0}{\partial y} - z\frac{\partial^2 w}{\partial y^2} + \frac{1}{2}\left(\frac{\partial w}{\partial y}\right)^2 \tag{2.3b}$$

$$\epsilon_{xy} = \frac{1}{2}\left(\frac{\partial u_0}{\partial y} + \frac{\partial v_0}{\partial x}\right) - z\frac{\partial^2 w}{\partial x \partial y} + \frac{1}{2}\frac{\partial w}{\partial x}\frac{\partial w}{\partial y} \tag{2.3c}$$

after substitution of the displacement field equations, Equations (2.1). We note that ϵ_{xz}, ϵ_{yz}, and ϵ_{zz} are identically zero because of the thin-plate theory displacements in Equations (2.1).

The principle of virtual displacements can be expressed as

$$\delta W = 0 \tag{2.4}$$

where δW is the total virtual work done by external and internal forces for any admissible virtual displacements (Ventsel and Krauthammer, 2001): the strain energy, kinetic energy, and work done by the external loads. In Cartesian coordinates, this principle becomes

$$\begin{aligned}\delta W = &\int_0^T \int_\Omega \int_{-\frac{h}{2}}^{\frac{h}{2}} \left(\sigma_{xx}\delta\epsilon_{xx} + \sigma_{yy}\delta\epsilon_{yy} + 2\,\sigma_{xy}\delta\epsilon_{xy}\right) dz dx dy dt \\ &- \int_0^T \int_\Omega \int_{-\frac{h}{2}}^{\frac{h}{2}} \rho\left(\dot{u}_x\delta\dot{u}_x + \dot{u}_y\delta\dot{u}_y + \dot{u}_z\delta\dot{u}_z\right) dz dx dy dt \\ &- \int_0^T \int_\Omega \int_{-\frac{h}{2}}^{\frac{h}{2}} \left(q_x\delta u_x + q_y\delta u_y + q_z\delta u_z\right) dz dx dy dt \;=\; 0\end{aligned} \tag{2.5}$$

for the thin plate, where q_x, q_y, and q_z are the external volumetric forces and surface tractions, T is the final time, Ω denotes the undeformed plate domain, and the overdot represents differentiation with respect to time.

We define

$$N_{xx} = \int_{-\frac{h}{2}}^{\frac{h}{2}} \sigma_{xx}\, dz \tag{2.6a}$$

$$N_{yy} = \int_{-\frac{h}{2}}^{\frac{h}{2}} \sigma_{yy}\, dz \tag{2.6b}$$

$$N_{xy} = \int_{-\frac{h}{2}}^{\frac{h}{2}} \sigma_{xy}\, dz \tag{2.6c}$$

$$M_{xx} = \int_{-\frac{h}{2}}^{\frac{h}{2}} \sigma_{xx}\, z\, dz \tag{2.6d}$$

$$M_{yy} = \int_{-\frac{h}{2}}^{\frac{h}{2}} \sigma_{yy}\, z\, dz \tag{2.6e}$$

$$M_{xy} = \int_{-\frac{h}{2}}^{\frac{h}{2}} \sigma_{xy}\, z\, dz \tag{2.6f}$$

where N_{xx}, N_{yy}, and N_{xy} are the in-plane forces and M_{xx}, M_{yy}, and M_{xy} are the out-of-plane moments. Upon substitution of Equations (2.3) and (2.6) into Equation (2.5), the principle of virtual displacements becomes

$$\begin{aligned}
\int_0^T \int_\Omega \Bigg[& N_{xx}\left(\frac{\partial \delta u_0}{\partial x} + \frac{\partial w}{\partial x}\frac{\partial \delta w}{\partial x}\right) - M_{xx}\frac{\partial^2 \delta w}{\partial x^2} \\
& + N_{yy}\left(\frac{\partial \delta v_0}{\partial y} + \frac{\partial w}{\partial y}\frac{\partial \delta w}{\partial y}\right) - M_{yy}\frac{\partial^2 \delta w}{\partial y^2} \\
& + N_{xy}\left(\frac{\partial \delta u_0}{\partial y} + \frac{\partial \delta v_0}{\partial x} + \frac{\partial \delta w}{\partial x}\frac{\partial w}{\partial y} + \frac{\partial w}{\partial x}\frac{\partial \delta w}{\partial y}\right) - 2\, M_{xy}\frac{\partial^2 \delta w}{\partial x \partial y} \\
& - I_0\left(\dot{u}_0 \delta \dot{u}_0 + \dot{v}_0 \delta \dot{v}_0 + \dot{w}\delta \dot{w}\right) - I_2\left(\frac{\partial \dot{w}}{\partial x}\frac{\partial \delta \dot{w}}{\partial x} + \frac{\partial \dot{w}}{\partial y}\frac{\partial \delta \dot{w}}{\partial y}\right) \\
& - \left(Q_x \delta u_0 - M_x \frac{\partial \delta w}{\partial x} + Q_y \delta v_0 - M_y \frac{\partial \delta w}{\partial y} + Q_z \delta w\right)\Bigg] dx dy dt = 0
\end{aligned} \tag{2.7}$$

where $I_0 = \rho h$ is the mass per area, $I_2 = \frac{1}{12}\rho h^3$ is the rotary inertia, and

$$Q_x = \int_{-\frac{h}{2}}^{\frac{h}{2}} q_x \, dz \tag{2.8a}$$

$$Q_y = \int_{-\frac{h}{2}}^{\frac{h}{2}} q_y \, dz \tag{2.8b}$$

$$Q_z = \int_{-\frac{h}{2}}^{\frac{h}{2}} q_z \, dz \tag{2.8c}$$

$$M_x = \int_{-\frac{h}{2}}^{\frac{h}{2}} q_x \, z \, dz \tag{2.8d}$$

$$M_y = \int_{-\frac{h}{2}}^{\frac{h}{2}} q_y \, z \, dz \tag{2.8e}$$

To account explicitly for surface tractions along the bounding curve(s) of the medium, we let

$$Q_x \to Q_x + Q_x^S \delta^S(\boldsymbol{x}) \tag{2.9a}$$

$$Q_y \to Q_y + Q_y^S \delta^S(\boldsymbol{x}) \tag{2.9b}$$

$$Q_z \to Q_z + Q_z^S \delta^S(\boldsymbol{x}) \tag{2.9c}$$

$$M_x \to M_x + M_x^S \delta^S(\boldsymbol{x}) \tag{2.9d}$$

$$M_y \to M_y + M_y^S \delta^S(\boldsymbol{x}) \tag{2.9e}$$

where the Dirac delta function $\delta^S(\boldsymbol{x})$ has dimensions of inverse length and magnitudes given by

$$\delta^S(\boldsymbol{x}) = \begin{cases} 0, & \boldsymbol{x} \notin S \\ \infty, & \boldsymbol{x} \in S \end{cases} \quad \text{where} \quad \int_\Omega f(\boldsymbol{x}) \, \delta^S(\boldsymbol{x}) \, dxdy = \int_S f(\boldsymbol{x}) \, dS \tag{2.10}$$

for a sufficiently smooth scalar function $f(\boldsymbol{x})$, and S is the curve(s) bounding the plate in the x-y plane. We note that the surface tractions along the upper and lower surfaces of the plate are implicitly accounted for in Q_x, Q_y, and Q_z. Equation (2.7) then becomes, with

some rearranging,

$$\begin{aligned}
\int_0^T \int_\Omega \Big[& (N_{xx}, N_{xy}) \cdot \nabla \delta u_0 + (N_{xy}, N_{yy}) \cdot \nabla \delta v_0 \\
& + (N_{xx}\frac{\partial w}{\partial x}, N_{xy}\frac{\partial w}{\partial x}) \cdot \nabla \delta w + (N_{xy}\frac{\partial w}{\partial y}, N_{yy}\frac{\partial w}{\partial y}) \cdot \nabla \delta w \\
& - (M_{xx}, M_{xy}) \cdot \nabla \frac{\partial \delta w}{\partial x} - (M_{xy}, M_{yy}) \cdot \nabla \frac{\partial \delta w}{\partial y} \\
& - I_0 \left(\dot{u}_0 \delta \dot{u}_0 + \dot{v}_0 \delta \dot{v}_0 + \dot{w} \delta \dot{w} \right) - I_2 \left(\frac{\partial \dot{w}}{\partial x}, \frac{\partial \dot{w}}{\partial y} \right) \cdot \nabla \delta \dot{w} \\
& - \left(Q_x \delta u_0 + Q_y \delta v_0 + Q_z \delta w \right) + (M_x, M_y) \cdot \nabla \delta w \Big] dx dy dt \\
+ \int_0^T \int_S \Big[& - \left(Q_x^S \delta u_0 + Q_y^S \delta v_0 + Q_z^S \delta w \right) + \left(M_x^S, M_y^S \right) \cdot \nabla \delta w \Big] dS dt = 0
\end{aligned} \tag{2.11}$$

where ∇ is the spatial gradient. In order to transfer derivatives away from δu, δv, and δw, we use Green's theorem expressed as

$$\int_\Omega \mathbf{f} \cdot \nabla g \, d\Omega = \int_S g \, \mathbf{f} \cdot \mathbf{n} \, dS - \int_\Omega g \, \nabla \cdot \mathbf{f} \, d\Omega \tag{2.12}$$

where $\mathbf{f}(\boldsymbol{x})$ and $g(\boldsymbol{x})$ are vector and scalar functions, respectively, and $\mathbf{n}$ is the outward normal vector to S. We apply Green's theorem to each vector product in Equation (2.11) or

integrate by parts to obtain

$$\int_\Omega (N_{xx}, N_{xy}) \cdot \nabla \delta u_0 \, d\Omega = \int_S \delta u_0 \, (N_{xx}, N_{xy}) \cdot \mathbf{n} \, dS - \int_\Omega \delta u_0 \left(\frac{\partial N_{xx}}{\partial x} + \frac{\partial N_{xy}}{\partial y} \right) d\Omega \tag{2.13a}$$

$$\int_\Omega (N_{xy}, N_{yy}) \cdot \nabla \delta v_0 \, d\Omega = \int_S \delta v_0 \, (N_{xy}, N_{yy}) \cdot \mathbf{n} \, dS - \int_\Omega \delta v_0 \left(\frac{\partial N_{xy}}{\partial x} + \frac{\partial N_{yy}}{\partial y} \right) d\Omega \tag{2.13b}$$

$$\int_\Omega \left(N_{xx} \frac{\partial w}{\partial x}, N_{xy} \frac{\partial w}{\partial x} \right) \cdot \nabla \delta w \, d\Omega = \int_S \delta w \left(N_{xx} \frac{\partial w}{\partial x}, N_{xy} \frac{\partial w}{\partial x} \right) \cdot \mathbf{n} \, dS - \int_\Omega \delta w \left[\frac{\partial}{\partial x} \left(N_{xx} \frac{\partial w}{\partial x} \right) + \frac{\partial}{\partial y} \left(N_{xy} \frac{\partial w}{\partial x} \right) \right] d\Omega \tag{2.13c}$$

$$\int_\Omega \left(N_{xy} \frac{\partial w}{\partial y}, N_{yy} \frac{\partial w}{\partial y} \right) \cdot \nabla \delta w \, d\Omega = \int_S \delta w \left(N_{xy} \frac{\partial w}{\partial y}, N_{yy} \frac{\partial w}{\partial y} \right) \cdot \mathbf{n} \, dS - \int_\Omega \delta w \left[\frac{\partial}{\partial x} \left(N_{xy} \frac{\partial w}{\partial y} \right) + \frac{\partial}{\partial y} \left(N_{yy} \frac{\partial w}{\partial y} \right) \right] d\Omega \tag{2.13d}$$

$$\int_\Omega (M_{xx}, M_{xy}) \cdot \nabla \frac{\partial \delta w}{\partial x} \, d\Omega = \int_S \frac{\partial \delta w}{\partial x} \, (M_{xx}, M_{xy}) \cdot \mathbf{n} \, dS - \int_\Omega \frac{\partial \delta w}{\partial x} \left(\frac{\partial M_{xx}}{\partial x} + \frac{\partial M_{xy}}{\partial y} \right) d\Omega \tag{2.13e}$$

$$\int_\Omega (M_{xy}, M_{yy}) \cdot \nabla \frac{\partial \delta w}{\partial y} \, d\Omega = \int_S \frac{\partial \delta w}{\partial y} \, (M_{xy}, M_{yy}) \cdot \mathbf{n} \, dS - \int_\Omega \frac{\partial \delta w}{\partial y} \left(\frac{\partial M_{xy}}{\partial x} + \frac{\partial M_{yy}}{\partial y} \right) d\Omega \tag{2.13f}$$

$$\int_0^T (\dot{u}_0 \delta \dot{u}_0 + \dot{v}_0 \delta \dot{v}_0 + \dot{w} \delta \dot{w}) \, dt = [\dot{u}_0 \delta u_0 + \dot{v}_0 \delta v_0 + \dot{w} \delta w]_0^T - \int_0^T (\ddot{u}_0 \delta u_0 + \ddot{v}_0 \delta v_0 + \ddot{w} \delta w) \, dt \tag{2.13g}$$

$$\int_\Omega \left(\frac{\partial \dot{w}}{\partial x}, \frac{\partial \dot{w}}{\partial y} \right) \cdot \nabla \delta \dot{w} \, d\Omega = \int_S \delta \dot{w} \left(\frac{\partial \dot{w}}{\partial x}, \frac{\partial \dot{w}}{\partial y} \right) \cdot \mathbf{n} \, dS - \int_\Omega \delta \dot{w} \left(\frac{\partial^2 \dot{w}}{\partial x^2} + \frac{\partial^2 \dot{w}}{\partial y^2} \right) d\Omega \tag{2.13h}$$

$$\int_\Omega (M_x, M_y) \cdot \nabla \delta w \, d\Omega = \int_S \delta w \, (M_x, M_y) \cdot \mathbf{n} \, dS - \int_\Omega \delta w \left(\frac{\partial M_x}{\partial x} + \frac{\partial M_y}{\partial y} \right) d\Omega \tag{2.13i}$$

Before substitution of Equations (2.13) into Equation (2.11), we combine Equations (2.13e)

and (2.13f) with some rearranging to obtain

$$\begin{aligned}\int_\Omega \left[(M_{xx}, M_{xy}) \cdot \nabla \frac{\partial \delta w}{\partial x} + (M_{xy}, M_{yy}) \cdot \nabla \frac{\partial \delta w}{\partial y} \right] d\Omega \\ = \int_S \left[\frac{\partial \delta w}{\partial x} (M_{xx}, M_{xy}) + \frac{\partial \delta w}{\partial y} (M_{xy}, M_{yy}) \right] \cdot \mathbf{n} \, dS \\ - \int_\Omega \left(\frac{\partial M_{xx}}{\partial x} + \frac{\partial M_{xy}}{\partial y}, \frac{\partial M_{xy}}{\partial x} + \frac{\partial M_{yy}}{\partial y} \right) \cdot \nabla \delta w \, d\Omega \end{aligned} \tag{2.14}$$

Then, we use Green's theorem for the last integral in Equation (2.14) and obtain

$$\begin{aligned}\int_\Omega \left[(M_{xx}, M_{xy}) \cdot \nabla \frac{\partial \delta w}{\partial x} + (M_{xy}, M_{yy}) \cdot \nabla \frac{\partial \delta w}{\partial y} \right] d\Omega \\ = \int_S \left[\frac{\partial \delta w}{\partial x} (M_{xx}, M_{xy}) + \frac{\partial \delta w}{\partial y} (M_{xy}, M_{yy}) \right] \cdot \mathbf{n} \, dS \\ - \int_S \delta w \left(\frac{\partial M_{xx}}{\partial x} + \frac{\partial M_{xy}}{\partial y}, \frac{\partial M_{xy}}{\partial x} + \frac{\partial M_{yy}}{\partial y} \right) \cdot \mathbf{n} \, dS \\ + \int_\Omega \delta w \left(\frac{\partial^2 M_{xx}}{\partial x^2} + 2 \frac{\partial^2 M_{xy}}{\partial x \partial y} + \frac{\partial^2 M_{yy}}{\partial y^2} \right) d\Omega \end{aligned} \tag{2.15}$$

We also integrate Equation (2.13h) with respect to time and, after integration of the resulting right-hand side by parts, obtain

$$\begin{aligned}\int_0^T \int_\Omega \left(\frac{\partial \dot{w}}{\partial x}, \frac{\partial \dot{w}}{\partial y} \right) \cdot \nabla \delta \dot{w} \, d\Omega dt = \left[\int_S \delta w \left(\frac{\partial \dot{w}}{\partial x}, \frac{\partial \dot{w}}{\partial y} \right) \cdot \mathbf{n} \, dS \right]_0^T \\ - \int_0^T \int_S \delta w \left(\frac{\partial \ddot{w}}{\partial x}, \frac{\partial \ddot{w}}{\partial y} \right) \cdot \mathbf{n} \, dS dt - \left[\int_\Omega \delta w \left(\frac{\partial^2 \dot{w}}{\partial x^2} + \frac{\partial^2 \dot{w}}{\partial y^2} \right) d\Omega \right]_0^T \\ + \int_0^T \int_\Omega \delta w \left(\frac{\partial^2 \ddot{w}}{\partial x^2} + \frac{\partial^2 \ddot{w}}{\partial y^2} \right) d\Omega dt \end{aligned} \tag{2.16}$$

2.3 General Governing Equations

We substitute Equations (2.13), (2.15), and (2.16) into Equation (2.11), assume no initial or final plate motion, and consequently set the resulting terms evaluated from $t = 0$ to $t = T$ equal to zero. We also set the coefficients of δu, δv, and δw in the resulting area integrands

equal to zero for admissible variations and obtain

$$\delta u: \quad \frac{\partial N_{xx}}{\partial x}+\frac{\partial N_{xy}}{\partial y}-I_0\ddot{u}_0+Q_x=0 \quad \text{in } \Omega \tag{2.17a}$$

$$\delta v: \quad \frac{\partial N_{xy}}{\partial x}+\frac{\partial N_{yy}}{\partial y}-I_0\ddot{v}_0+Q_y=0 \quad \text{in } \Omega \tag{2.17b}$$

$$\begin{aligned}\delta w: \quad & \frac{\partial}{\partial x}\left(N_{xx}\frac{\partial w}{\partial x}\right)+\frac{\partial}{\partial y}\left(N_{xy}\frac{\partial w}{\partial x}\right)+\frac{\partial}{\partial x}\left(N_{xy}\frac{\partial w}{\partial y}\right)+\frac{\partial}{\partial y}\left(N_{yy}\frac{\partial w}{\partial y}\right)\\ & +\frac{\partial^2 M_{xx}}{\partial x^2}+2\frac{\partial^2 M_{xy}}{\partial x\partial y}+\frac{\partial^2 M_{yy}}{\partial y^2}-I_0\ddot{w}+I_2\frac{\partial^2}{\partial t^2}\left(\frac{\partial^2 w}{\partial x^2}+\frac{\partial^2 w}{\partial y^2}\right)\\ & +Q_z+\left(\frac{\partial M_x}{\partial x}+\frac{\partial M_y}{\partial y}\right)=0 \quad \text{in } \Omega\end{aligned} \tag{2.17c}$$

Either the coefficients of δu, δv, δw, $\delta\frac{\partial w}{\partial x}$, and $\delta\frac{\partial w}{\partial y}$ in the resulting boundary integrands are zero for admissible variations or the variations themselves are zero; that is,

$$(N_{xx},N_{xy})\cdot\mathbf{n}=Q_x^S \quad \text{or} \quad \delta u_0=0 \quad \text{on } S \tag{2.18a}$$

$$(N_{xy},N_{yy})\cdot\mathbf{n}=Q_y^S \quad \text{or} \quad \delta v_0=0 \quad \text{on } S \tag{2.18b}$$

$$\begin{aligned}&\left(N_{xx}\frac{\partial w}{\partial x}+N_{xy}\frac{\partial w}{\partial y}+\frac{\partial M_{xx}}{\partial x}+\frac{\partial M_{xy}}{\partial y}+M_x+I_2\frac{\partial\ddot{w}}{\partial x},\right.\\ &\left.N_{xy}\frac{\partial w}{\partial x}+N_{yy}\frac{\partial w}{\partial y}+\frac{\partial M_{xy}}{\partial x}+\frac{\partial M_{yy}}{\partial y}+M_y+I_2\frac{\partial\ddot{w}}{\partial y}\right)\cdot\mathbf{n}=Q_z^S\end{aligned}$$

$$\text{or} \quad \delta w=0 \quad \text{on } S \tag{2.18c}$$

$$(M_{xx},M_{xy})\cdot\mathbf{n}=M_x^S \quad \text{or} \quad \delta\frac{\partial w}{\partial x}=0 \quad \text{on } S \tag{2.18d}$$

$$(M_{xy},M_{yy})\cdot\mathbf{n}=M_y^S \quad \text{or} \quad \delta\frac{\partial w}{\partial y}=0 \quad \text{on } S \tag{2.18e}$$

2.4 Special Governing Equations

2.4.1 Stress-Strain Relations

We consider the homogeneous and isotropic plate to be governed by linear stress-strain relations with a residual uniform and constant stress τ; that is,

$$\sigma_{xx}=\frac{E}{1-\nu^2}(\epsilon_{xx}+\nu\epsilon_{yy})+\tau \tag{2.19a}$$

$$\sigma_{yy}=\frac{E}{1-\nu^2}(\epsilon_{yy}+\nu\epsilon_{xx})+\tau \tag{2.19b}$$

$$\sigma_{xy}=2\,G\epsilon_{xy} \tag{2.19c}$$

where $G = \frac{E}{2(1+\nu)}$ is the shear modulus. Substituting Equations (2.19) into Equations (2.6), we obtain

$$N_{xx} = \int_{-\frac{h}{2}}^{\frac{h}{2}} \frac{E}{1-\nu^2}(\epsilon_{xx} + \nu\epsilon_{yy})\, dz + \tau h \tag{2.20a}$$

$$N_{yy} = \int_{-\frac{h}{2}}^{\frac{h}{2}} \frac{E}{1-\nu^2}(\epsilon_{yy} + \nu\epsilon_{xx})\, dz + \tau h \tag{2.20b}$$

$$N_{xy} = \int_{-\frac{h}{2}}^{\frac{h}{2}} 2\,G\epsilon_{xy}\, dz \tag{2.20c}$$

$$M_{xx} = \int_{-\frac{h}{2}}^{\frac{h}{2}} \frac{E}{1-\nu^2}(\epsilon_{xx} + \nu\epsilon_{yy})\, z\, dz \tag{2.20d}$$

$$M_{yy} = \int_{-\frac{h}{2}}^{\frac{h}{2}} \frac{E}{1-\nu^2}(\epsilon_{yy} + \nu\epsilon_{xx})\, z\, dz \tag{2.20e}$$

$$M_{xy} = \int_{-\frac{h}{2}}^{\frac{h}{2}} 2\,G\epsilon_{xy}\, z\, dz \tag{2.20f}$$

Substituting the expressions for ϵ_{xx}, ϵ_{yy}, and ϵ_{xy} from Equations (2.3) into Equations (2.20), we have

$$N_{xx} = \frac{Eh}{1-\nu^2}\left\{\frac{\partial u_0}{\partial x} + \frac{1}{2}\left(\frac{\partial w}{\partial x}\right)^2 + \nu\left[\frac{\partial v_0}{\partial y} + \frac{1}{2}\left(\frac{\partial w}{\partial y}\right)^2\right]\right\} + \tau h \tag{2.21a}$$

$$N_{yy} = \frac{Eh}{1-\nu^2}\left\{\frac{\partial v_0}{\partial y} + \frac{1}{2}\left(\frac{\partial w}{\partial y}\right)^2 + \nu\left[\frac{\partial u_0}{\partial x} + \frac{1}{2}\left(\frac{\partial w}{\partial x}\right)^2\right]\right\} + \tau h \tag{2.21b}$$

$$N_{xy} = Gh\left(\frac{\partial u_0}{\partial y} + \frac{\partial v_0}{\partial x} + \frac{\partial w}{\partial x}\frac{\partial w}{\partial y}\right) \tag{2.21c}$$

$$M_{xx} = -D\left(\frac{\partial^2 w}{\partial x^2} + \nu\frac{\partial^2 w}{\partial y^2}\right) \tag{2.21d}$$

$$M_{yy} = -D\left(\frac{\partial^2 w}{\partial y^2} + \nu\frac{\partial^2 w}{\partial x^2}\right) \tag{2.21e}$$

$$M_{xy} = -D\,(1-\nu)\frac{\partial^2 w}{\partial x \partial y} \tag{2.21f}$$

where $D = \frac{Eh^3}{12(1-\nu^2)}$ is the plate flexural rigidity.

2.4.2 Equation of Motion

When the in-plane natural frequencies are large compared with the transverse natural frequencies, the in-plane inertia terms in Equations (2.17a) and (2.17b) can be neglected (Ventsel

and Krauthammer, 2001). We also assume that the influence of the in-plane external forces is relatively small and therefore neglect Q_x and Q_y. Equations (2.17a) and (2.17b) then become

$$\frac{\partial N_{xx}}{\partial x} + \frac{\partial N_{xy}}{\partial y} = 0 \tag{2.22a}$$

$$\frac{\partial N_{xy}}{\partial x} + \frac{\partial N_{yy}}{\partial y} = 0 \tag{2.22b}$$

We then introduce an Airy stress function Φ associated with the deformation that satisfies these two equations by letting

$$N_{xx} = \frac{\partial^2 \Phi}{\partial y^2} + \tau h \tag{2.23a}$$

$$N_{yy} = \frac{\partial^2 \Phi}{\partial x^2} + \tau h \tag{2.23b}$$

$$N_{xy} = -\frac{\partial^2 \Phi}{\partial x \partial y} \tag{2.23c}$$

The only equation of motion left to satisfy is Equation (2.17c). We neglect the rotary and in-plane inertia terms as well as the moments (M_x and M_y) due to external forces, substitute Equations (2.23) and our moment expressions given by Equations (2.21d)-(2.21f) into Equation (2.17c), add a linear damping term, and obtain

$$D\nabla^4 w + \rho h \ddot{w} + 2c\dot{w} = \tau h \nabla^2 w + Q_z + \frac{\partial^2 \Phi}{\partial x^2}\frac{\partial^2 w}{\partial y^2} - 2\frac{\partial^2 \Phi}{\partial x \partial y}\frac{\partial^2 w}{\partial x \partial y} + \frac{\partial^2 \Phi}{\partial y^2}\frac{\partial^2 w}{\partial x^2} \tag{2.24}$$

2.4.3 Compatibility Equation

We now derive the compatibility equation that will enable Equation (2.24) to be solved for the deflection. First, we write the expressions for N_{xx}, N_{yy}, and N_{xy} in matrix form as

$$\begin{Bmatrix} N_{xx} \\ N_{yy} \\ N_{xy} \end{Bmatrix} = \frac{Eh}{1-\nu^2} \begin{bmatrix} 1 & \nu & 0 \\ \nu & 1 & 0 \\ 0 & 0 & \frac{1-\nu}{2} \end{bmatrix} \begin{Bmatrix} e_{xx} \\ e_{yy} \\ e_{xy} \end{Bmatrix} + \begin{Bmatrix} \tau h \\ \tau h \\ 0 \end{Bmatrix} \tag{2.25}$$

where

$$e_{xx} = \frac{\partial u_0}{\partial x} + \frac{1}{2}\left(\frac{\partial w}{\partial x}\right)^2 \tag{2.26a}$$

$$e_{yy} = \frac{\partial v_0}{\partial y} + \frac{1}{2}\left(\frac{\partial w}{\partial y}\right)^2 \tag{2.26b}$$

$$e_{xy} = \frac{\partial u_0}{\partial y} + \frac{\partial v_0}{\partial x} + \frac{\partial w}{\partial x}\frac{\partial w}{\partial y} \tag{2.26c}$$

Equations (2.26) satisfy

$$\frac{\partial^2 e_{xx}}{\partial y^2} + \frac{\partial^2 e_{yy}}{\partial x^2} - \frac{\partial^2 e_{xy}}{\partial x \partial y} = \left(\frac{\partial^2 w}{\partial x \partial y}\right)^2 - \frac{\partial^2 w}{\partial x^2}\frac{\partial^2 w}{\partial y^2} \tag{2.27}$$

To convert this compatibility equation to one that governs Φ, we first invert Equation (2.25) to obtain

$$\begin{Bmatrix} e_{xx} \\ e_{yy} \\ e_{xy} \end{Bmatrix} = \frac{1}{Eh}\begin{bmatrix} 1 & -\nu & 0 \\ -\nu & 1 & 0 \\ 0 & 0 & 2(1+\nu) \end{bmatrix}\begin{Bmatrix} N_{xx} - \tau h \\ N_{yy} - \tau h \\ N_{xy} \end{Bmatrix} \tag{2.28}$$

Substituting Equations (2.23) into Equation (2.28), then substituting the outcome into Equation (2.27), and rearranging the result, we rewrite the compatibility equation as

$$\nabla^4 \Phi = Eh\left[\left(\frac{\partial^2 w}{\partial x \partial y}\right)^2 - \frac{\partial^2 w}{\partial x^2}\frac{\partial^2 w}{\partial y^2}\right] \tag{2.29}$$

2.5 Governing Equations for CMUTs

The previous derivation of the equation of motion, Equation (2.24), and its corresponding compatibility equation, Equation (2.29), for a linear, homogeneous and isotropic plate was accomplished using a Cartesian coordinate system. However, we desire to use a polar coordinate system defined by

$$\hat{r}^2 = x^2 + y^2 \tag{2.30a}$$

$$\tan\theta = y/x, \quad \theta \in [0, 2\pi) \tag{2.30b}$$

to analyze the CMUT of Figure 2.2. Thus, we let Q_z in Equation (2.24) include the external force due to the electrostatic field and obtain the two governing equations in polar coordinates as

$$\begin{aligned} \rho h\frac{\partial^2 \hat{w}}{\partial \hat{t}^2} + 2\hat{c}\frac{\partial \hat{w}}{\partial \hat{t}} + D\hat{\nabla}^4\hat{w} = {} & \frac{1}{\hat{r}}\frac{\partial}{\partial \hat{r}}\left(\frac{\partial \hat{w}}{\partial \hat{r}}\frac{\partial \hat{\Phi}}{\partial \hat{r}}\right) + \frac{2}{\hat{r}^2}\left[\frac{\partial}{\partial \hat{r}}\left(\frac{1}{\hat{r}}\frac{\partial \hat{w}}{\partial \theta}\frac{\partial \hat{\Phi}}{\partial \theta}\right) - \frac{\partial^2 \hat{w}}{\partial \hat{r}\partial\theta}\frac{\partial^2 \hat{\Phi}}{\partial \hat{r}\partial\theta}\right] \\ & + \frac{1}{\hat{r}^2}\left(\frac{\partial^2 \hat{w}}{\partial \hat{r}^2}\frac{\partial^2 \hat{\Phi}}{\partial \theta^2} + \frac{\partial^2 \hat{w}}{\partial \theta^2}\frac{\partial^2 \hat{\Phi}}{\partial \hat{r}^2}\right) + \hat{\tau}h\hat{\nabla}^2\hat{w} + \hat{F} + \frac{\epsilon_0 \hat{v}^2(\hat{t})}{2(d-\hat{w})^2} \end{aligned} \tag{2.31}$$

$$\hat{\nabla}^4\hat{\Phi} = Eh\left[\left(\frac{1}{\hat{r}}\frac{\partial^2 \hat{w}}{\partial \hat{r}\partial\theta} - \frac{1}{\hat{r}^2}\frac{\partial \hat{w}}{\partial \theta}\right)^2 - \frac{\partial^2 \hat{w}}{\partial \hat{r}^2}\left(\frac{1}{\hat{r}}\frac{\partial \hat{w}}{\partial \hat{r}} + \frac{1}{\hat{r}^2}\frac{\partial^2 \hat{w}}{\partial \theta^2}\right)\right] \tag{2.32}$$

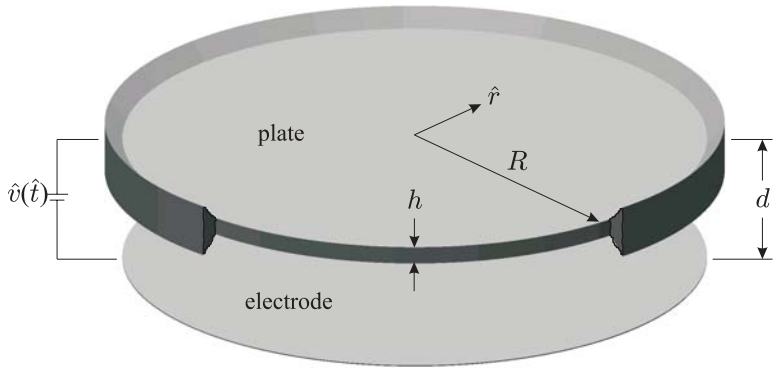

Figure 2.2: A schematic of electric actuation of a CMUT.

where the hat denotes a dimensional quantity, $\hat{w}$ is the downward deflection, $\hat{\Phi}$ is the stress function, ρ is the material mass density, E is Young's modulus, D is the plate flexural rigidity that was already defined, d is the effective gap distance between the top and bottom electrodes, ϵ_0 is the electric permittivity of the medium in the gap between the plate and electrode, $\hat{c}$ is a damping coefficient, $\hat{\tau}$ is the residual stress, $\hat{F}$ is an additional downward pressure, and $\hat{v}(\hat{t})$ is the applied voltage. Furthermore, we note that the electric forcing term in Equation (2.31) is a parallel-plate approximation to the capacitance with fringing fields ignored for a small aspect ratio ($d \ll R$) of the capacitor (Pelesko, 2001).

Chapter 3

Static Plate Deflections and Linear Vibrations

3.1 Problem Formulation

Equations (2.31) and (2.32) will be solved to yield the axisymmetric plate deflection for the clamped circular plate. The boundary conditions are

$$\hat{w}(R,\hat{t}) = 0, \frac{\partial \hat{w}(R,\hat{t})}{\partial \hat{r}} = 0, \ \hat{w}(0,\hat{t}) \text{ is bounded} \tag{3.1a}$$

$$\frac{\partial^2 \hat{\Phi}(R,\hat{t})}{\partial \hat{r}^2} - \frac{\nu}{R}\frac{\partial \hat{\Phi}(R,\hat{t})}{\partial \hat{r}} = 0, \ \hat{\Phi}(0,\hat{t}) \text{ is bounded} \tag{3.1b}$$

which render the motion axisymmetric under an axisymmetric forcing $\hat{F}(\hat{r},\hat{t})$. The biharmonic operator $\hat{\nabla}^4$ then involves only radial derivatives and becomes

$$\hat{\nabla}^4 = \left(\frac{\partial^2}{\partial \hat{r}^2} + \frac{1}{\hat{r}}\frac{\partial}{\partial \hat{r}}\right)^2$$

For convenience, we nondimensionalize the general equations according to

$$\hat{r} = R\,r, \quad \hat{t} = R^2\left(\frac{\rho h}{D}\right)^{1/2} t, \quad \hat{w} = d\,w, \quad \hat{c} = \frac{(D\rho h)^{1/2}}{R^2}\,c,$$

$$\hat{F} = \frac{Dd}{R^4}\,F, \quad \hat{v}^2(\hat{t}) = \frac{2Dd^3}{\epsilon_0 R^4}\,v^2(t), \ \hat{\tau} = \frac{D}{R^2 h}\,\tau, \quad \hat{\Phi} = Ehd^2\,\Phi \tag{3.2}$$

and transform the axisymmetric forms of Equations (2.31) and (2.32) into

$$\frac{\partial^2 w}{\partial t^2} + 2c\frac{\partial w}{\partial t} + \nabla^4 w = \frac{\beta}{r}\frac{\partial}{\partial r}\left(\frac{\partial w}{\partial r}\frac{\partial \Phi}{\partial r}\right) + \frac{\tau}{r}\frac{\partial}{\partial r}\left(r\frac{\partial w}{\partial r}\right) + F(r,t) + \frac{v^2(t)}{(1-w)^2} \tag{3.3}$$

and

$$\nabla^4 \Phi = -\frac{1}{r}\frac{\partial^2 w}{\partial r^2}\frac{\partial w}{\partial r} \tag{3.4}$$

respectively, where the nondimensional parameter β is defined as

$$\beta = 12(1-\nu^2)d^2/h^2 \tag{3.5}$$

Furthermore, the nondimensional boundary conditions become

$$w(1,t) = 0, \frac{\partial w(1,t)}{\partial r} = 0,\ w(0,t) \text{ is bounded,} \tag{3.6a}$$

$$\frac{\partial^2 \Phi(1,t)}{\partial r^2} - \nu\frac{\partial \Phi(1,t)}{\partial r} = 0,\ \Phi(0,t) \text{ is bounded} \tag{3.6b}$$

3.2 Reduced-Order Model

We approximate $w(r,t)$ as

$$w(r,t) = \sum_{m=1}^{N} \eta_m(t)\phi_m(r) \tag{3.7}$$

where $\phi_m(r)$ is the mth shape function, $\eta_m(t)$ is the mth generalized coordinate for the mth shape function, and N is the number of chosen shape functions. As N approaches infinity, the approximation in Equation (3.7) becomes exact, if the chosen shape functions form a complete set.

We choose the shape functions $\phi_m(r)$ to be the axisymmetric modes of the linear undamped case ($\beta = 0$) with zero residual stress ($\tau = 0$) and no external forcing ($F(r,t) = v(t) = 0$). For this case, $\phi_m(r)$ is the mth eigenmode given by the eigenvalue problem

$$\nabla^4 \phi_m = \Omega_m^2 \phi_m \tag{3.8}$$

and the corresponding clamped boundary conditions, where Ω_m is the nondimensional resonance frequency for $\phi_m(r)$. The solution of this eigenvalue problem can be expressed as

$$\phi_m(r) = \frac{J_0(r\sqrt{\Omega_m})}{J_0(\sqrt{\Omega_m})} - \frac{I_0(r\sqrt{\Omega_m})}{I_0(\sqrt{\Omega_m})} \tag{3.9}$$

where J_0 is the Bessel function of the first kind, I_0 is the modified Bessel function of the first kind (O'Neil, 1995), and the mode shapes are chosen to be orthonormal; that is,

$$\int_0^1 r\phi_m(r)\phi_n(r)dr = \delta_{mn} \tag{3.10}$$

where δ_{mn} is the Kronecker delta.

Next, substitution of Equation (3.7) into Equation (3.4) yields

$$\nabla^4\Phi = -\frac{1}{r}\sum_{m,n=1}^{N}\eta_m\eta_n\phi_m''\phi_n' \tag{3.11}$$

where the prime denotes differentiation with respect to the space variable r. The solution of Equations (3.6b) and (3.11) is

$$\Phi(r,t) = \sum_{m,n=1}^{N}\eta_m(t)\eta_n(t)\psi_{mn}(r) \tag{3.12}$$

where (Nayfeh and Pai, 2004)

$$\psi_{mn}'(r) = \frac{1}{4r}\int_0^r \xi\phi_m'\phi_n'd\xi + \frac{r}{4}\int_r^1 \frac{\phi_m'\phi_n'}{\xi}d\xi + \frac{r}{4}\frac{1+\nu}{1-\nu}\int_0^1 \xi\phi_m'\phi_n'd\xi \tag{3.13}$$

for $m,n = 1,2,\ldots,N$.

We then substitute Equations (3.7), (3.8), and (3.12) into Equation (3.3) and obtain

$$\begin{aligned}\sum_{m=1}^{N}\left(\ddot{\eta}_m + 2c\dot{\eta}_m + \Omega_m^2\eta_m\right)\phi_m = {} & \frac{\beta}{r}\sum_{m,n,p=1}^{N}\eta_m\eta_n\eta_p\left(\phi_m''\psi_{np}' + \phi_m'\psi_{np}''\right) \\ & + \tau\sum_{m=1}^{N}\eta_m\left(\phi_m'' + \frac{1}{r}\phi_m'\right) + F(r,t) + v^2(t)\left(1 - \sum_{i=1}^{N}\eta_i\phi_i\right)^{-2}\end{aligned} \tag{3.14}$$

where the overdot denotes differentiation with respect to the time variable t. Finally, we multiply Equation (3.14) with $\left(1-\sum_{i=1}^{N}\eta_i\phi_i\right)^2$, multiply every term by $r\phi_q(r)$, integrate

the outcome over $r \in [0,1]$, use the orthonormality condition (3.10), and obtain

$$\ddot{\eta}_q + 2c\dot{\eta}_q + \Omega_q^2\eta_q - 2\sum_{i,m=1}^{N}\left(\ddot{\eta}_m + 2c\dot{\eta}_m + \Omega_m^2\eta_m\right)\eta_i\int_0^1 r\phi_i\phi_m\phi_q dr$$

$$+\sum_{i,j,m=1}^{N}\left(\ddot{\eta}_m + 2c\dot{\eta}_m + \Omega_m^2\eta_m\right)\eta_i\eta_j\int_0^1 r\phi_i\phi_j\phi_m\phi_q dr =$$

$$\beta\Bigg(-\sum_{m,n,p=1}^{N}\eta_m\eta_n\eta_p\int_0^1\phi_q'\phi_m'\psi_{np}'dr + 2\sum_{i,m,n,p=1}^{N}\eta_i\eta_m\eta_n\eta_p\int_0^1(\phi_i\phi_q)'\,\phi_m'\psi_{np}'dr$$

$$-\sum_{i,j,m,n,p=1}^{N}\eta_i\eta_j\eta_m\eta_n\eta_p\int_0^1(\phi_i\phi_j\phi_q)'\,\phi_m'\psi_{np}'dr\Bigg) - \tau\sum_{m=1}^{N}\eta_m\int_0^1 r\phi_m'\phi_q'dr$$

$$+2\tau\sum_{i,m=1}^{N}\eta_i\eta_m\int_0^1 r\phi_m'(\phi_i\phi_q)'\,dr - \tau\sum_{i,j,m=1}^{N}\eta_i\eta_j\eta_m\int_0^1 r\phi_m'(\phi_i\phi_j\phi_q)'\,dr$$

$$+\int_0^1 Fr\phi_q dr - 2\sum_{i=1}^{N}\eta_i\int_0^1 Fr\phi_i\phi_q dr + \sum_{i,j=1}^{N}\eta_i\eta_j\int_0^1 Fr\phi_i\phi_j\phi_q dr + v^2(t)\int_0^1 r\phi_q dr \quad (3.15)$$

where $q = 1, 2, \ldots, N$. Consequently, the discretizations for $w(r,t)$ and $\Phi(r,t)$ in Equations (3.7) and (3.12), respectively, have rendered the general nonlinear partial-differential equations (3.3) and (3.4) and associated boundary conditions into the system of N coupled nonlinear ordinary-differential equations (3.15).

According to our definitions for ϕ_m and ψ_{mn}', the integrals in Equation (3.15) can be evaluated once a function $F(r,t)$ is chosen. Then, once all $\eta_m(t)$ are determined by solving Equations (3.15), the deflection $w(r,t)$ is given approximately by Equation (3.7).

3.3 Notation Simplification of System Equations

We now simplify the notation of Equation (3.15) before using it to analyze the forced vibrations of the clamped circular plate. We let

$$\psi_{mn}'(r) = \varphi_{1mn}(r) + \frac{1+\nu}{1-\nu}\varphi_{2mn}(r) \quad (3.16)$$

where

$$\varphi_{1mn}(r) = \frac{1}{4r}\int_0^r \xi\phi_m'\phi_n'd\xi + \frac{r}{4}\int_r^1 \frac{\phi_m'\phi_n'}{\xi}d\xi \quad (3.17a)$$

$$\varphi_{2mn}(r) = \frac{r}{4}\int_0^1 \xi\phi_m'\phi_n'd\xi \quad (3.17b)$$

Equation (3.15) then becomes

$$\begin{aligned}
&\left(\ddot{\eta}_q + 2c\dot{\eta}_q + \Omega_q^2\eta_q\right) - 2\left(\ddot{\eta}_m + 2c\dot{\eta}_m + \Omega_m^2\eta_m\right)\eta_i A_{imq} + \\
&\left(\ddot{\eta}_m + 2c\dot{\eta}_m + \Omega_m^2\eta_m\right)\eta_i\eta_j B_{ijmq} = \beta\Bigg[-\eta_m\eta_n\eta_p\left(C_{1mnpq} + \frac{1+\nu}{1-\nu}C_{2mnpq}\right) \\
&+ 2\eta_i\eta_m\eta_n\eta_p\left(D_{1imnpq} + \frac{1+\nu}{1-\nu}D_{2imnpq}\right) - \eta_i\eta_j\eta_m\eta_n\eta_p\Bigg(E_{1ijmnpq} \\
&+ \frac{1+\nu}{1-\nu}E_{2ijmnpq}\Bigg)\Bigg] - \tau\eta_m F_{mq} + 2\tau\eta_i\eta_m G_{imq} - \tau\eta_i\eta_j\eta_m H_{ijmq} + I_q \\
&- 2\eta_i J_{iq} + \eta_i\eta_j K_{ijq} + v^2(t)L_q
\end{aligned} \tag{3.18}$$

where

$$\begin{gathered}
A_{imq} = \int_0^1 r\phi_i\phi_m\phi_q dr, \quad B_{ijmq} = \int_0^1 r\phi_i\phi_j\phi_m\phi_q dr, \quad C_{1mnpq} = \int_0^1 \phi_q'\phi_m'\varphi_{1np} dr, \\
C_{2mnpq} = \int_0^1 \phi_q'\phi_m'\varphi_{2np} dr, \quad D_{1imnpq} = \int_0^1 (\phi_i\phi_q)'\,\phi_m'\varphi_{1np} dr, \\
D_{2imnpq} = \int_0^1 (\phi_i\phi_q)'\,\phi_m'\varphi_{2np} dr, \quad E_{1ijmnpq} = \int_0^1 (\phi_i\phi_j\phi_q)'\,\phi_m'\varphi_{1np} dr, \\
E_{2ijmnpq} = \int_0^1 (\phi_i\phi_j\phi_q)'\,\phi_m'\varphi_{2np} dr, \quad F_{mq} = \int_0^1 r\phi_m'\phi_q' dr, \\
G_{imq} = \int_0^1 r\phi_m'\,(\phi_i\phi_q)'\,dr, \quad H_{ijmq} = \int_0^1 r\phi_m'\,(\phi_i\phi_j\phi_q)'\,dr, \quad I_q = \int_0^1 Fr\phi_q dr, \\
J_{iq} = \int_0^1 Fr\phi_i\phi_q dr, \quad K_{ijq} = \int_0^1 Fr\phi_i\phi_j\phi_q dr, \quad L_q = \int_0^1 r\phi_q dr
\end{gathered} \tag{3.19}$$

for $q = 1, 2, \ldots, N$, and the summation signs have been removed in Equation (3.18) for notation simplification. Therefore, all terms in Equation (3.18) are created by summing over their respective lower-case Latin indices (excluding q), which range from 1 to N. Furthermore, because all integrands in Equations (3.19) are known explictly after a function $F(r,t)$ is chosen, the integrals can be evaluated numerically *one time* and saved for future use. Thus, the variables with upper-case Latin names in Equation (3.18) are known.

Finally, we simplify the form of Equation (3.18) by putting the N coupled equations ($q = 1, 2, \ldots, N$) in matrix form. We collect all $\eta_i(t)$ into a column vector $\boldsymbol{\eta}(t)$; that is,

$$\boldsymbol{\eta}(t) = \{\eta_1(t),\ \eta_2(t), \ldots,\ \eta_N(t)\} \tag{3.20}$$

and then rearrange Equation (3.18) to obtain

$$M(\boldsymbol{\eta})\ddot{\boldsymbol{\eta}} + 2cM(\boldsymbol{\eta})\dot{\boldsymbol{\eta}} + N(\boldsymbol{\eta})\boldsymbol{\eta} = P(\boldsymbol{\eta}) + v^2(t)\boldsymbol{L} \tag{3.21}$$

where

$$M(\boldsymbol{\eta}) = [M_{qs}(\boldsymbol{\eta})] = [\delta_{qs} - 2\eta_i A_{isq} + \eta_i\eta_j B_{ijsq}] \tag{3.22a}$$

$$N(\boldsymbol{\eta}) = [N_{qs}(\boldsymbol{\eta})] = [\Omega_q^2\delta_{qs} - 2\Omega_s^2\eta_i A_{isq} + \Omega_s^2\eta_i\eta_j B_{ijsq}] \tag{3.22b}$$

$$\begin{aligned} P(\boldsymbol{\eta}) = \{P_q(\boldsymbol{\eta})\} = \Bigg\{ & \beta\Bigg[- \eta_m\eta_n\eta_p\left(C_{1mnpq} + \frac{1+\nu}{1-\nu}C_{2mnpq}\right) \\ & + 2\eta_i\eta_m\eta_n\eta_p\left(D_{1imnpq} + \frac{1+\nu}{1-\nu}D_{2imnpq}\right) \\ & - \eta_i\eta_j\eta_m\eta_n\eta_p\left(E_{1ijmnpq} + \frac{1+\nu}{1-\nu}E_{2ijmnpq}\right)\Bigg] \\ & - \tau\eta_m F_{mq} + 2\tau\eta_i\eta_m G_{imq} - \tau\eta_i\eta_j\eta_m H_{ijmq} \\ & + I_q - 2\eta_i J_{iq} + \eta_i\eta_j K_{ijq}\Bigg\} \end{aligned} \tag{3.22c}$$

$$\boldsymbol{L} = \{L_q\} \tag{3.22d}$$

and δ_{qs} is the Kronecker delta. Also, the summation signs have been removed in Equations (3.22) for notation simplification, as in Equation (3.18). Hence, once all $\eta_m(t)$ are determined by solving the nonlinear matrix equation (3.21), the plate deflection $w(r,t)$ is given approximately by Equation (3.7).

3.4 Static Behavior Under Electrostatic Actuation

By letting both $\eta_m(t)$ and $v(t)$ be independent of time, setting all time derivatives equal to zero, and letting the function $F(r,t)$ be zero, we reduce Equations (3.15) to a system of coupled algebraic equations. Once we choose values for the parameters β, ν, τ, N and the time-independent electric potential v, we can solve for all time-independent η_m to obtain the static deflection from Equation (3.7). For example, Figure 3.1 shows variation of the maximum static deflection $w_{\max}$ (at $r = 0$) with the electric forcing v^2 for $\beta = 1.0$, $\nu = 0.25$, $\tau = 0$, and various values of N. The solid branches in Figure 3.1 are stable whereas the dashed branches are unstable.

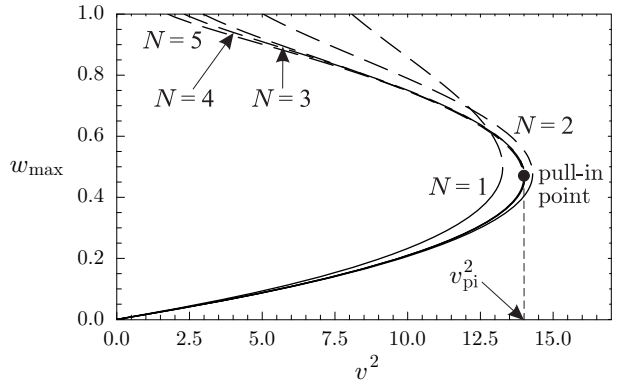

Figure 3.1: Deflection at the plate center versus electric forcing.

Upon comparison of the curves in Figure 3.1, we conclude that using three modes for discretizing $w(r,t)$ can be sufficient to model adequately the static deflection of the clamped circular plate over its stable physical range. Clearly, the solution converges as the number of modes increases. In fact, the curve for six modes ($N = 6$) was not plotted in Figure 3.1 because it could not be distinguished from the curve for five modes ($N = 5$). Furthermore, the unstable solution approaches the approximate physical deflection limit of $w = 1$, where the circular plate center almost contacts the electrode, from the right as N increases. Also, the slope of all curves becomes infinite at the pull-in point, as expected, when the voltage v approaches the critical nondimensional pull-in voltage v_{pi}.

3.5 Validation of Pull-in Values

Now that we have modeled the static deflection, we validate the model with experimental data. Osterberg (1995) measured the pull-in voltage $\hat{v}_{\text{pi}}$ for various radii R of clamped circular plates made of silicon. These MEMS have a thickness h of about 3 μm with an initial, undeformed gap width d of about 1 μm. Osterberg developed a statistics-based model to approximate $\hat{v}_{\text{pi}}$ and solved for the optimal statistical coefficients by fitting his model to the experimental data. We fit our physics-based model to the experimental data by solving

for the values of E, $\hat{\tau}$, ν, d, and h that minimize the objective function

$$W = \sum_{i=1}^{14} \left(\frac{\hat{v}_i^{\text{model}}(E, \hat{\tau}, \nu, d, h) - \hat{v}_i^{\text{exp}}}{\delta_i} \right)^2 \tag{3.23}$$

where the $\delta_i, \hat{v}_i^{\text{model}}$, and $\hat{v}_i^{\text{exp}}$ are the respective experimental standard deviations, model pull-in values, and experimental pull-in values for the 14 different experimental radii. We found the global minimum of W for $d = 1.014$ μm, $h = 3.01$ μm, $E = 150.6$ GPa, $\nu = 0.0436$, and $\hat{\tau} = 7.82$ MPa. The pull-in voltages from this optimum model are displayed in Figure 3.2 along with the experimental data. Standard deviation bars for the experimental data are also shown in the figure. The average percentage deviation of the optimum values from the experimental values is 2.54%. The optimum fit (dashed curve) from the reduced-order model matches fairly well the experimental data curve (solid curve) in Figure 3.2 for all radii.

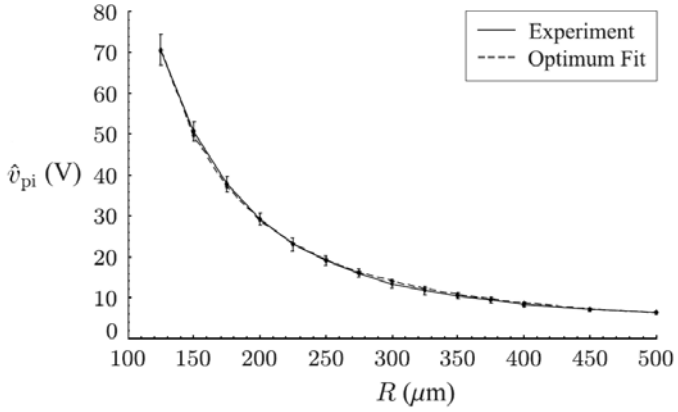

Figure 3.2: Variation of the pull-in voltage with the plate radius obtained experimentally (Osterberg, 1995) and theoretically using the optimum macromodel.

Because Osterberg's values are based on his beam analysis, it seems reasonable that our optimum values for clamped circular plates do not match fully with his beam-dependent values. Furthermore, instead of letting ν vary, Osterberg set $\nu = 0.06$ or $\nu = 0.32$ in his numerical simulations. Because the optimum value of 0.0436 for ν is much closer to 0.06 than to 0.32, the optimum ν seems to be physically reasonable. Consequently, our reduced-order model is adequate for determining the material properties (Young's modulus E, Poisson's ratio ν, and residual stress $\hat{\tau}$) and geometric properties (thickness h and gap width d) of the

system through use of the experimental pull-in data.

The reduced-order model pull-in values are also comparable to those obtained from full 3-D electromechanical simulations. For a clamped circular plate with $d = 1$ μm, $h = 20$ μm, $E = 169$ GPa, and $\nu = 0.3$, we use our macromodel and Osterberg's model to calculate the pull-in voltage $\hat{v}_{\text{pi}}$ for both $\hat{\tau} = 0$ and $\hat{\tau} = 500$ MPa. The results are given in Table 3.1 along with the pull-in voltages from CoSolve-EM simulations (Osterberg, 1995). The macromodel pull-in values deviate by 1.2% from the full 3-D simulation values produced by CoSolve-EM. Most of the deviation between the macromodel and simulation values might be caused by the parallel-plate approximation assumed for the capacitance. Specifically, the macromodel pull-in values are lower than the simulation values because the total electrostatic force is overestimated due to the parallel-plate approximation. Yet, even with the parallel-plate approximation, the macromodel accurately predicts the pull-in voltage of a clamped circular plate under an electrostatic actuation.

Table 3.1: Comparison between model and simulation pull-in voltages.

$\hat{\tau}$ (MPa)	$\hat{v}_{\text{pi}}$ (V) Osterberg [O]	$\hat{v}_{\text{pi}}$ (V) Vogl [V]	$\hat{v}_{\text{pi}}$ (V) CoSolve [C]	Δ% between O and C	Δ% between V and C
0	313	315	319	2.0	1.2
500	362	364	369	1.8	1.2

3.6 Natural Frequencies

In this section, we determine the natural frequencies of the axisymmetric modes of the deflected plate due to an electrostatic actuation. First, we perturb each coefficient function $\eta_m(t)$ with a harmonic term $\mathrm{e}^{\mathrm{i}\omega t}$ from its equilibrium value η_m^{eq}, such that

$$\eta_m(t) = \eta_m^{\text{eq}} + \xi_m \mathrm{e}^{\mathrm{i}\omega t} \tag{3.24}$$

where ξ_m is the mode shape corresponding to the frequency ω. Then, substituting Equation (3.24) into the reduced-order model (3.15) yields an eigenvalue problem for the N unique

frequencies and modes of vibration for the stable deformed state.

Figure 3.3 shows variation of the first three nondimensional axisymmetric natural frequencies associated with the stable deflected equilibrium for a given system. A close-up of the fundamental natural frequency is also included. The fundamental natural frequency decreases as the electric forcing v increases, reaching a value of zero at pull-in, as seen in Figure 3.3(b). The fundamental natural frequency is zero at pull-in because the general restoring force of the clamped plate is negated by the equal and opposite force from the electrode at pull-in. However, the frequencies do not always decrease monotonically to zero as pull-in is approached. The effect of the first geometric nonlinearity of the von Kármán type is related to β, as seen in Equation (3.3). Not only do the pull-in voltages increase with β, but the frequencies can also increase with voltage due to strain hardening, as seen in Figure 3.4.

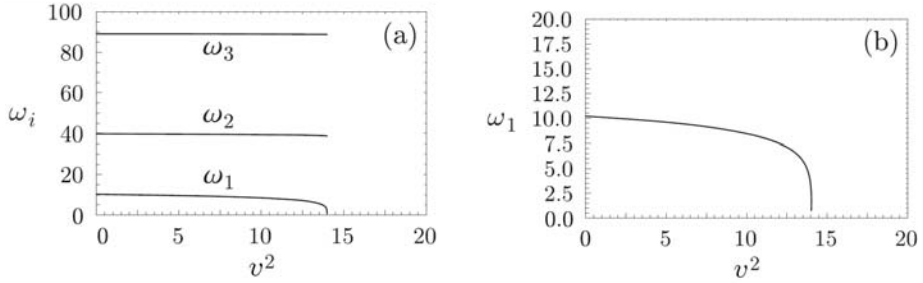

Figure 3.3: (a) The first three natural frequencies and (b) the fundamental natural frequency versus electric forcing for $\beta = 1$, $\nu = 0.25$, $\tau = 0$, and $F(r,t) = 0$.

The reduced-order model has one main computational advantage over other models with respect to the calculation of the natural frequencies. As with the model developed by Younis et al. (2003), the natural frequencies near pull-in can be calculated from the reduced-order model as easily as those well before pull-in. Consequently, the reduced-order model is robust because it does not suffer from numerical stiffness when calculating the natural frequencies. The computational time is then relatively low compared to other methods, such as the shooting method (Nayfeh and Balachandran, 1995), which is used by Faris et al. (2002) to solve an eigenvalue problem for a clamped circular plate.

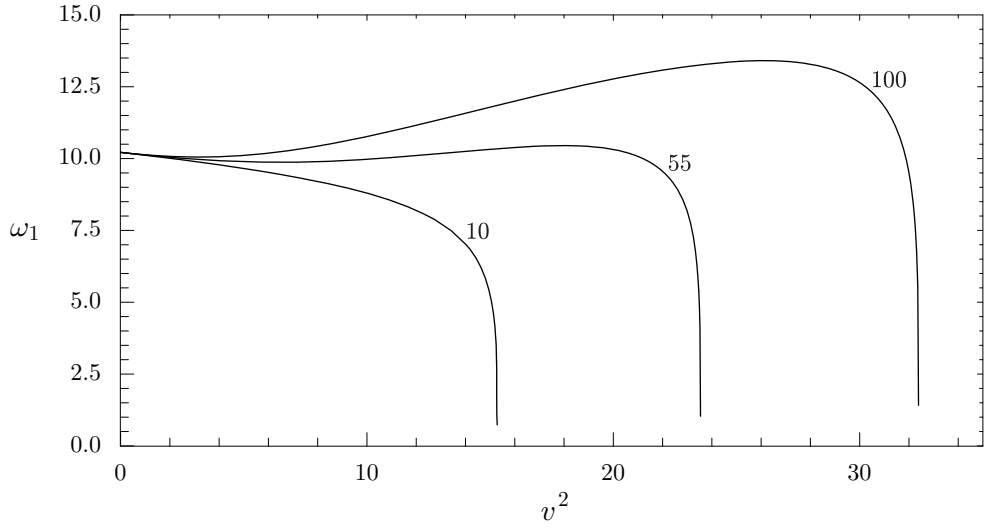

Figure 3.4: Fundamental natural frequency for various β with $\nu = 0.25$, $\tau = 0$, and $F(r,t) = 0$.

Chapter 4

Nonlinear Resonance Theory

4.1 Primary Resonance of First Mode

We now investigate the response of the clamped CMUT to a primary resonance excitation of the first mode, the main mode of excitation for CMUTs. Hence, we let the voltage $v(t)$ be

$$v(t) = \chi_0 + \chi_3 \cos(\omega_f t) \tag{4.1}$$

where the forcing frequency ω_f is defined as

$$\omega_f = \omega_1 + \sigma \tag{4.2}$$

and the *detuning parameter* σ represents how far the forcing frequency is from the first natural frequency ω_1 of the plate around its deformed equilibrium state. Physically, the parameters χ_0 and χ_3 are associated with the DC and AC voltage components, respectively. The nondimensional DC voltage χ_0 causes the plate to deform towards the fixed electrode, and the first frequency ω_1 is then determined for the deflected equilibrium.

4.2 Method of Multiple Scales

Different techniques can be used to solve the nonlinear matrix equation (3.21) with the forcing in Equation (4.1). For example, after all necessary parameters are chosen, a straightforward numerical integration can be used to solve the matrix equation for the generalized vector

$\boldsymbol{\eta}(t)$. The approximate deflection $w(r,t)$ for a specific system is then known according to Equation (3.7). While correct, this computational method needs to be repeated if the geometric, material, or forcing parameters change. In contrast, the method of multiple scales (MMS) (Nayfeh, 1973, 1981) can be used to yield uniformly valid approximate solutions for general parameters, which might be useful for design purposes of CMUTs.

The main goal of the method of multiple scales is to derive an asymptotically uniform solution of a given problem. For some problems, a naturally small parameter ϵ causes the solution $\boldsymbol{\eta}$ to be a perturbation from the equilibrium solution $\boldsymbol{\eta}_0$ for zero ϵ. In this spirit, we seek an asymptotic expansion in the form

$$\boldsymbol{\eta}(t;\epsilon) = \boldsymbol{\eta}_0 + \epsilon\boldsymbol{\eta}_1(t;\epsilon) + \epsilon^2\boldsymbol{\eta}_2(t;\epsilon) + \epsilon^3\boldsymbol{\eta}_3(t;\epsilon) + O(\epsilon^4) \tag{4.3}$$

where ϵ is a small bookkeeping parameter that we created to keep track of the order of the different terms. The solution should also be uniform in the sense that every $\boldsymbol{\eta}_i$ is bounded for all time t.

4.2.1 Scaling and Balancing

Somehow, the parameter ϵ modifies the functional dependence of $\boldsymbol{\eta}_i$ on time t. This fact is revealed in the analytical solutions of many benchmark problems (like oscillations of linear systems with small damping), where terms like ϵt and $\epsilon^2 t$ appear. Following the method of multiple scales, we use this as inspiration to create multiple time scales that depend on ϵ. We let

$$T_0 = t, \;\; T_1 = \epsilon t, \;\; T_2 = \epsilon^2 t, \;\; \ldots \tag{4.4}$$

and let the solution (4.3) depend explicitly on these time scales; that is,

$$\begin{aligned}\boldsymbol{\eta}(t;\epsilon) = \boldsymbol{\eta}_0 + \epsilon\boldsymbol{\eta}_1(T_0, T_1, T_2, \ldots) + \epsilon^2\boldsymbol{\eta}_2(T_0, T_1, T_2, \ldots) \\ + \epsilon^3\boldsymbol{\eta}_3(T_0, T_1, T_2, \ldots) + O(\epsilon^4)\end{aligned} \tag{4.5}$$

Every $\boldsymbol{\eta}_i$ is of $O(1)$ and depends on ϵ only implicitly through the time scales.

When we substitute Equation (4.5) into Equation (3.21), the ordinary-differential matrix equation will become a partial-differential matrix equation with respect to the time scales

in Equations (4.4). Terms of $O(1)$, $O(\epsilon)$, $O(\epsilon^2)$, etc. will also be seen peppered throughout the matrix equation. To render its solution to be asymptotic, we will generate an equation for each order of ϵ by equating terms of like order on both sides of the matrix equation. All equations will then be solved sequentially in increasing order of ϵ, and at some order, *modulation equations* will be derived that govern the temporal evolution of $\boldsymbol{\eta}_1$. At this order, the damping, nonlinearities, and forcing terms "balance" each other, which means that $\boldsymbol{\eta}$ will be uniform (as required).

However, balancing only occurs if terms are scaled correctly. For our problem, we scale coefficients and functions *a priori* as

$$c \to \epsilon^2 c, \quad \chi_3 \to \epsilon^3 \chi_3, \quad \text{and} \quad \sigma \to \epsilon^2 \sigma \tag{4.6}$$

such that the system to be solved becomes

$$M(\boldsymbol{\eta})\ddot{\boldsymbol{\eta}} + 2\epsilon^2 c M(\boldsymbol{\eta})\dot{\boldsymbol{\eta}} + N(\boldsymbol{\eta})\boldsymbol{\eta} = P(\boldsymbol{\eta}) + v^2(t)\boldsymbol{L} \tag{4.7}$$

where

$$v(t) = \chi_0 + \epsilon^3 \chi_3 \cos(\omega_f t) \tag{4.8}$$

and

$$\omega_f = \omega_1 + \epsilon^2 \sigma \tag{4.9}$$

With the scaled system in Equations (4.7)-(4.9), our modulation equations will be obtained at $O(\epsilon^3)$. Consequently, we can produce a second-order uniform approximation of Equation (4.7). We then truncate the solution in Equation (4.5) *a priori* at $O(\epsilon^3)$ and neglect time scales T_3, T_4, etc. to obtain the approximation that we seek; that is,

$$\boldsymbol{\eta}(t;\epsilon) = \underbrace{\boldsymbol{\eta}_0 + \epsilon\boldsymbol{\eta}_1(T_0, T_1, T_2) + \epsilon^2\boldsymbol{\eta}_2(T_0, T_1, T_2)}_{\text{approximation to be solved}} + \epsilon^3\boldsymbol{\eta}_3(T_0, T_1, T_2) \tag{4.10}$$

We are almost ready to substitute Equations (4.8) and (4.10) into Equation (4.7) and derive our modulation equations that govern the solution $\boldsymbol{\eta}$ and reveal how the plate responds to a primary excitation. Before we do so, we need to make sure that $v(t)$ is a function of the time scales (and not time t) so that Equation (4.7) will become a partial-differential

equation. By using the time scales in Equations (4.4), we combine ϵ^2 and t and rearrange $v(t)$ in Equation (4.8) to be

$$v(t) = \chi_0 + \epsilon^3 \chi_3 \frac{1}{2}\Big(e^{i\sigma T_2} e^{i\omega_1 T_0} + e^{-i\sigma T_2} e^{-i\omega_1 T_0}\Big) \tag{4.11}$$

where an exponential form of the cosine function has been used to simplify future use of the equation. Furthermore, because every function now depends on the time scales T_0, T_1, and T_2, the time derivative operator $\frac{d}{dt}$ is transformed into

$$\begin{aligned} \frac{d}{dt} &= \frac{\partial}{\partial T_0}\frac{dT_0}{dt} + \frac{\partial}{\partial T_1}\frac{dT_1}{dt} + \frac{\partial}{\partial T_2}\frac{dT_2}{dt} \\ &= D_0 + \epsilon D_1 + \epsilon^2 D_2 \end{aligned} \tag{4.12}$$

according to the chain rule of differentiation where $D_i = \frac{\partial}{\partial T_i}$. Moreover, the operator $\frac{d^2}{dt^2}$ is transformed into

$$\begin{aligned} \frac{d^2}{dt^2} &= \frac{d}{dt}\left(\frac{d}{dt}\right) = (D_0 + \epsilon D_1 + \epsilon^2 D_2)^2 \\ &= D_0^2 + 2\epsilon D_1 D_0 + \epsilon^2 (D_1^2 + 2 D_2 D_0) + O(\epsilon^3) \end{aligned} \tag{4.13}$$

4.2.2 Ordered System of Equations

MMS is now used to investigate the primary resonance of the first mode. We substitute the voltage $v(t)$ from Equation (4.11) into Equation (4.7), expand all matrices and vectors that are functions of $\boldsymbol{\eta}$ in Taylor series, collect coefficients of like powers of ϵ up to $O(\epsilon^3)$, and

obtain the following equations:

$$O(1): \qquad N_0\,\boldsymbol{\eta}_0 - \boldsymbol{P}_0 - \chi_0^2 \boldsymbol{L} = \boldsymbol{0} \tag{4.14}$$

$$O(\epsilon): \qquad M_0\,D_0^2\boldsymbol{\eta}_1 + N_0\,\boldsymbol{\eta}_1 + N_1(\boldsymbol{\eta}_1)\,\boldsymbol{\eta}_0 - P_1\,\boldsymbol{\eta}_1 = \boldsymbol{0} \tag{4.15}$$

$$\begin{aligned} O(\epsilon^2): \qquad & M_0\,D_0^2\boldsymbol{\eta}_2 + N_0\,\boldsymbol{\eta}_2 + N_1(\boldsymbol{\eta}_2)\,\boldsymbol{\eta}_0 - P_1\,\boldsymbol{\eta}_2 = -2M_0\,D_0D_1\boldsymbol{\eta}_1 \\ & - M_1(\boldsymbol{\eta}_1)\,D_0^2\boldsymbol{\eta}_1 - N_1(\boldsymbol{\eta}_1)\,\boldsymbol{\eta}_1 - N_2(\boldsymbol{\eta}_1,\boldsymbol{\eta}_1)\,\boldsymbol{\eta}_0 + \boldsymbol{P}_2(\boldsymbol{\eta}_1,\boldsymbol{\eta}_1) \end{aligned} \tag{4.16}$$

$$\begin{aligned} O(\epsilon^3): \qquad & M_0\,D_0^2\boldsymbol{\eta}_3 + N_0\,\boldsymbol{\eta}_3 + N_1(\boldsymbol{\eta}_3)\,\boldsymbol{\eta}_0 - P_1\,\boldsymbol{\eta}_3 = -2cM_0\,D_0\boldsymbol{\eta}_1 \\ & - 2M_0\,D_0D_1\boldsymbol{\eta}_2 - M_0\,D_1^2\boldsymbol{\eta}_1 - 2M_0\,D_0D_2\boldsymbol{\eta}_1 - M_1(\boldsymbol{\eta}_1)\,D_0^2\boldsymbol{\eta}_2 \\ & - 2M_1(\boldsymbol{\eta}_1)\,D_0D_1\boldsymbol{\eta}_1 - M_1(\boldsymbol{\eta}_2)\,D_0^2\boldsymbol{\eta}_1 - M_2(\boldsymbol{\eta}_1,\boldsymbol{\eta}_1)\,D_0^2\boldsymbol{\eta}_1 \\ & - N_1(\boldsymbol{\eta}_1)\,\boldsymbol{\eta}_2 - N_1(\boldsymbol{\eta}_2)\,\boldsymbol{\eta}_1 - N_2(\boldsymbol{\eta}_1,\boldsymbol{\eta}_1)\,\boldsymbol{\eta}_1 - 2N_2(\boldsymbol{\eta}_1,\boldsymbol{\eta}_2)\,\boldsymbol{\eta}_0 \\ & - N_3(\boldsymbol{\eta}_1,\boldsymbol{\eta}_1,\boldsymbol{\eta}_1)\,\boldsymbol{\eta}_0 + 2\boldsymbol{P}_2(\boldsymbol{\eta}_1,\boldsymbol{\eta}_2) + \boldsymbol{P}_3(\boldsymbol{\eta}_1,\boldsymbol{\eta}_1,\boldsymbol{\eta}_1) \\ & + \chi_0\chi_3\Big(e^{i\sigma T_2}e^{i\omega_1 T_0} + e^{-i\sigma T_2}e^{-i\omega_1 T_0}\Big)\boldsymbol{L} \end{aligned} \tag{4.17}$$

where $\boldsymbol{0}$ is the zero vector of length N,

$$M_0 = M(\boldsymbol{\eta}_0), \quad N_0 = N(\boldsymbol{\eta}_0), \quad \boldsymbol{P}_0 = \boldsymbol{P}(\boldsymbol{\eta}_0) \tag{4.18a}$$

$$M_1(\boldsymbol{x}) = \left[\frac{\partial M}{\partial \eta_i}\boldsymbol{x}_i\right]\Bigg|_{\boldsymbol{\eta}_0}, \quad N_1(\boldsymbol{x}) = \left[\frac{\partial N}{\partial \eta_i}\boldsymbol{x}_i\right]\Bigg|_{\boldsymbol{\eta}_0}, \quad P_1 = [P_{1ij}] = \left[\frac{\partial \boldsymbol{P}_i}{\partial \eta_j}\right]\Bigg|_{\boldsymbol{\eta}_0} \tag{4.18b}$$

$$M_2(\boldsymbol{x},\boldsymbol{y}) = \left[\frac{1}{2}\frac{\partial^2 M}{\partial \eta_i \partial \eta_j}\boldsymbol{x}_i\boldsymbol{y}_j\right]\Bigg|_{\boldsymbol{\eta}_0}, \quad N_2(\boldsymbol{x},\boldsymbol{y}) = \left[\frac{1}{2}\frac{\partial^2 N}{\partial \eta_i \partial \eta_j}\boldsymbol{x}_i\boldsymbol{y}_j\right]\Bigg|_{\boldsymbol{\eta}_0} \tag{4.18c}$$

$$\boldsymbol{P}_2(\boldsymbol{x},\boldsymbol{y}) = \{P_{2k}(\boldsymbol{x},\boldsymbol{y})\} = \left\{\frac{1}{2}\frac{\partial^2 \boldsymbol{P}_k}{\partial \eta_i \partial \eta_j}\boldsymbol{x}_i\boldsymbol{y}_j\right\}\Bigg|_{\boldsymbol{\eta}_0} \tag{4.18d}$$

$$N_3(\boldsymbol{x},\boldsymbol{y},\boldsymbol{z}) = \left[\frac{1}{6}\frac{\partial^3 N}{\partial \eta_i \partial \eta_j \partial \eta_k}\boldsymbol{x}_i\boldsymbol{y}_j\boldsymbol{z}_k\right]\Bigg|_{\boldsymbol{\eta}_0} \tag{4.18e}$$

$$\boldsymbol{P}_3(\boldsymbol{x},\boldsymbol{y},\boldsymbol{z}) = \{P_{3k}(\boldsymbol{x},\boldsymbol{y},\boldsymbol{z})\} = \left[\frac{1}{6}\frac{\partial^3 \boldsymbol{P}_k}{\partial \eta_i \partial \eta_j \partial \eta_k}\boldsymbol{x}_i\boldsymbol{y}_j\boldsymbol{z}_k\right]\Bigg|_{\boldsymbol{\eta}_0} \tag{4.18f}$$

and $\boldsymbol{v}_i$ is the ith component of a general vector $\boldsymbol{v}$. We note that Einstein's summation convention is used in Equations (4.18).

Before solving the ordered equations (4.14)-(4.17), we rearrange the left-hand sides of the

equations of $O(\epsilon)$ and greater. By definition,

$$\begin{aligned} N_1(\boldsymbol{x})\,\boldsymbol{\eta}_0 &= \left[\frac{\partial N}{\partial \eta_i}\boldsymbol{x}_i\right]\boldsymbol{\eta}_0 \\ &= \left\{\frac{\partial N}{\partial \eta_1}\boldsymbol{\eta}_0\right\}\boldsymbol{x}_1 + \left\{\frac{\partial N}{\partial \eta_2}\boldsymbol{\eta}_0\right\}\boldsymbol{x}_2 + \cdots + \left\{\frac{\partial N}{\partial \eta_N}\boldsymbol{\eta}_0\right\}\boldsymbol{x}_N \\ &= \left[\left\{\frac{\partial N}{\partial \eta_1}\boldsymbol{\eta}_0\right\}\ \left\{\frac{\partial N}{\partial \eta_2}\boldsymbol{\eta}_0\right\}\ \cdots\ \left\{\frac{\partial N}{\partial \eta_N}\boldsymbol{\eta}_0\right\}\right]\boldsymbol{x} \end{aligned}$$

Therefore, for a general $\boldsymbol{\eta}_i$,

$$N_1(\boldsymbol{\eta}_i)\,\boldsymbol{\eta}_0 = Q_0\,\boldsymbol{\eta}_i \tag{4.19}$$

where

$$Q_0 = \left[\left\{\frac{\partial N}{\partial \eta_1}\boldsymbol{\eta}_0\right\}\ \left\{\frac{\partial N}{\partial \eta_2}\boldsymbol{\eta}_0\right\}\ \cdots\ \left\{\frac{\partial N}{\partial \eta_N}\boldsymbol{\eta}_0\right\}\right]\Bigg|_0 \tag{4.20}$$

Our ordered equations are then rewritten as

$$O(1): \qquad N_0\,\boldsymbol{\eta}_0 - \boldsymbol{P}_0 - \chi_0^2\boldsymbol{L} = \boldsymbol{0} \tag{4.21}$$

$$O(\epsilon): \qquad M_0\,D_0^2\boldsymbol{\eta}_1 + R_0\,\boldsymbol{\eta}_1 = \boldsymbol{0} \tag{4.22}$$

$$\begin{aligned} O(\epsilon^2): \qquad & M_0\,D_0^2\boldsymbol{\eta}_2 + R_0\,\boldsymbol{\eta}_2 = -2M_0\,D_0D_1\boldsymbol{\eta}_1 - M_1(\boldsymbol{\eta}_1)\,D_0^2\boldsymbol{\eta}_1 \\ & - N_1(\boldsymbol{\eta}_1)\,\boldsymbol{\eta}_1 - N_2(\boldsymbol{\eta}_1,\boldsymbol{\eta}_1)\,\boldsymbol{\eta}_0 + \boldsymbol{P}_2(\boldsymbol{\eta}_1,\boldsymbol{\eta}_1) \end{aligned} \tag{4.23}$$

$$\begin{aligned} O(\epsilon^3): \qquad & M_0\,D_0^2\boldsymbol{\eta}_3 + R_0\,\boldsymbol{\eta}_3 = -2cM_0\,D_0\boldsymbol{\eta}_1 - 2M_0\,D_0D_1\boldsymbol{\eta}_2 - M_0\,D_1^2\boldsymbol{\eta}_1 \\ & - 2M_0\,D_0D_2\boldsymbol{\eta}_1 - M_1(\boldsymbol{\eta}_1)\,D_0^2\boldsymbol{\eta}_2 - 2M_1(\boldsymbol{\eta}_1)\,D_0D_1\boldsymbol{\eta}_1 \\ & - M_1(\boldsymbol{\eta}_2)\,D_0^2\boldsymbol{\eta}_1 - M_2(\boldsymbol{\eta}_1,\boldsymbol{\eta}_1)\,D_0^2\boldsymbol{\eta}_1 - N_1(\boldsymbol{\eta}_1)\,\boldsymbol{\eta}_2 \\ & - N_1(\boldsymbol{\eta}_2)\,\boldsymbol{\eta}_1 - N_2(\boldsymbol{\eta}_1,\boldsymbol{\eta}_1)\,\boldsymbol{\eta}_1 - 2N_2(\boldsymbol{\eta}_1,\boldsymbol{\eta}_2)\,\boldsymbol{\eta}_0 \\ & - N_3(\boldsymbol{\eta}_1,\boldsymbol{\eta}_1,\boldsymbol{\eta}_1)\,\boldsymbol{\eta}_0 + 2\boldsymbol{P}_2(\boldsymbol{\eta}_1,\boldsymbol{\eta}_2) + \boldsymbol{P}_3(\boldsymbol{\eta}_1,\boldsymbol{\eta}_1,\boldsymbol{\eta}_1) \\ & + \chi_0\chi_3\Big(e^{i\sigma T_2}e^{i\omega_1 T_0} + e^{-i\sigma T_2}e^{-i\omega_1 T_0}\Big)\boldsymbol{L} \end{aligned} \tag{4.24}$$

where $R_0 = N_0 - P_1 + Q_0$.

4.2.3 Solutions of Ordered Equations

We now solve the ordered equations (4.21)-(4.24) sequentially, starting with the $O(1)$ equation. The equations are solved symbolically here and numerical solutions will be generated afterwards.

$\underline{O(1)}$

If χ_0 is less than its pull-in value χ_0^{pi}, the nondimensional DC voltage χ_0 causes the CMUT plate to reach a new static equilibrium state after the plate deforms towards the bottom electrode. Because Equation (4.21) is a nonlinear matrix equation, we assume at this point that a numerical solution of $\boldsymbol{\eta}_0$ is known for the static equilibrium and move on to solve the $O(\epsilon)$ equation with this assumed solution.

$\underline{O(\epsilon)}$

The $O(\epsilon)$ equation, Equation (4.22), can be rearranged as

$$D_0^2\boldsymbol{\eta}_1 + S_0\,\boldsymbol{\eta}_1 = \mathbf{0} \tag{4.25}$$

where $S_0 = M_0^{-1}R_0$ and is determined by using the $O(1)$ solution $\boldsymbol{\eta}_0$. Seeking solutions of Equation (4.25) in the form $\boldsymbol{\eta}_1 = A(T_1,T_2)e^{i\omega T_0}\boldsymbol{p}$, we obtain the eigenvalue problem

$$S_0\,\boldsymbol{p} = \omega^2\boldsymbol{p} \tag{4.26}$$

Collecting the real eigenvalues ω_1^2, ω_2^2, $\ldots$, ω_N^2 and associated real eigenvectors $\boldsymbol{p}_1$, $\boldsymbol{p}_2$, $\ldots$, $\boldsymbol{p}_N$, which represent the undamped natural frequencies and mode shapes around the deflected configuration, respectively, we obtain

$$\boldsymbol{\eta}_1 = \sum_{k=1}^{N}\left(A_k(T_1,T_2)e^{i\omega_k T_0}\boldsymbol{p}_k + \bar{A}_k(T_1,T_2)e^{-i\omega_k T_0}\boldsymbol{p}_k\right) \tag{4.27}$$

according to the superposition principle, where A_k is a complex measure of the vibration amplitude of the kth mode and the overbar denotes the complex conjugate of an expression.

Now, because in the presence of damping all of the modes that are not directly or indirectly excited decay with time (Nayfeh, 2000; Nayfeh and Mook, 1979), the dynamical long-term solution of the $O(\epsilon)$ equation consists of the modes that are only excited directly or indirectly (via internal resonance). In other words, if the kth mode is not excited, then $A_k = 0$ as $t \to \infty$. Assuming that no mode is involved in an internal resonance with the directly excited first mode, we conclude that $A_k = 0$ for $k \neq 1$ after a long time. Therefore, the solution *a priori* of Equation (4.25) is

$$\boldsymbol{\eta}_1 = A(T_1,T_2)e^{i\omega_1 T_0}\boldsymbol{p}_1 + \bar{A}(T_1,T_2)e^{-i\omega_1 T_0}\boldsymbol{p}_1 \tag{4.28}$$

Because ω_1 and $\boldsymbol{p}_1$ are known, we only need to solve for $A(T_1, T_2)$ to determine $\boldsymbol{\eta}_1$. Two partial-differential equations (one at $O(\epsilon^2)$ and one at $O(\epsilon^3)$) are used to determine A because it is a function of two time scales.

$\underline{O(\epsilon^2)}$

Substituting Equation (4.28) into Equation (4.22), we obtain

$$\begin{aligned} M_0\, D_0^2\boldsymbol{\eta}_2 + R_0\, \boldsymbol{\eta}_2 = &-2i\omega_1 D_1 A\, e^{i\omega_1 T_0} M_0\, \boldsymbol{p}_1 + 2i\omega_1 D_1 \bar{A}\, e^{-i\omega_1 T_0} M_0\, \boldsymbol{p}_1 \\ &+ \omega_1^2 A^2 e^{2i\omega_1 T_0} M_1(\boldsymbol{p}_1)\, \boldsymbol{p}_1 + \omega_1^2 \bar{A}^2 e^{-2i\omega_1 T_0} M_1(\boldsymbol{p}_1)\, \boldsymbol{p}_1 + 2\omega_1^2 A\bar{A} M_1(\boldsymbol{p}_1)\, \boldsymbol{p}_1 \\ &- A^2 e^{2i\omega_1 T_0} N_1(\boldsymbol{p}_1)\, \boldsymbol{p}_1 - \bar{A}^2 e^{-2i\omega_1 T_0} N_1(\boldsymbol{p}_1)\, \boldsymbol{p}_1 - 2A\bar{A} N_1(\boldsymbol{p}_1)\, \boldsymbol{p}_1 \\ &- A^2 e^{2i\omega_1 T_0} N_2(\boldsymbol{p}_1, \boldsymbol{p}_1)\, \boldsymbol{\eta}_0 - \bar{A}^2 e^{-2i\omega_1 T_0} N_2(\boldsymbol{p}_1, \boldsymbol{p}_1)\, \boldsymbol{\eta}_0 - 2A\bar{A} N_2(\boldsymbol{p}_1, \boldsymbol{p}_1)\, \boldsymbol{\eta}_0 \\ &+ A^2 e^{2i\omega_1 T_0} \boldsymbol{P}_2(\boldsymbol{p}_1, \boldsymbol{p}_1) + \bar{A}^2 e^{-2i\omega_1 T_0} \boldsymbol{P}_2(\boldsymbol{p}_1, \boldsymbol{p}_1) + 2A\bar{A} \boldsymbol{P}_2(\boldsymbol{p}_1, \boldsymbol{p}_1) \end{aligned} \tag{4.29}$$

We want to solve for $\boldsymbol{\eta}_2$, but we need to make sure that the solution is uniform. Therefore, we need to eliminate *secular terms* from $\boldsymbol{\eta}_2$. The terms that cause secular terms have frequencies identical to those of the left-hand homogeneous system, which are ω_1, ω_2, ... and ω_N. Because we have assumed no internal resonances, the only terms that lead to secular terms are the right-hand terms in Equation (4.29) associated with ω_1, containing $e^{i\omega_1 T_0}$ or $e^{-i\omega_1 T_0}$. Consequently, the terms that produce secular terms are proportional to the vector $-2i\omega_1 D_1 A\, M_0\, \boldsymbol{p}_1$ and its complex conjugate. A uniform solution for $\boldsymbol{\eta}_2$ only exists if the terms that produce secular terms are orthogonal to the conjugate $\bar{\boldsymbol{u}}_1$ of the nontrivial solution $\boldsymbol{u}_1$ of the adjoint homogeneous problem corresponding to ω_1; that is,

$$\omega_1^2 M_0^*\, \boldsymbol{u}_1 = R_0^*\, \boldsymbol{u}_1 \tag{4.30}$$

where a star superscript denotes the transpose of a matrix conjugate; that is, $X^* = \bar{X}^T$. Because all matrices are real, $X^* = X^T$ and the adjoint homogeneous problem corresponding to ω_1 is

$$\omega_1^2 M_0^T\, \boldsymbol{u}_1 = R_0^T\, \boldsymbol{u}_1 \tag{4.31}$$

For the terms that produce secular terms to be orthogonal to $\bar{\boldsymbol{u}}_1$ (that is, $\boldsymbol{u}_1$), the coefficient

of the vector $M_0\,\boldsymbol{p}_1$ must be zero; that is,

$$D_1 A = 0 \quad \Longrightarrow \quad A(T_1, T_2) = A(T_2) \tag{4.32}$$

Then, the $O(\epsilon^2)$ equation becomes

$$\begin{aligned} M_0\,D_0^2\boldsymbol{\eta}_2 + R_0\,\boldsymbol{\eta}_2 &= \omega_1^2 A^2 e^{2i\omega_1 T_0} M_1(\boldsymbol{p}_1)\,\boldsymbol{p}_1 + \omega_1^2 \bar{A}^2 e^{-2i\omega_1 T_0} M_1(\boldsymbol{p}_1)\,\boldsymbol{p}_1 \\ &\quad + 2\omega_1^2 A\bar{A} M_1(\boldsymbol{p}_1)\,\boldsymbol{p}_1 - A^2 e^{2i\omega_1 T_0} N_1(\boldsymbol{p}_1)\,\boldsymbol{p}_1 - \bar{A}^2 e^{-2i\omega_1 T_0} N_1(\boldsymbol{p}_1)\,\boldsymbol{p}_1 \\ &\quad - 2A\bar{A} N_1(\boldsymbol{p}_1)\,\boldsymbol{p}_1 - A^2 e^{2i\omega_1 T_0} N_2(\boldsymbol{p}_1, \boldsymbol{p}_1)\,\boldsymbol{\eta}_0 - \bar{A}^2 e^{-2i\omega_1 T_0} N_2(\boldsymbol{p}_1, \boldsymbol{p}_1)\,\boldsymbol{\eta}_0 \\ &\quad - 2A\bar{A} N_2(\boldsymbol{p}_1, \boldsymbol{p}_1)\,\boldsymbol{\eta}_0 + A^2 e^{2i\omega_1 T_0} \boldsymbol{P}_2(\boldsymbol{p}_1, \boldsymbol{p}_1) + \bar{A}^2 e^{-2i\omega_1 T_0} \boldsymbol{P}_2(\boldsymbol{p}_1, \boldsymbol{p}_1) \\ &\quad + 2A\bar{A}\boldsymbol{P}_2(\boldsymbol{p}_1, \boldsymbol{p}_1) \end{aligned} \tag{4.33}$$

The solution of Equation (4.33) consists of a homogeneous part and a particular part. We "lump" the homogeneous solution for $\boldsymbol{\eta}_2$ with the homogeneous solution for $\boldsymbol{\eta}_1$, since they are of the same form, which leaves us with the particular solution for $\boldsymbol{\eta}_2$; that is,

$$\boldsymbol{\eta}_2 = A^2 e^{2i\omega_1 T_0} \boldsymbol{z}_1 + \bar{A}^2 e^{-2i\omega_1 T_0} \boldsymbol{z}_1 + A\bar{A}\boldsymbol{z}_2 \tag{4.34}$$

where

$$\boldsymbol{z}_1 = [R_0 - 4\omega_1^2 M_0]^{-1}\{\omega_1^2 M_1(\boldsymbol{p}_1)\,\boldsymbol{p}_1 - N_1(\boldsymbol{p}_1)\,\boldsymbol{p}_1 - N_2(\boldsymbol{p}_1, \boldsymbol{p}_1)\,\boldsymbol{\eta}_0 + \boldsymbol{P}_2(\boldsymbol{p}_1, \boldsymbol{p}_1)\} \tag{4.35a}$$

$$\boldsymbol{z}_2 = 2\,R_0^{-1}\{\omega_1^2 M_1(\boldsymbol{p}_1)\,\boldsymbol{p}_1 - N_1(\boldsymbol{p}_1)\,\boldsymbol{p}_1 - N_2(\boldsymbol{p}_1, \boldsymbol{p}_1)\,\boldsymbol{\eta}_0 + \boldsymbol{P}_2(\boldsymbol{p}_1, \boldsymbol{p}_1)\} \tag{4.35b}$$

$\underline{O(\epsilon^3)}$

As with $\boldsymbol{\eta}_2$, a uniform solution for $\boldsymbol{\eta}_3$ only exists if the terms that produce secular terms of the $O(\epsilon^3)$ equation are orthogonal to the nontrivial solution $\boldsymbol{u}_1$ of the adjoint homogeneous equation (4.31). When we substitute our solutions for $\boldsymbol{\eta}_0$, $\boldsymbol{\eta}_1$, and $\boldsymbol{\eta}_1$ into the $O(\epsilon^3)$ equation, use Equation (4.32), collect terms proportional to $e^{i\omega_1 T_0}$, and make the vector sum be orthogonal to $\boldsymbol{u}_1$, we find that the *solvability condition* is

$$(\boldsymbol{u}_1 \cdot \boldsymbol{v}_1)\,A' + c\,(\boldsymbol{u}_1 \cdot \boldsymbol{v}_1)\,A + (\boldsymbol{u}_1 \cdot \boldsymbol{v}_2)\,A^2\bar{A} + (\chi_0\,\boldsymbol{u}_1 \cdot \boldsymbol{L})\,e^{i\sigma T_2}\chi_3 = 0 \tag{4.36}$$

where

$$\boldsymbol{v}_1 = -2i\omega_1 M_0\,\boldsymbol{p}_1 \tag{4.37a}$$

$$\begin{aligned}\boldsymbol{v}_2 = {}& \omega_1^2 M_1(\boldsymbol{z}_1)\,\boldsymbol{p}_1 + \omega_1^2 M_1(\boldsymbol{z}_2)\,\boldsymbol{p}_1 + 3\omega_1^2 M_2(\boldsymbol{p}_1,\boldsymbol{p}_1)\,\boldsymbol{p}_1 - N_1(\boldsymbol{z}_1)\,\boldsymbol{p}_1 \\ & - N_1(\boldsymbol{z}_2)\,\boldsymbol{p}_1 - 3N_2(\boldsymbol{p}_1,\boldsymbol{p}_1)\,\boldsymbol{p}_1 + 4\omega_1^2 M_1(\boldsymbol{p}_1)\,\boldsymbol{z}_1 - N_1(\boldsymbol{p}_1)\,\boldsymbol{z}_1 \\ & - N_1(\boldsymbol{p}_1)\,\boldsymbol{z}_2 - 2N_2(\boldsymbol{p}_1,\boldsymbol{z}_1)\,\boldsymbol{\eta}_0 - 2N_2(\boldsymbol{p}_1,\boldsymbol{z}_2)\,\boldsymbol{\eta}_0 - 3N_3(\boldsymbol{p}_1,\boldsymbol{p}_1,\boldsymbol{p}_1)\,\boldsymbol{\eta}_0 \\ & + 2\boldsymbol{P}_2(\boldsymbol{p}_1,\boldsymbol{z}_1) + 2\boldsymbol{P}_2(\boldsymbol{p}_1,\boldsymbol{z}_2) + 3\boldsymbol{P}_3(\boldsymbol{p}_1,\boldsymbol{p}_1,\boldsymbol{p}_1)\end{aligned} \tag{4.37b}$$

and the prime superscript denotes differentiation with respect to T_2, such that $A' = D_2 A$. Because the eigenvector $\boldsymbol{u}_1$ is known to within an arbitrary constant chosen at our disposal, we normalize $\boldsymbol{u}_1$ such that

$$\boldsymbol{u}_1 \cdot \boldsymbol{v}_1 = 1$$

and hence rewrite Equation (4.36) as

$$A' + cA + (\boldsymbol{u}_1 \cdot \boldsymbol{v}_2)\,A^2\bar{A} + (\chi_0\,\boldsymbol{u}_1 \cdot \boldsymbol{L})\,e^{i\sigma T_2}\chi_3 = 0 \tag{4.38}$$

Finally, we rearrange Equation (4.38) as

$$A' + cA - 4i\alpha_1 A^2\bar{A} + \frac{1}{2}i\alpha_2 e^{i\sigma T_2}\chi_3 = 0 \tag{4.39}$$

where α_1 and α_2 are real and defined as

$$\alpha_1 = \frac{1}{4} i\boldsymbol{u}_1 \cdot \boldsymbol{v}_2 \tag{4.40a}$$

$$\alpha_2 = -2i\,\chi_0\,\boldsymbol{u}_1 \cdot \boldsymbol{L} \tag{4.40b}$$

Equation (4.39) governs the temporal evolution of the complex quantity $A(T_2)$. At this point, we have solutions for $\boldsymbol{\eta}_0$, $\boldsymbol{\eta}_1$, and $\boldsymbol{\eta}_2$, where both $\boldsymbol{\eta}_1$ and $\boldsymbol{\eta}_2$ are functions of the unknown quantity $A(T_2)$. Once Equation (4.39) is solved for $A(T_2)$, a second-order (and large-time) approximate solution of $\boldsymbol{\eta}(t;\epsilon)$ is known according to Equation (4.10) as

$$\boldsymbol{\eta}(t;\epsilon) = \boldsymbol{\eta}_0 + \epsilon\boldsymbol{\eta}_1(T_0, T_2) + \epsilon^2\boldsymbol{\eta}_2(T_0, T_2) + \cdots \tag{4.41}$$

4.2.4 Modulation Equations

It is convenient to solve for $A(T_2)$ after converting the complex solvability condition (4.39) to two coupled real equations. To this end, we let

$$A(T_2) = \frac{1}{2}a(T_2)e^{i\theta(T_2)} \tag{4.42}$$

where $a(T_2)$ and $\theta(T_2)$ are real functions. The $O(\epsilon)$ solution $\boldsymbol{\eta}_1$ in Equation (4.28) and the $O(\epsilon^2)$ solution $\boldsymbol{\eta}_2$ in Equation (4.34) can then be expressed as

$$\boldsymbol{\eta}_1 = a(T_2)\cos(\omega_1 T_0 + \theta(T_2))\,\boldsymbol{p}_1 \tag{4.43}$$

and

$$\boldsymbol{\eta}_2 = \frac{1}{2}a^2(T_2)\Big(\cos(2\omega_1 T_0 + 2\theta(T_2))\,\boldsymbol{z}_1 + \frac{1}{2}\boldsymbol{z}_2\Big) \tag{4.44}$$

respectively. The functions $a(T_2)$ and $\theta(T_2)$ then represent the respective amplitude and phase of $\boldsymbol{\eta}_1$. Then, $\boldsymbol{\eta}(t;\epsilon)$ becomes

$$\begin{aligned}\boldsymbol{\eta}(t;\epsilon) = \;& \boldsymbol{\eta}_0 + \epsilon\, a(T_2)\cos\Big(\omega_1 T_0 + \theta(T_2)\Big)\,\boldsymbol{p}_1 \\ & + \frac{1}{2}\epsilon^2 a^2(T_2)\Big[\cos\Big(2\omega_1 T_0 + 2\theta(T_2)\Big)\,\boldsymbol{z}_1 + \frac{1}{2}\boldsymbol{z}_2\Big] + O(\epsilon^3)\end{aligned} \tag{4.45}$$

Now, because ϵ is a bookkeeping parameter, it is at our disposal and we are allowed to absorb ϵ into a by letting $\epsilon a \to a$, such that a is now a small quantity. In other words, we let ϵ equal one, with the understanding that a is small. With this choice, the solution $\boldsymbol{\eta}(t)$ becomes

$$\begin{aligned}\boldsymbol{\eta}(t) = \;& \boldsymbol{\eta}_0 + a(T_2)\cos\Big(\omega_1 T_0 + \theta(T_2)\Big)\,\boldsymbol{p}_1 \\ & + \frac{1}{2}a^2(T_2)\Big[\cos\Big(2\omega_1 T_0 + 2\theta(T_2)\Big)\,\boldsymbol{z}_1 + \frac{1}{2}\boldsymbol{z}_2\Big] + O(a^3)\end{aligned} \tag{4.46}$$

If a is sufficiently small and $\|\boldsymbol{p}_1\| = 1$, then the functions $a(T_2)$ and $\theta(T_2)$ represent the respective amplitude and phase of the fundamental response of the clamped circular plate.

Upon use of Equation (4.42), the solvability condition becomes

$$a' + ia\theta' + ca - i\alpha_1 a^3 + i\alpha_2 e^{i\sigma T_2 - i\theta}\chi_3 = 0 \tag{4.47}$$

For this complex-valued equation to hold, its real and imaginary parts must balance each other, respectively. The equation governing the amplitude $a(T_2)$ corresponds to the real part and the equation governing the phase $\theta(T_2)$ corresponds to the imaginary part; that is,

$$\text{Re(Eq.(4.47))}: \qquad a' = -ca + \alpha_2\chi_3 \sin(\sigma T_2 - \theta) \tag{4.48}$$

$$\text{Im(Eq.(4.47))}: \qquad \theta' = \alpha_1 a^2 - \frac{\alpha_2\chi_3 \cos(\sigma T_2 - \theta)}{a} \tag{4.49}$$

for nonzero amplitude $a(T_2)$.

These *modulation equations* are nonautonomous because they depend explicitly on the time scale T_2. To determine an autonomous set of modulation equations, we let

$$\gamma(T_2) = \theta(T_2) - \sigma T_2 \tag{4.50}$$

and transform Equations (4.48) and (4.49) into

$$a' = -ca - \alpha_2\chi_3 \sin(\gamma) \tag{4.51}$$

$$\gamma' = \alpha_1 a^2 - \sigma - \frac{\alpha_2\chi_3 \cos(\gamma)}{a} \tag{4.52}$$

respectively.

4.3 Frequency-Response (F-R) Equation

The equations governing the equilibrium values a_{eq} and γ_{eq} are found by setting $a' = 0$ and $\gamma' = 0$ in the modulation equations. Thus, at the (dynamic) equilibrium of the primary resonance excitation of the first mode,

$$0 = -ca - \alpha_2\chi_3 \sin(\gamma) \tag{4.53a}$$

$$0 = \alpha_1 a^2 - \sigma - \frac{\alpha_2\chi_3 \cos(\gamma)}{a} \tag{4.53b}$$

These coupled equations can be used to find how the amplitude a varies with frequency through the detuning parameter σ. By using the fact that $\sin(\gamma_{eq})^2 + \cos(\gamma_{eq})^2 = 1$, we combine the equilibrium equations and obtain

$$a_{eq}^2\left\{c^2 + (\sigma - \alpha_1 a_{eq}^2)^2\right\} = \alpha_2^2\chi_3^2 \tag{4.54}$$

which is called the *frequency-response* (*F-R*) *equation*. The curve that satisfies the F-R equation is called the *frequency-response curve* and a point on it is stable if all of the eigenvalues of the Jacobian matrix of Equations (4.51) and (4.52) evaluated at that point are in the left-half side of the complex plane. It follows from Equations (4.51) and (4.52) that the Jacobian matrix J at an F-R point is

$$J = \left[\begin{array}{cc} \frac{\partial a'}{\partial a} & \frac{\partial a'}{\partial \gamma} \\ \frac{\partial \gamma'}{\partial a} & \frac{\partial \gamma'}{\partial \gamma} \end{array} \right] \Bigg|_{F-R} = \left[\begin{array}{cc} -c & a_{eq}(\sigma - \alpha_1 a_{eq}^2) \\ 2\alpha_1 a_{eq} + \frac{\alpha_1 a_{eq}^2 - \sigma}{a_{eq}} & -c \end{array} \right] \tag{4.55}$$

The eigenvalues λ_1 and λ_2 of J are then

$$\lambda_1, \lambda_2 = -c \pm \sqrt{-(\sigma - \alpha_1 a_{eq}^2)(\sigma - 3\alpha_1 a_{eq}^2)} \tag{4.56}$$

If $\mathrm{Re}(\lambda_1) < 0$ and $\mathrm{Re}(\lambda_2) < 0$ for a given equilibrium point (σ, a_{eq}) on the F-R curve, then the point is stable. If $\mathrm{Re}(\lambda_1) > 0$ and/or $\mathrm{Re}(\lambda_2) > 0$, then the point is unstable.

4.3.1 Nonlinear Resonance

The nonlinear resonance frequency occurs at the peak of the F-R curve, which is where the equilibrium amplitude a_{eq} is a maximum in the $\sigma - a_{eq}$ plane. Inspection of the frequency-response equation (4.54) reveals that a_{eq} is maximized when

$$\sigma - \alpha_1 a_{eq}^2 = 0 \tag{4.57}$$

The F-R equation then reduces to $c^2 a_{eq}^2 = \alpha_2^2 \chi_3^2$, which means that the nonlinear resonance amplitude a_{nr} is

$$a_{nr} = \frac{|\alpha_2|\, \chi_3}{c} \tag{4.58}$$

for positive c and χ_3. The value of σ for nonlinear resonance is then

$$\sigma = \alpha_1 a_{nr}^2 = \frac{\alpha_1 \alpha_2^2 \chi_3^2}{c^2} \tag{4.59}$$

according to Equation (4.57). Therefore, the nonlinear resonance frequency ω_{nr} is

$$\omega_{nr} = \omega_1 + \alpha_1 a_{nr}^2 = \omega_1 + \frac{\alpha_1 \alpha_2^2 \chi_3^2}{c^2} \tag{4.60}$$

according to our definition of ω_f in Equation (4.9) with ϵ being set equal to one.

In summary, when only the first mode is excited by a primary resonance excitation, the clamped circular plate resonates nonlinearly at the frequency ω_{nr} with a first-order amplitude a_{nr}, according to the solution for $\boldsymbol{\eta}(t)$ in Equation (4.46). We also note that a_{nr} must be sufficiently small in order for terms of $O(a^3)$ and higher to be neglected in the solution.

4.3.2 Inflection Point

For sufficiently small forcing χ_3, the amplitude a_{eq} is a single-valued function of the detuning parameter σ. The F-R curve has a "camel's hump" with a peak occuring at the nonlinear resonance point. However, as the forcing parameter χ_3 increases, the camel's hump bends either to the left (softening) or to the right (hardening). At a critical value χ_3^{cr}, the camel's hump loses its single-valuedness (one a_{eq} for one σ) for $\chi_3 < \chi_3^{cr}$ and is multi-valued (three a_{eq} for one σ) for certain σ when $\chi_3 > \chi_3^{cr}$. Therefore, an *inflection point* exists on the F-R curve when $\chi_3 = \chi_3^{cr}$, being the transition point between single- and multi-valuedness. In this section, we seek expressions for the inflection point in the $\sigma - a_{eq}$ plane and the critical χ_3 that causes the inflection point.

We begin seeking the inflection point by using the F-R equation (4.54) to create a function $f(a)$ as

$$f(a) = a^2\left\{c^2 + (\alpha_1 a^2 + \sigma)^2\right\} - \alpha_2^2\chi_3^2 \tag{4.61}$$

According to the F-R equation, $f(a_{eq}) = 0$. Now, because the F-R curve is on the verge of multi-valuedness at the inflection point, $f(a)$ must have a triple root there, such that the one root for $\chi_3 < \chi_3^{cr}$ bifurcates into three roots for $\chi_3 > \chi_3^{cr}$. For the triple root to exist at the inflection point, the first and second derivatives of $f(a)$ must be zero when $a = a_{eq}$; that is, $f'(a_{eq}) = f''(a_{eq}) = 0$.

The three equations ($f(a_{eq}) = 0$, $f'(a_{eq}) = 0$, and $f''(a_{eq}) = 0$) can be solved for the three unknowns (a_{eq}, σ, and χ_3) at the inflection point. Specifically, the two derivative equations ($f'(a_{eq}) = 0$ and $f''(a_{eq}) = 0$) can be solved for a_{eq} and σ at the inflection point, and then these values can be substituted into the third equation ($f(a_{eq}) = 0$) to yield the critical χ_3. Using the `Solve` command in *Mathematica*, we solve $f'(a_{eq}) = 0$ and $f''(a_{eq}) = 0$

for positive a_{eq} and real σ to find the inflection point at

$$(\sigma,\, a_{eq}) = \left(\sqrt{3}\, c\, \mathrm{sgn}(\alpha_1),\ \frac{\sqrt{2\, c}}{\sqrt[4]{3\, \alpha_1^2}}\right) \tag{4.62}$$

where $\mathrm{sgn}(x)$ gives the sign of a real, nonzero number x. After substitution of the inflection point into $f(a_{eq}) = 0$, the critical χ_3 is found to satisfy

$$\chi_3^2 = \frac{8\, c^3}{3\sqrt{3}\, |\alpha_1|\, \alpha_2^2} \tag{4.63}$$

Thus, an inflection occurs at the point in Equation (4.62) when Equation (4.63) is satisfied.

4.3.3 Softening or Hardening

A simple way to determine whether the F-R curve bends to the left (softening) or to the right (hardening) is to determine how the F-R curve behaves locally around the inflection point (4.62). Because $f(a)$ has a triple root at the inflection point, σ is locally a cubic function of a_{eq} with no linear and quadratic terms; that is, $\sigma'(a_{eq}) = 0$ and $\sigma''(a_{eq}) = 0$. Consequently, to determine whether the effective nonlinearity of the plate is softening or hardening, we inspect the triple derivative $\sigma^{(3)}(a_{eq})$ at the inflection point; that is,

$$\sigma^{(3)}(a_{eq}) > 0 \implies \text{softening} \quad \text{and} \quad \sigma^{(3)}(a_{eq}) < 0 \implies \text{hardening}$$

Therefore, we need to determine the sign of σ to know whether the nonlinearity is softening or hardening.

To determine $\sigma^{(3)}(a_{eq})$ at the inflection point, we operate on the F-R equation (4.54) with $\frac{d^3}{da_{eq}^3}$, where σ is taken to be an implicit function of a_{eq}. Then, we use the fact that $\sigma'(a_{eq}) = \sigma''(a_{eq}) = 0$ to reduce the problem into a single equation in the single unknown $\sigma^{(3)}(a_{eq})$ at the inflection point (4.62) whose solution is

$$\sigma^{(3)}(a_{eq}) = -\frac{24\sqrt{2}\, \sqrt[4]{3\, \alpha_1^2}\, \alpha_1}{\sqrt{c}} \tag{4.64}$$

at the inflection point. Consequently, the sign of $\sigma^{(3)}(a_{eq})$ only depends on α_1 as

$$\alpha_1 < 0 \implies \text{softening} \quad \text{and} \quad \alpha_1 > 0 \implies \text{hardening} \tag{4.65}$$

4.3.4 Saddle-Node Bifurcations

As χ_3 increases beyond the critical value satisfying Equation (4.63), the F-R curve becomes multi-valued, with two saddle-node bifurcations instead of an inflection point. The saddle-node bifurcations satisfy the F-R equation (4.54) and $\sigma'(a_{eq}) = 0$. To use the latter equation, we differentiate Equation (4.54) with respect to a_{eq}, where σ is taken to be an implicit function of a_{eq}, set $\sigma'(a_{eq}) = 0$, and obtain the other equation that the saddle-node bifurcations satisfy:

$$2\left\{c^2 + (\sigma - \alpha_1 a_{eq}^2)^2\right\} - 4\alpha_1 a_{eq}^2(\sigma - \alpha_1 a_{eq}^2) = 0 \tag{4.66}$$

for nonzero a_{eq}. Later, we will solve the F-R equation (4.54) and the additional equation (4.66) numerically to find the values of a_{eq} and σ at the saddle-node bifurcations for various system parameters.

Chapter 5

Nonlinear Resonance Results

5.1 Numerical Results

In this chapter, we investigate the primary resonance excitation of the first mode of the clamped CMUT plate. By using the frequency-response equation (4.54), we can plot the equilibrium vibration amplitude a_{eq} versus the forcing frequency ω_f; that is, we can create F-R curves for general system parameters. The nonlinear resonance frequency ω_{nr} and amplitude a_{nr} and possible saddle-node bifurcations are known according to equations presented in the previous chapter. Furthermore, the softening or hardening type of the effective nonlinearity due to the DC voltage χ_0 is determined according to the conditions (4.65), and the critical AC voltage amplitude χ_3^{cr} for the onset of multi-valuedness is known according to Equation (4.63).

5.1.1 Frequency-Response Curves

We begin by choosing system parameters and plotting F-R curves for various amplitudes χ_3 of the AC voltage. Figure 5.1 contains representative plots of the equilibrium vibration amplitude a_{eq} (a, for short) versus forcing frequency ω_f. For any given system, a critical χ_3^{cr} exists, such that the F-R curve is single-valued for $\chi_3 < \chi_3^{cr}$, as in Figure 5.1(a). The response is purely stable, being represented by a solid curve, and the nonlinear resonance point is located by a circle. At the critical value χ_3^{cr}, the single-valuedness is about to break down, as in Figure 5.1(b). An inflection point exists, denoted by the dot. For $\chi_3 > \chi_3^{cr}$, the curve is

partially multi-valued, as seen in Figure 5.1(c). Two saddle-node bifurcations, also denoted by dots, now exist and the curve between them is unstable (dashed). Accordingly, hysteresis exists associated with jumps at the saddle-node bifurcations as the forcing frequency ω_f is slowly varied. As one follows the F-R curve by slowly increasing/decreasing the forcing frequency ω_f, the vibration amplitude a will jump down/up at a saddle-node bifurcation. The rapid changes in amplitude due to small changes in forcing frequency are indicated by the dashed arrows in Figure 5.1(c).

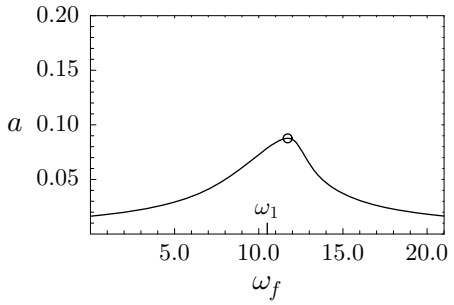

(a) Single-valued response ($\chi_3 < \chi_3^{cr}$)

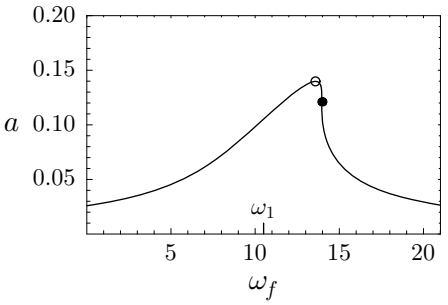

(b) Response with inflection point ($\chi_3 = \chi_3^{cr}$)

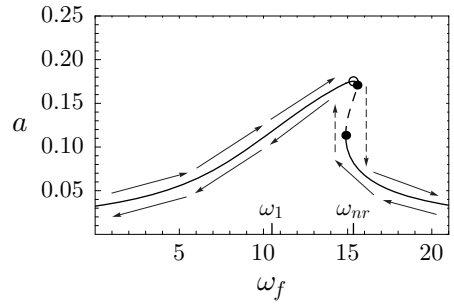

(c) Multi-valued response ($\chi_3 > \chi_3^{cr}$)

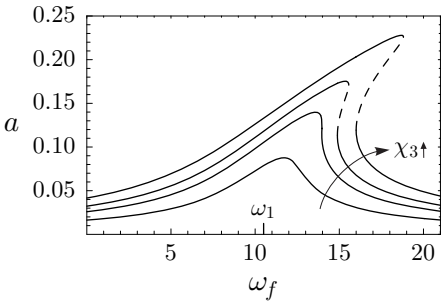

(d) Responses for various χ_3

Figure 5.1: F-R curves for $\beta = 100$, $\nu = 0.1$, $\tau = 1$, $F(r,t) = 0$, $\chi_0^2 = 0.5$, $c = 2$, and (a) $\chi_3 = 5$, (b) $\chi_3 = \chi_3^{cr} = 7.98$, (c) $\chi_3 = 10$, and (d) various values of χ_3.

The evolution of the vibration amplitude with increasing χ_3 can be seen in Figure 5.1(d). As the AC forcing amplitude χ_3 increases for the given system, a increases and the F-R curve bends to the right (hardening). Eventually, the F-R curve becomes multi-valued accompanied with hysteresis. We note that due to the conditions (4.65), the effective nonlinearity $\alpha_1 = 157.5 > 0$ and hence the system behavior is of is of the hardening type. The nonlinear

resonance frequency ω_{nr} is then always greater than the first natural undamped frequency ω_1, according to Equation (4.60), as seen in Figure 5.1(c).

Because α_1 is independent of χ_3, the nonlinearity type (softening/hardening) is independent of χ_3. The softening and hardening type only depends on the voltage through the DC component χ_0, which affects the equilibrium. Consequently, as we increase χ_0 and the plate deflects more towards the fixed electrode, the plate's nonlinear behavior, like that in Figure 5.1, becomes less hardening and eventually becomes softening. In fact, for the clamped circular plate with electrostatic actuation, the system behavior does transition from hardening to softening as χ_0 increases. For example, Figure 5.2 contains representative plots of a versus ω_f for a system with softening behavior. The chosen system parameters are the same as those for Figure 5.1, except that $\chi_0^2 = 25$, which is greater than $\chi_0^2 = 0.5$ for Figure 5.1.

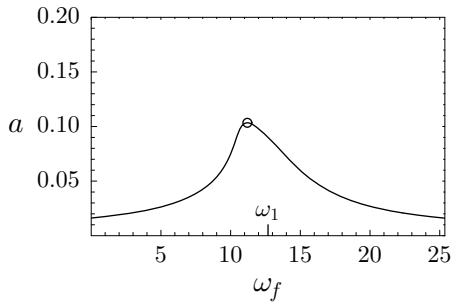

(a) Single-valued response ($\chi_3 < \chi_3^{cr}$)

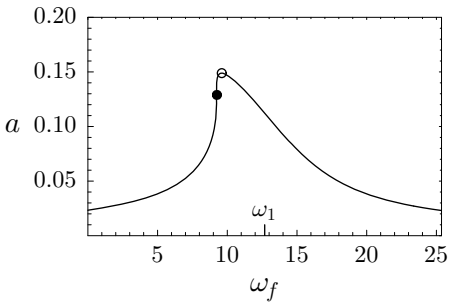

(b) Response with inflection point ($\chi_3 = \chi_3^{cr}$)

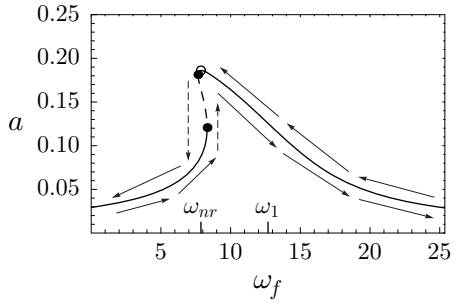

(c) Multi-valued response ($\chi_3 > \chi_3^{cr}$)

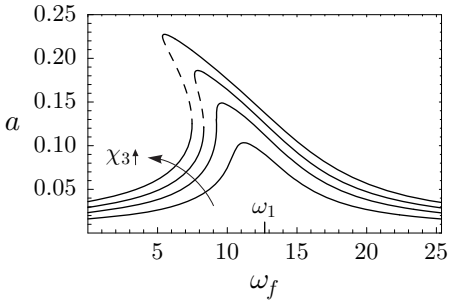

(d) Responses for various χ_3

Figure 5.2: F-R curves for $\beta = 100$, $\nu = 0.1$, $\tau = 1$, $F(r,t) = 0$, $\chi_0^2 = 25$, $c = 2$, and (a) $\chi_3 = 0.5$, (b) $\chi_3 = \chi_3^{cr} = 0.720$, (c) $\chi_3 = 0.9$, and (d) various values of χ_3.

Characteristics similar to those in Figure 5.2 are exhibited in Figure 5.1 for increasing

χ_3, except that the nonlinear behavior is softening rather than hardening. Once again, as the forcing amplitude χ_3 increases, the F-R curve eventually becomes multi-valued accompanied with hysteresis and jumps, as seen in Figure 5.2(d). In this case, the nonlinearity type is softening instead of hardening because $\alpha_1 = -138.9$, which is now negative. The nonlinear resonance frequency ω_{nr} is then always smaller than the frequency ω_1 according to Equation (4.60), as seen in Figure 5.2(c). Consequently, as one follows the F-R curve by slowly increasing/decreasing the forcing frequency ω_f, the amplitude a will jump up/down at a saddle-node bifurcation.

5.1.2 Force-Response Curves

Jumps in the response amplitude may also be seen in a *force-response* (*Force-R*) *curve*, which depicts how the vibration amplitude a changes with the amplitude χ_3 of the AC forcing for a fixed forcing frequency ω_f, or alternatively, a fixed detuning parameter σ. Representative Force-R curves are shown in Figures 5.3(b) and 5.3(d) for the systems of 5.3(a) and 5.3(c), respectively. Jumps (depicted as arrows) occur in Figure 5.3(b) because σ is greater than the critical value for the inflection point (4.62) of the *hardening-type* system, and amplitude jumps occur in Figure 5.3(d) because σ is less than the critical inflection point value of the *softening-type* system. Conversely, if the chosen forcing frequency ω_f does not deviate far enough from the natural frequency ω_1 for either system type, then no jumps in the vibration amplitude will occur.

5.1.3 Transition from Hardening- to Softening-Type Nonlinearity

As we increase the DC voltage χ_0, the clamped CMUT plate transitions from a hardening-type to a softening-type system. For example, this transition is seen in the *backbone* (bold) curve in Figure 5.4. The backbone curve tracks the nonlinear resonance frequency from its position for zero χ_0 (denoted with a circle) up to pull-in (not seen in the figure). Initially, we only have hardening-type systems ($\alpha_1 > 0$), with the tracked nonlinear resonance point heading north-east. However, at the *turnaround point* (denoted by a dot), the nonlinear resonance point begins to head north-west. As we increase χ_0 to 3.36 (denoted by an asterisk), we find that there is neither hardening nor softening behavior because $\alpha_1 = 0$. Hence, the system

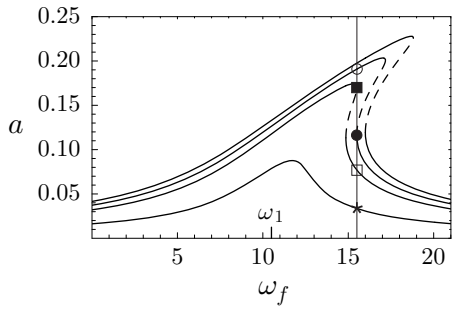

(a) F-R curves for $\chi_0^2 = 0.5$

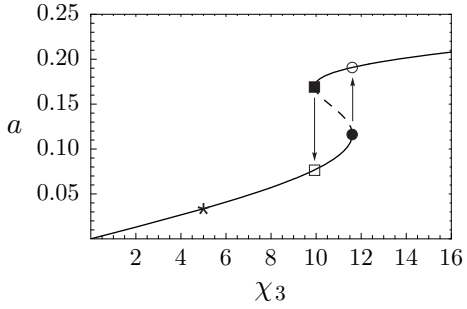

(b) Force-R curve for $\chi_0^2 = 0.5$ and $\sigma = 5$

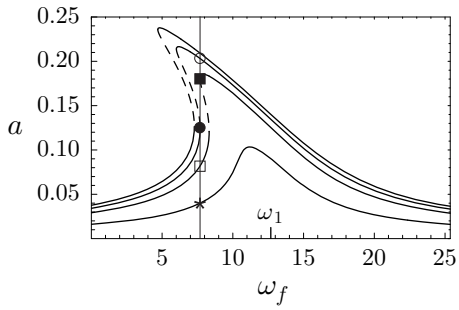

(c) F-R curves for $\chi_0^2 = 25$

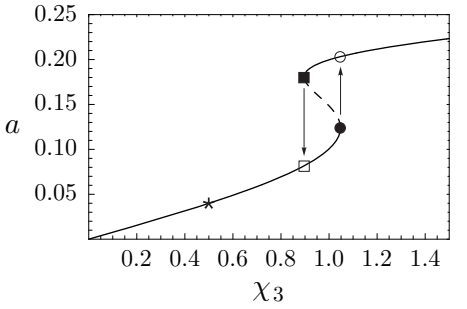

(d) Force-R curve for $\chi_0^2 = 25$ and $\sigma = -5$

Figure 5.3: Frequency-response and force-response curves for the system with $\beta = 100$, $\nu = 0.1$, $\tau = 1$, $F(r,t) = 0$, $c = 2$, and either (a)-(b) $\chi_0^2 = 0.5$ or (c)-(d) $\chi_0^2 = 25$.

is locally linear and the F-R curve is not bent for that case. However, as we increase the DC voltage χ_0 beyond 3.36, we find that the nonlinearity of the system becomes softening ($\alpha_1 < 0$), with the F-R curve being bent to the left, like that for $\chi_0 = 3.61$. Softening remains until pull-in is reached.

The same transition from hardening to softening behavior is also exhibited in Figure 5.5. The frequency ratio ω_{nr}/ω_1 is plotted versus the DC forcing χ_0 in Figure 5.5(a). For zero χ_0, the frequency ratio ω_{nr}/ω_1 is always equal to one because $\alpha_2 = 0$ when $\chi_0 = 0$ according to Equation (4.40b), which means that $\omega_{nr} = \omega_1$ according to Equation (4.60). Then, ω_{nr}/ω_1 increases as χ_0 increases because the system is of the hardening type (i.e., α_1 is initially positive), as seen in Figure 5.5(b). However, this trend ends when the maximum of ω_{nr}/ω_1 is reached (denoted by a vertical dash). The frequency ratio begins to head back to one, and as χ_0 increases beyond 3.36, the nonlinearity type becomes softening and ω_{nr}/ω_1 decreases

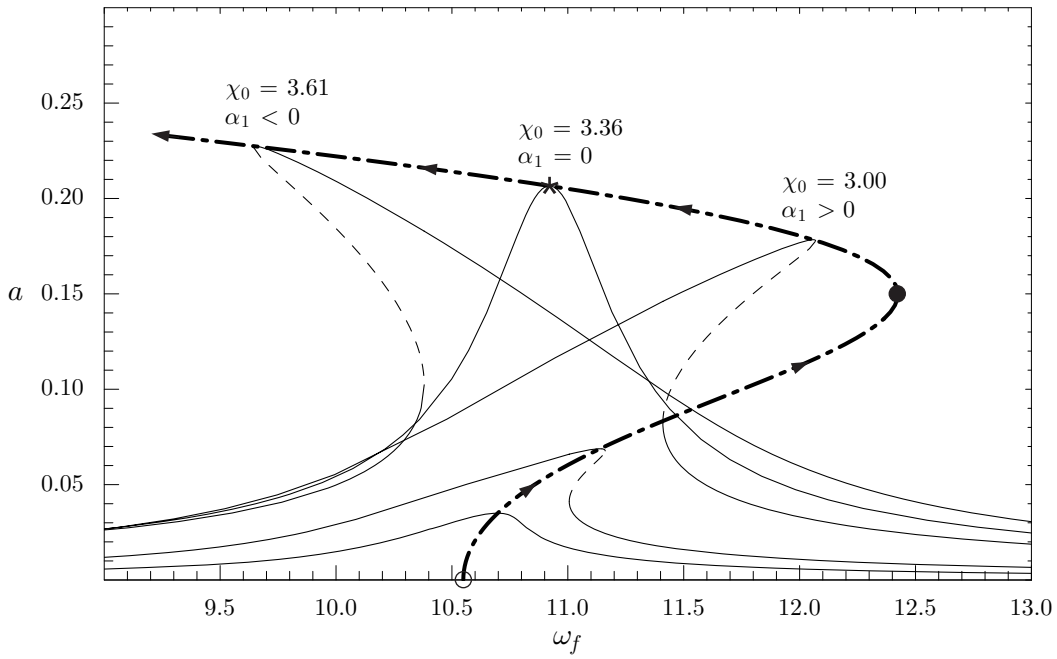

Figure 5.4: Progression from hardening to softening behavior as χ_0 increases for $\beta = 100$, $\nu = 0.1$, $\tau = 1$, $F(r,t) = 0$, $c = 0.25$, and $\chi_3 = 0.25$.

below one, or alternatively, $\alpha_1 < 0$, as seen in Figure 5.5(b). We note that the circle, dot, and asterisk of Figure 5.5(a) are analogous to those on the backbone curve in Figure 5.4. Furthermore, we note that the turnaround point does not generally occur at the maximum of ω_{nr}/ω_1, as in Figure 5.5(a).

The DC voltage χ_0 at the transition point ($\alpha_1 = 0$) from a hardening-type to a softening-type system depends on the parameters. The dependence on β for $\nu = 0.1$, $\tau = 1$, and $F(r,t) = 0$ is seen in Figure 5.6. For example, when $\beta = 100$, the system being studied is that of Figure 5.5. The system behavior changes from hardening to softening as χ_0 is increased. Eventually, the plate is pulled into the "brick wall" (the bottom electrode). In fact, $\alpha_1 \to -\infty$ and $\alpha_2 \to \infty$ as the pull-in limit is approached, which means that the nonlinear resonance amplitude and frequency become increasingly sensitive to the amplitude χ_3 of the AC forcing according to Equations (4.58) and (4.60), respectively. Consequently, χ_3 must approach zero to maintain finite responses as the plate approaches pull-in.

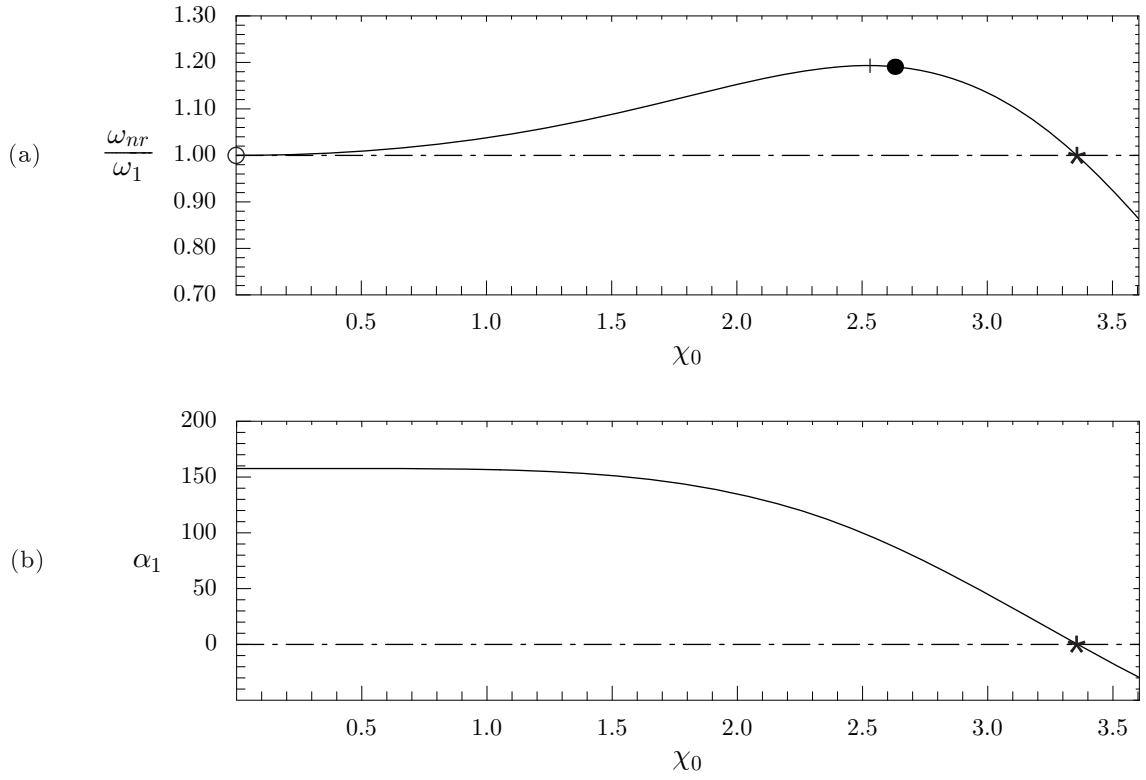

Figure 5.5: (a) Change in ω_{nr}/ω_1 from being greater than one (hardening) to being less than one (softening) and (b) change in α_1 from positive (hardening) to negative (softening) as χ_0 increases for $\beta = 100$, $\nu = 0.1$, $\tau = 1$, $F(r,t) = 0$, $c = 0.25$, and $\chi_3 = 0.25$.

5.2 Numerical Convergence

Thus far, we have found that stable deflections converge sufficiently with five axisymmetric modes. However, in order for the reduced-order model to be of any use, the equilibrium amplitude a also has to converge as the number N of modes increases. This means that the system parameters α_1 and α_2 in Equation (4.54) and the first undamped natural frequency ω_1 must all be sufficiently close to their limits so that the F-R curve is sufficiently converged.

5.2.1 Zero Pressure Difference

We calculated α_1, α_2, and ω_1 as functions of χ_0 for various combinations of system parameters with different values of N. Because the reduced-order model is intended for analysis of

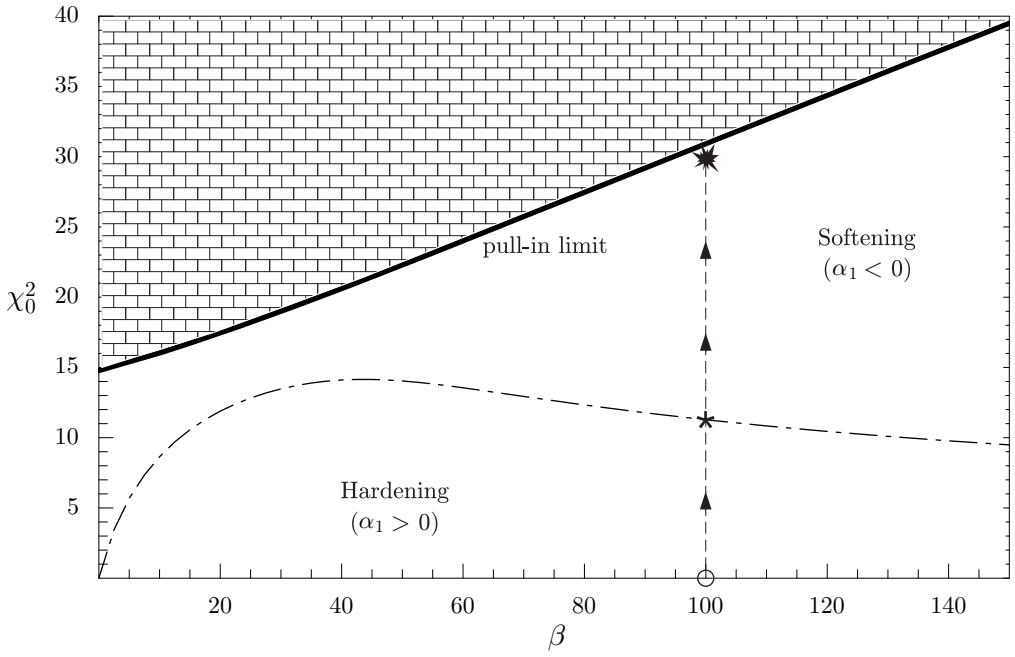

Figure 5.6: Hardening and softening regions for $\nu = 0.1$, $\tau = 1$, and $F(r,t) = 0$.

CMUTs, we choose (nondimensional) system parameters feasible for typical CMUTs. We focus on modeling air transducers by restricting the nondimensional residual stress τ to be less than the nondimensional parameter β, where β is as high as 100. For simplicity, we also let Poisson's ratio ν equal to 0.2 and let $F(r,t) = 0$ (no pressure difference across the plate).

Results for a combination of parameters are shown in Figure 5.7. As pull-in is approached, the respective curves in Figures 5.7(a)-(c) generally deviate from each other. However, three modes seem to be sufficient to characterize the dynamic-related quantities α_1, α_2, and ω_1 for most of the range of χ_0 up to pull-in. In fact, the curves for three and four modes are hardly distinguishable. At $\chi_0^2 = 13$, which is about 87% of the critical value for pull-in, the frequency-response curves in Figure 5.7(d) are basically converged for three modes.

However, when the geometric nonlinearity increases by increasing β from 1 (in Figure 5.7) to 100 (in Figure 5.8), at least four modes may be needed to sufficiently characterize the steady-state dynamics for most of the range up to pull-in. The curves in Figure 5.8 for four and fives modes are barely distinguishable, and at $\chi_0^2 = 28$, which is about 84% of the critical value for pull-in, the F-R curves in Figure 5.8(d) are basically converged for four modes.

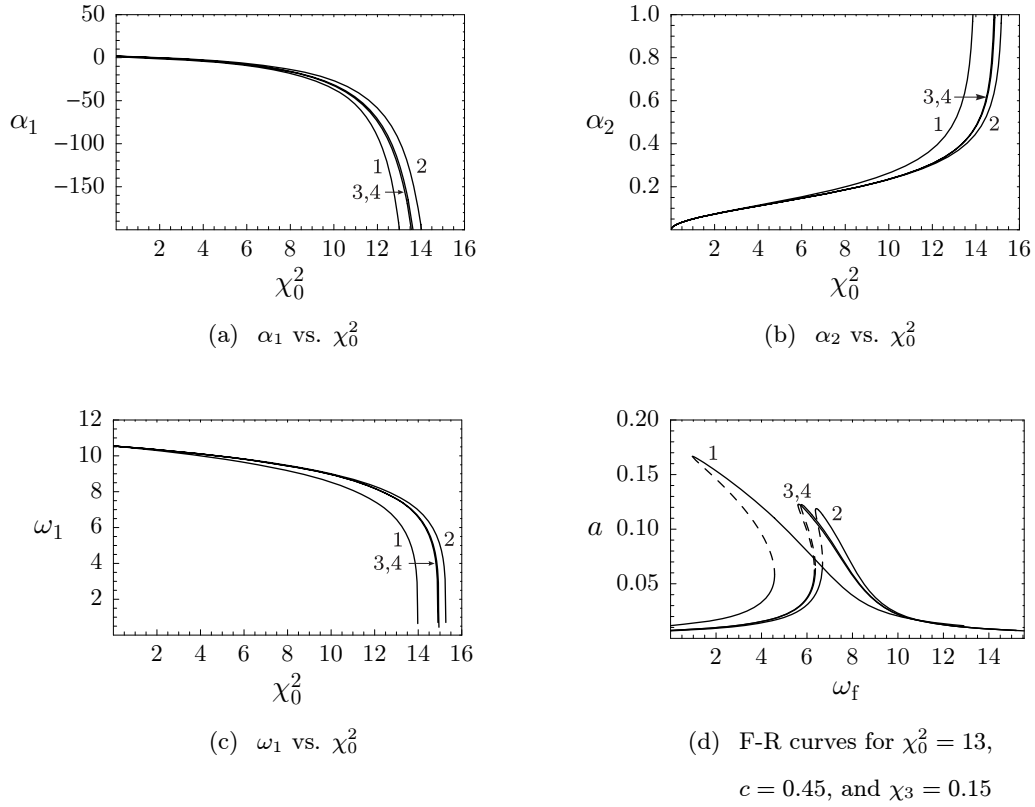

(a) α_1 vs. χ_0^2

(b) α_2 vs. χ_0^2

(c) ω_1 vs. χ_0^2

(d) F-R curves for $\chi_0^2 = 13$, $c = 0.45$, and $\chi_3 = 0.15$

Figure 5.7: Parameter and response curves for $\beta = 1$, $\nu = 0.2$, $\tau = 1$, and $F(r,t) = 0$ obtained with different number of modes.

5.2.2 Positive Pressure Difference

The previous analysis was for systems with zero pressure difference across the plate, but advantageous pressure differences exist in many CMUTs. For instance, when a vacuum is created under the plate and the pressure from a fluid acts on its top, the electromechanical coupling increases due to the plate deflection, making the system more efficient for conversion of electrical energy to mechanical energy (Huang et al., 2003a). We would like the macro-model to be applicable for such situations. In this spirit, we let $F(r,t)$ be constant and test convergence for feasible cases, one of which is seen in Figure 5.9. For all four values of F, four modes are sufficient for convergence for most of the range up to the respective pull-in. However, as F increases, the curves deviate more and five modes become necessary for convergence.

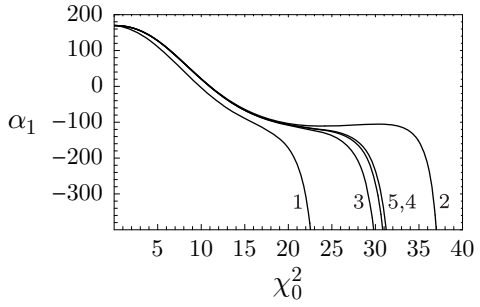

(a) α_1 vs. χ_0^2

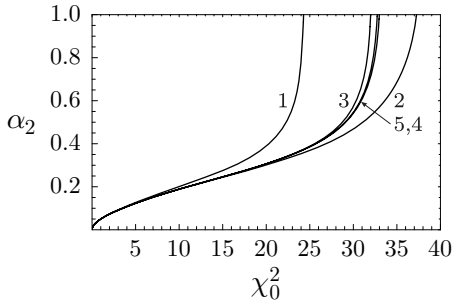

(b) α_2 vs. χ_0^2

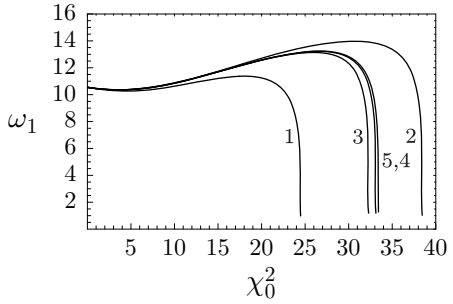

(c) ω_1 vs. χ_0^2

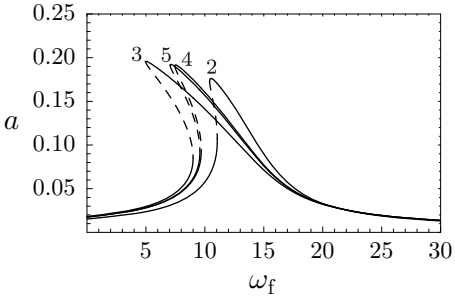

(d) F-R curves for $\chi_0^2 = 28$, $c = 1.2$, and $\chi_3 = 0.5$

Figure 5.8: Parameter and response curves for $\beta = 100$, $\nu = 0.2$, $\tau = 1$, and $F(r,t) = 0$ obtained with different number of modes.

In general, at least three ($N = 3$) modes should be used in the reduced-order model (3.21) to characterize the responses of clamped circular plates used in air-immersed CMUTs to primary resonance excitations. In fact, three modes were used to generate the curves in Figures 5.1-5.6. Consequently, the error in the approximate equilibrium solution (4.46) is mainly due to truncation at a certain order of a in the method of multiple scales, instead of being due to the truncation of the number N of modes in the reduced-order model. In practice, however, the nondimensional amplitude a will be sufficiently small, such that the number N of modes primarily limits the accuracy of the approximate amplitudes.

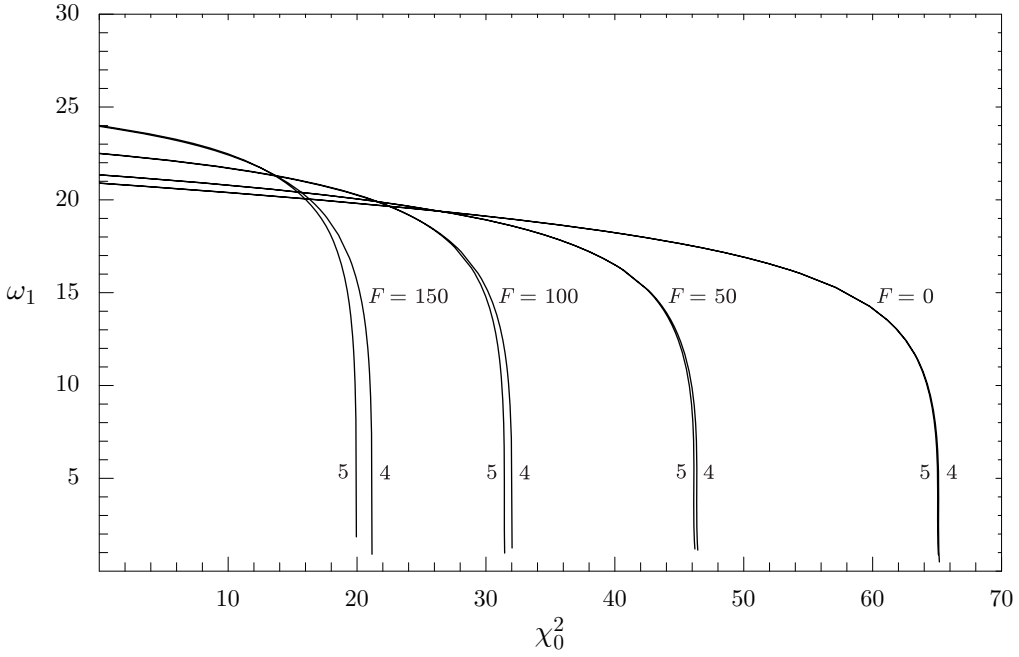

Figure 5.9: First undamped natural frequency for $\beta = 50$, $\nu = 0.2$, $\tau = 50$, and (for paired curves from left to right) $F(r,t) = 150$, $F(r,t) = 100$, $F(r,t) = 50$, or $F(r,t) = 0$ obtained with four and five modes.

5.3 Design Curves for Zero Pressure Difference

Thus far, we have examined the behavior of the primary resonance excitation for the system with $\beta = 100$, $\nu = 0.1$, $\tau = 1$, and $F(r,t) = 0$. For example, as the DC forcing χ_0 increases from zero, the system transitions from a hardening-type ($\alpha_1 > 0$) to a softening-type ($\alpha_1 < 0$) system up to pull-in. However, for design purposes, it might be instructive to know when the system is of the hardening- or the softening-type for any system parameters for the common case of zero pressure difference ($F(r,t) = 0$) across the plate.

First, we determine how the curve $\alpha_1 = 0$ in Figure 5.6 changes as the residual stress τ varies. Figure 5.10(a) shows *transition curves* from hardening-to-softening behavior for various values of τ. These curves resemble the curve shown in Figure 5.6. Clearly, the transition value X_0^{tr} increases/decreases as τ increases/decreases. This trend makes sense because the pull-in values X_0^{pi} also increase with τ. In fact, an approximate scaling seems to exist among the transition curves. The maxima of the curves are denoted by dots and seem to fall approx-

imately on a straight line, as evidenced by the dashed curve in the Figure 5.10(a). Because both of the pull-in and transition values increase with τ, we scale the transition values with respect to the pull-in values for all curves in order to visualize any possible scalings. These scaled transition curves are seen in Figure 5.10(b). The maximum of X_0^{tr}/X_0^{pi} is about 71.0% for most curves, even though this maximum occurs for different values of β. Again, it appears that an approximate scaling exists somehow.

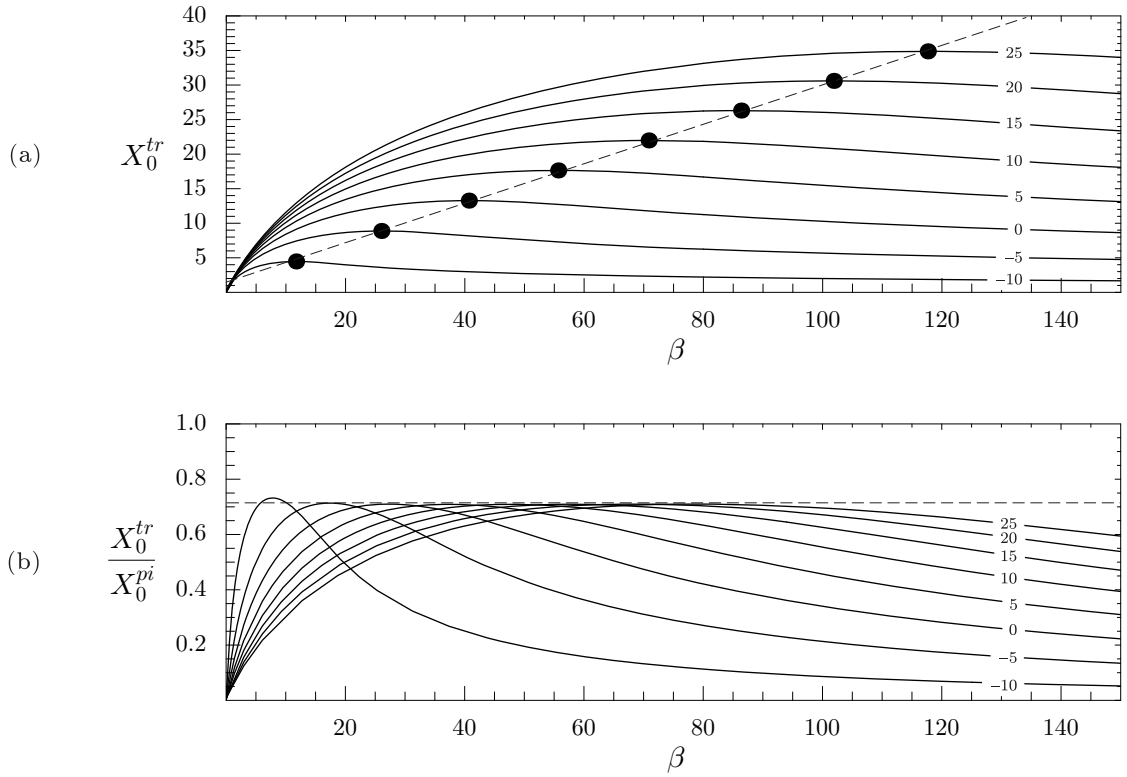

Figure 5.10: (a) Transition curves ($\alpha_1 = 0$) and (b) scaled transition curves for $\nu = 0.1$ and various values of τ.

Because of the apparent scaling, an attempt was made to relate the hardening-to-softening transition curves for non-zero τ to the transition curve for zero τ. We attempted to find equations that would enable one to approximate a transition curve for non-zero τ by using the transition curve for zero τ. Inspired by the dashed line in Figure 5.10(a), we let

$$\beta = \left(1 + \frac{\tau}{\delta_1}\right)\beta|_{\tau=0} \quad \text{and} \quad X_0^{tr} = \left(1 + \frac{\tau}{\delta_2}\right)X_0^{tr}|_{\tau=0}, \tag{5.1}$$

where $(\beta|_{\tau=0},\ X_0^{tr}|_{\tau=0})$ is any point on the transition curve for zero τ and δ_1 and δ_2 are constants yet to be determined. A transition curve for general stress τ can by drawn by using these linear expansion rules once the transition curve for zero τ is known. We note that both the transition curve for zero τ and every δ_i are functions of ν.

The constants δ_1 and δ_2 were determined first for $\nu = 0.1$ through use of a least-squares fit between predictions from the mapping in Equations (5.1) and actual transition curve values for $\tau = 10,\ 20,\ 30,\ 40$, and 50. Positive τ values were used because the residual stresses in MEMS (hundreds of MPas) can be precisely controlled (Ladabaum et al., 1998) and are usually tensile. Many data points on the zero-τ transition curve were chosen and used in Equations (5.1) to predict points on the non-zero τ curves for fitting purposes. The sum of the squares of errors between predicted and actual X_0^{tr} values on the non-zero τ curves was then minimized. A local minimum is found at

$$\delta_1 = 13.18 \quad \text{and} \quad \delta_2 = 15.47 \tag{5.2}$$

for $\nu = 0.1$. The transition curves used for the minimization are shown in Figure 5.11(a) along with the data points (squares) for $\tau = 0$ and the optimal predicted points (dots) for the non-zero τ hardening-to-softening transition curves, which were created by using the δ_i from Equations (5.2) in the mapping equations (5.1). As seen in the figure, the predicted transition values X_0^{tr} match the actual transition values fairly well. In fact, the maximum error between predicted and actual transition values X_0^{tr} is about 0.75 in magnitude. Compared to the usual sizes of X_0^{tr} in Figure 5.11(a), the absolute error is small.

Several transition curves and their respective predicted curves for $\nu = 0.1$ are shown in Figure 5.11(b). The values of τ are 75, 100, and 125, which are all outside the range $\tau \in [0, 50]$ that was used to determine the parameters δ_1 and δ_2 for the linear expansion rules (5.1). Furthermore, the values of β in Figure 5.11(b) are well outside the range in Figure 5.11(a) used for fitting purposes. Despite the relatively large values for τ and β, the predicted curves seem to approximate the actual hardening-to-softening transition curves fairly well, especially for relatively large β.

To get a better approximation of the transition curves for larger τ, one could increase the range of τ used in the minimization scheme to find the optimal δ_i. Furthermore, one could

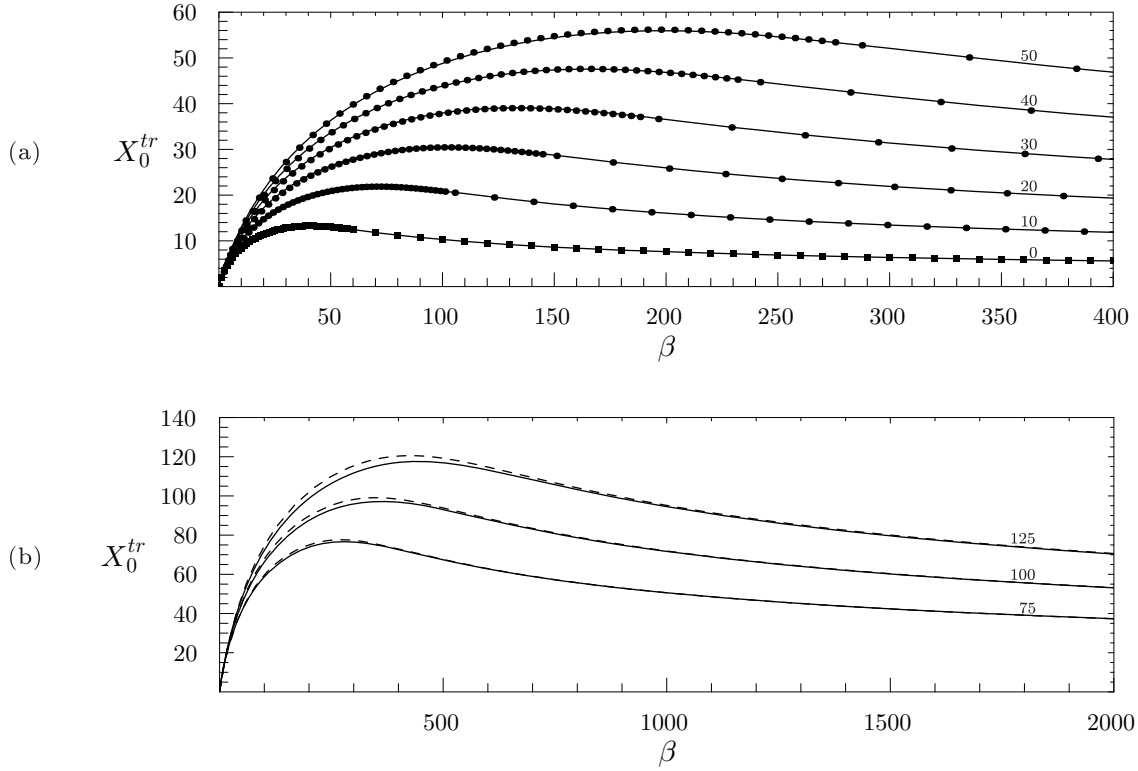

Figure 5.11: (a) Data points (squares) and predicted points (dots) near transition curves of varying τ used for parameter extraction and (b) several transition curves (solid) and respective predicted curves (dashed) for $\nu = 0.1$ and $F(r,t) = 0$.

change the mapping in Equations (5.1), perhaps by adding parabolic and cubic terms to scale the transition values for zero τ. However, we leave our scheme alone, since it is mainly used here for illustrative purposes. We have shown that the transition curves are approximately related linearly through the expansion rules in Equations (5.1). In other words, the transition curve for zero τ is scaled approximately linearly as τ changes.

The dependence of the transition curves on Poisson's ratio ν can also be estimated. Thus far, we have kept ν constant at 0.1 and varied τ. Now, we use similar fitting schemes to determine the values of δ_1 and δ_2 for other values of ν. Figure 5.12(a) shows the zero-τ transition curves for several values of $\nu \in [0, 0.5]$, and Figures 5.12(b) and 5.12(c) show the variations of δ_1 and δ_2 with ν. After choosing a value for ν, one can use its associated zero-τ curve in Figure 5.12(a) and its associated values of δ_1 and δ_2 to create the hardening-to-

softening transition curve for a given τ from the linear expansion rules (5.1).

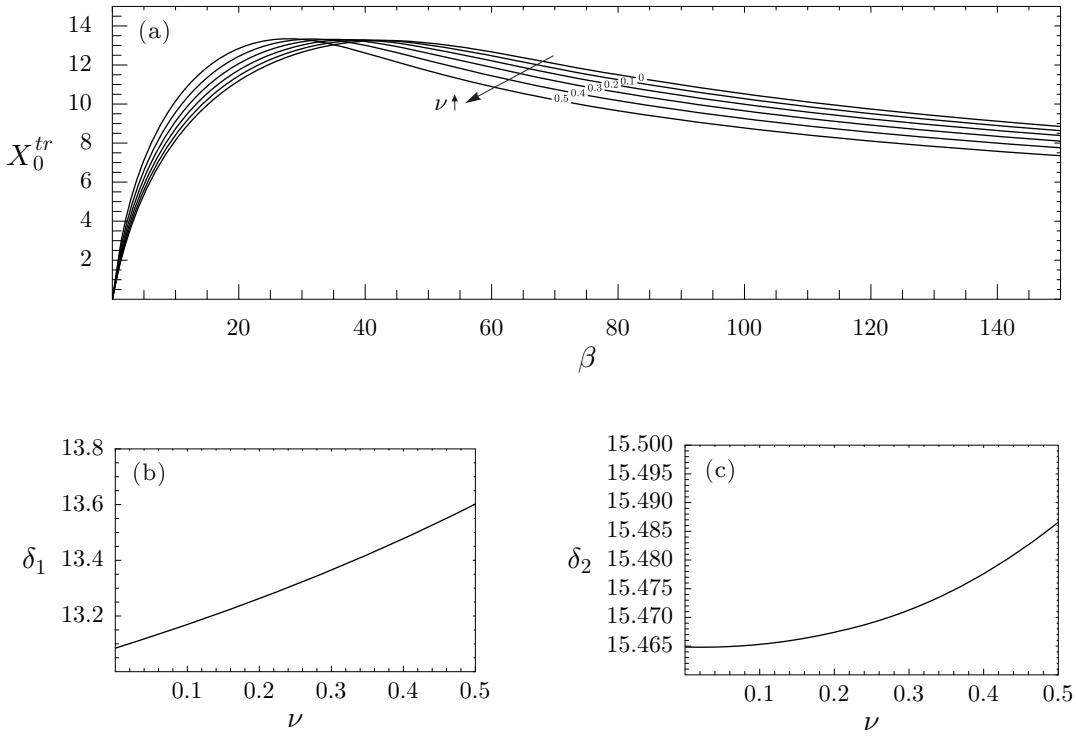

Figure 5.12: (a) Zero-τ transition curves for various ν, (b) δ_1 versus ν, and (c) δ_2 versus ν.

Chapter 6

Boundary Effects on Static Plate Behavior

6.1 Motivation

The previous problem formulation was based on clamped boundary conditions. However, as seen in Figure 6.1, the boundary of an actual CMUT may not be clamped.

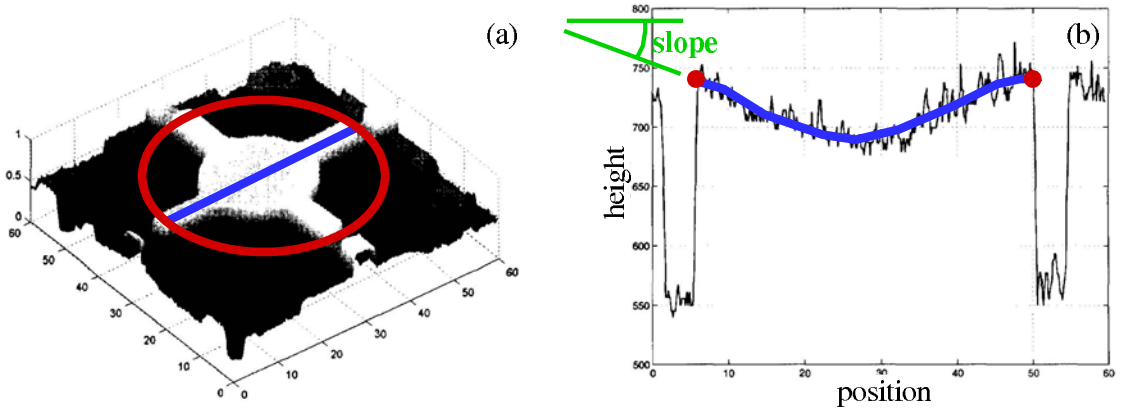

Figure 6.1: (a) An atomic force microscopy (AFM) image of a circular CMUT cell and (b) an AFM scan line of the deflected CMUT (adapted from Yaralioglu et al. (2001)).

In fact, the dynamics of CMUTs are highly influenced by the boundary conditions. Most

analytical CMUT models assume that the outer edge of the midplane is fixed and clamped for simplicity. For non-clamped outer edges, analytical models are usually abandoned for a finite-element approach. In contrast, we update our reduced-order model to account for the coupling of the plate and boundary.

6.2 Boundary Conditions

As seen in Figure 6.2, we assume that the boundary force N_{rr} and moment M_{rr} cause the plate boundary to displace horizontally ($w = 0$) and rotationally ($\frac{\partial w}{\partial r} \neq 0$ in general). Moreover, we assume that the force and moment affect the slope linearly such that the boundary conditions for w are

$$w = 0 \quad \text{at} \quad r = 1 \tag{6.1a}$$

$$\frac{\partial w}{\partial r} = -k_1 N_{rr} + k_2 M_{rr} \quad \text{at} \quad r = 1 \tag{6.1b}$$

where

$$N_{rr} = \beta \left[\frac{1}{r}\frac{\partial \Phi}{\partial r} + \frac{1}{r^2}\frac{\partial^2 \Phi}{\partial \theta^2} \right] + \tau \tag{6.2a}$$

$$M_{rr} = -\left[\frac{\partial^2 w}{\partial r^2} + \frac{\nu}{r}\left(\frac{\partial w}{\partial r} + \frac{1}{r}\frac{\partial^2 w}{\partial \theta^2} \right) \right] \tag{6.2b}$$

and k_1 and k_2 are non-negative constants. We also need conditions for the stress function Φ. For simplicity, we assume that the residual stress acts at the boundary, which means that $N_{rr} = \tau$ and

$$\frac{1}{r}\frac{\partial \Phi}{\partial r} + \frac{1}{r^2}\frac{\partial^2 \Phi}{\partial \theta^2} = 0 \quad \text{at} \quad r = 1 \tag{6.3}$$

Also, since Φ is known to within an arbitrary function of time (Nayfeh and Pai, 2004), we only need to solve for $\partial\Phi/\partial r$. Thus, the axisymmetric boundary conditions are

$$w = 0 \qquad \text{at} \quad r = 1 \tag{6.4a}$$

$$\frac{\partial w}{\partial r} = -K_\tau - K_2 \frac{\partial^2 w}{\partial r^2} \qquad \text{at} \quad r = 1 \tag{6.4b}$$

$$\frac{\partial \Phi}{\partial r} = 0 \qquad \text{at} \quad r = 1 \tag{6.4c}$$

$$w < \infty \ \text{ and } \ \Phi < \infty \qquad \text{at} \quad r = 0 \tag{6.4d}$$

where $K_\tau = \frac{k_1 \tau}{1 + k_2 \nu}$ and $K_2 = \frac{k_2}{1 + k_2 \nu}$.

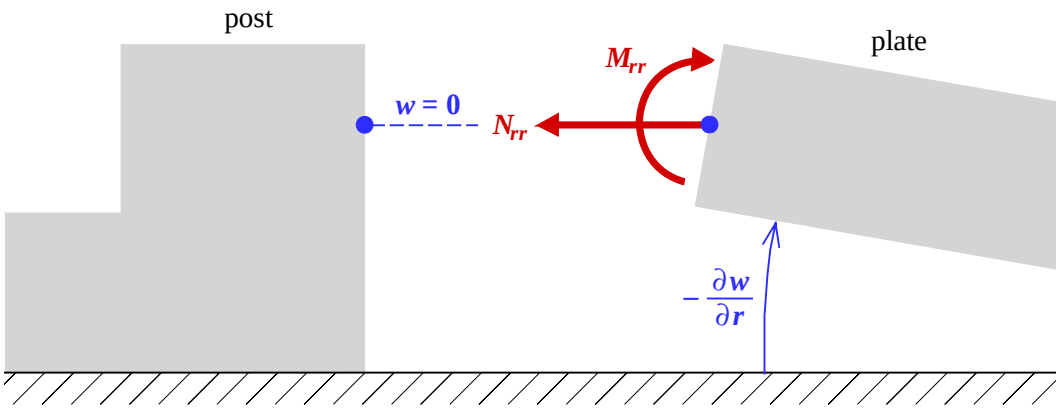

Figure 6.2: Boundary conditions for the updated macromodel.

6.3 Galerkin Approach for Axisymmetric Motion

For axisymmetric motion, Equations (6.4) need to be solved with the two governing equations, repeated here for convenience:

$$\frac{\partial^2 w}{\partial t^2} + 2c\frac{\partial w}{\partial t} + \nabla^4 w = \frac{\beta}{r}\frac{\partial}{\partial r}\left(\frac{\partial w}{\partial r}\frac{\partial \Phi}{\partial r}\right) + \frac{\tau}{r}\frac{\partial}{\partial r}\left(r\frac{\partial w}{\partial r}\right) + F(r,t) + \frac{v^2(t)}{(1-w)^2} \tag{6.5}$$

$$\nabla^4 \Phi = -\frac{1}{r}\frac{\partial^2 w}{\partial r^2}\frac{\partial w}{\partial r} \tag{6.6}$$

Once again, we use a Galerkin approach to find approximate solutions. However, an additional static deflection is included because of the non-clamped boundary conditions. Accordingly, we approximate $w(r,t)$ as

$$w(r,t) = w_s(r) + \sum_{m=1}^{N} \eta_m(t)\phi_m(r) \tag{6.7}$$

where $w_s(r)$ is given by

$$\nabla^4 w_s = 0 \qquad \forall \;\; r \in (0,1) \tag{6.8a}$$

$$w_s = 0 \qquad \text{at} \;\; r = 1 \tag{6.8b}$$

$$w_s' = -K_\tau - K_2 w_s'' \qquad \text{at} \;\; r = 1 \tag{6.8c}$$

$$w_s < \infty \qquad \text{at} \;\; r = 0 \tag{6.8d}$$

Also, we choose the shape functions $\phi_m(r)$ to be the axisymmetric modes of the linear undamped and unforced plate. It follows from Equation (6.5) that the governing equation is

$$\ddot{w} + \nabla^4 w = 0 \tag{6.9}$$

Thus, $\phi_m(r)$ is the mth shape function; it is the solution of

$$\nabla^4 \phi_m - \omega_m^2 \phi_m = 0 \qquad \forall \ r \in (0,1) \tag{6.10a}$$

$$\phi_m = 0 \qquad \text{at} \ \ r = 1 \tag{6.10b}$$

$$\phi_m' = -K_2 \phi_m'' \qquad \text{at} \ \ r = 1 \tag{6.10c}$$

$$\phi_m < \infty \qquad \text{at} \ \ r = 0 \tag{6.10d}$$

In Equation (6.7), $\eta_m(t)$ is the mth generalized coordinate for the mth shape function and ω_m is the corresponding frequency. Consequently, Equation (6.7) satisfies the conditions for $w(r,t)$ in Equations (6.4) and the equation of motion (6.9).

6.3.1 Static Deflection

Solving Equations (6.8) yields the static deflection

$$w_s(r) = K_1(1 - r^2) \tag{6.11}$$

where $K_1 = \frac{K_\tau}{2(1+K_2)}$.

6.3.2 Shape Functions

The general solution of Equations (6.10a) that is bounded at the origin can be expressed as

$$\phi_m(r) = c_1 J_n(\alpha_m r) + c_2 I_n(\alpha_m r) \tag{6.12}$$

where $\alpha_m = \sqrt{\omega_m}$ and c_1 and c_2 are determined by the boundary conditions. Imposing the boundary conditions, Equations (6.10b) and (6.10c), we obtain

$$\begin{bmatrix} J_n(\alpha_m) & I_n(\alpha_m) \\ J_n'(\alpha_m) + \alpha_m K_2 J_n''(\alpha_m) & I_n'(\alpha_m) + \alpha_m K_2 I_n''(\alpha_m) \end{bmatrix} \begin{Bmatrix} c_1 \\ c_2 \end{Bmatrix} = \begin{Bmatrix} 0 \\ 0 \end{Bmatrix} \tag{6.13}$$

A nontrivial solution requires that the determinant of the matrix is zero; that is,

$$\big[J_n(\alpha_m)I_n'(\alpha_m) - I_n(\alpha_m)J_n'(\alpha_m)\big] + \alpha_m K_2\big[J_n(\alpha_m)I_n''(\alpha_m) - I_n(\alpha_m)J_n''(\alpha_m)\big] = 0 \quad (6.14)$$

Given K_2, one can find all α_m (and hence all ω_m) required for the Galerkin approach. Figure 6.3 shows the values for the axisymmetric modes. According to Equation (6.10c), the

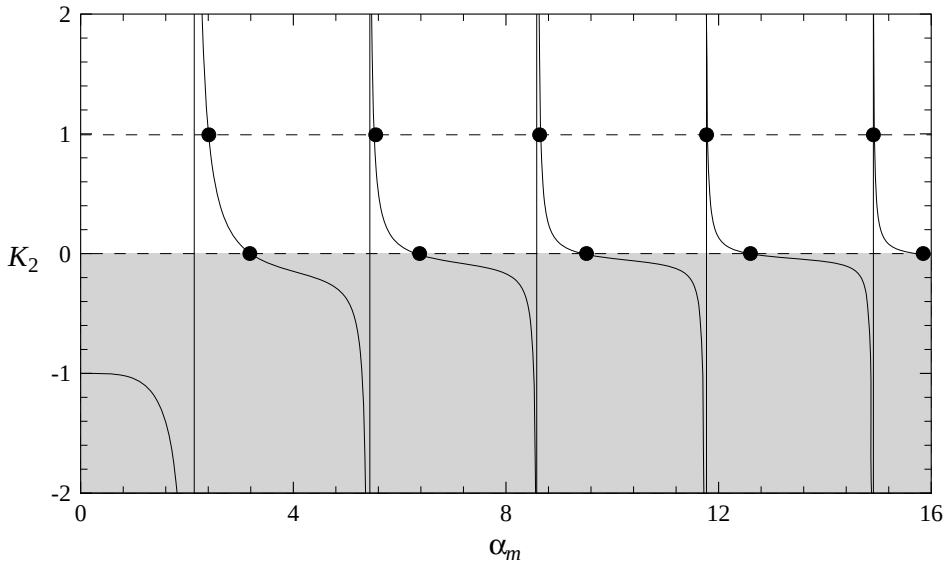

Figure 6.3: K_2 versus α_m for the axisymmetric modes. Solid dots represent the α_m for the given K_2 of a dashed line.

$K_2 = 0$ case represents a sliding-clamped boundary for $\phi_m(r)$. As the clamped condition loosens with increasing K_2, the natural frequencies decrease as seen in Figure 6.3. The first six axisymmetric modes for various K_2 values are seen in Figure 6.4.

6.3.3 Stress Function

Like the plate deflection $w(r,t)$, the stress function $\Phi(r,t)$ also needs to be discretized and solved to within arbitrary generalized coordinates $\eta_i(t)$. We begin by noting that Equation (6.6) becomes

$$r\,\frac{\partial^3\Phi}{\partial r^3} + \frac{\partial^2\Phi}{\partial r^2} - \frac{1}{r}\frac{\partial\Phi}{\partial r} = -\frac{1}{2}\left(\frac{\partial w}{\partial r}\right)^2 \quad (6.15)$$

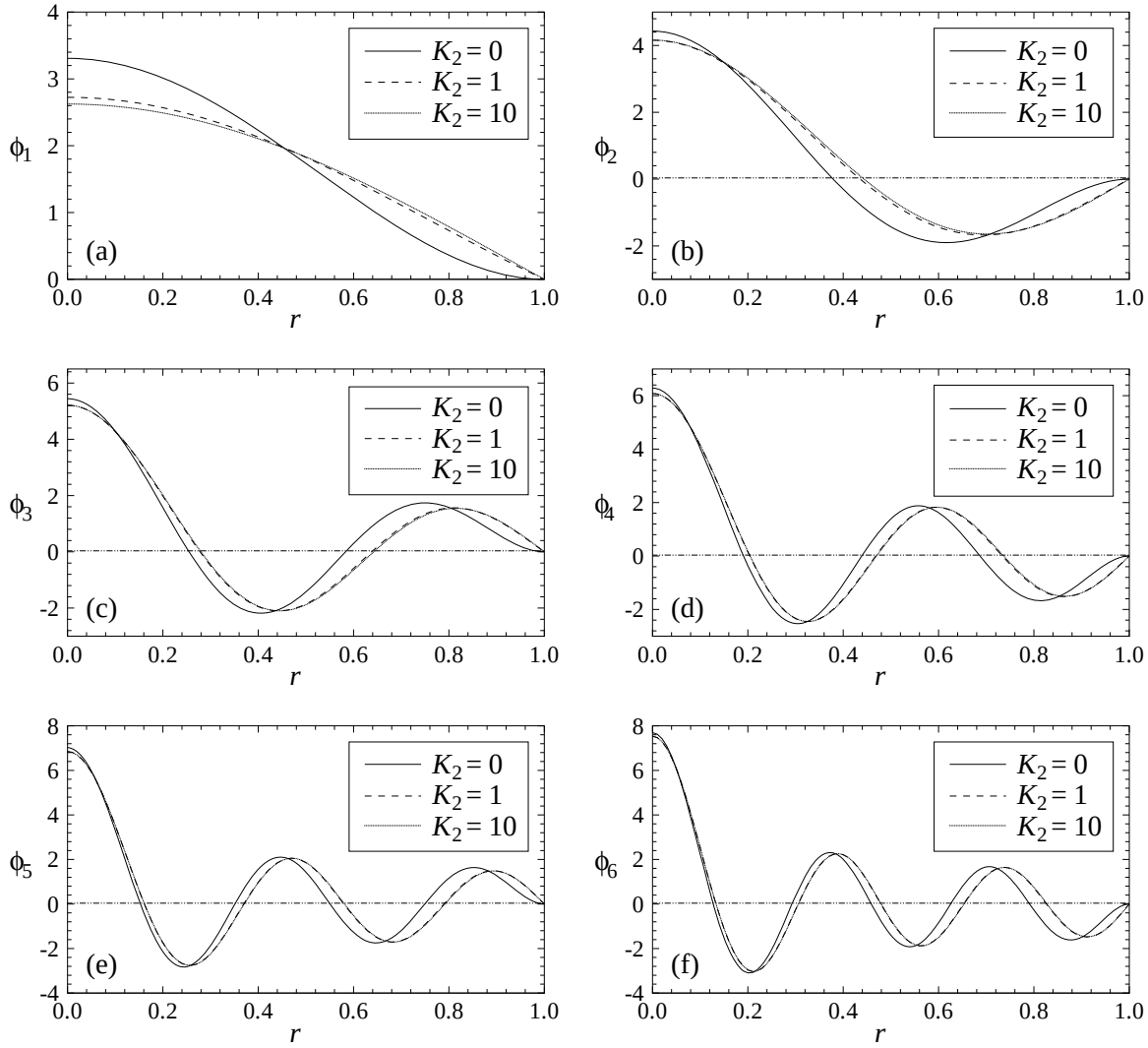

Figure 6.4: (a) $\phi_1(r)$, (b) $\phi_2(r)$, etc. for various K_2 values.

for axisymmetric motion (Nayfeh and Pai, 2004). Substitution of Equation (6.7) into Equation (6.15) yields

$$r\frac{\partial^3\Phi}{\partial r^3} + \frac{\partial^2\Phi}{\partial r^2} - \frac{1}{r}\frac{\partial\Phi}{\partial r} = -\frac{1}{2}\left[w_s'(r) + \sum_{i=1}^{N}\eta_i(t)\phi_i'(r)\right]^2 \tag{6.16}$$

Consequently, we seek the solution of Φ in the form

$$\Phi(r,t) = \Phi_s(r) + \sum_{m=1}^{N}\eta_m(t)\Gamma_m(r) + \sum_{m,n=1}^{N}\eta_m(t)\eta_n(t)\psi_{mn}(r) \tag{6.17}$$

We substitute Equation (6.17) into Equation (6.16), collect terms for general η_i, and obtain

$$r\Phi_s''' + \Phi_s'' - \frac{1}{r}\Phi_s' = -\frac{1}{2}\left(w_s'\right)^2 \tag{6.18a}$$

$$r\Gamma_m''' + \Gamma_m'' - \frac{1}{r}\Gamma_m' = -w_s'\phi_m' \tag{6.18b}$$

$$r\psi_{mn}''' + \psi_{mn}'' - \frac{1}{r}\psi_{mn}' = -\frac{1}{2}\phi_m'\phi_n' \tag{6.18c}$$

for m, $n = 1, 2, \ldots N$. It follows from Equations (6.4) that the boundary conditions are

$$\Phi_s' = 0 \text{ at } r = 1 \text{ with } \Phi_s < \infty \text{ at } r = 0 \tag{6.19a}$$

$$\Gamma_m' = 0 \text{ at } r = 1 \text{ with } \Gamma_m < \infty \text{ at } r = 0 \tag{6.19b}$$

$$\psi_{mn}' = 0 \text{ at } r = 1 \text{ with } \psi_{mn} < \infty \text{ at } r = 0 \tag{6.19c}$$

The three systems of Equations (6.18) and (6.19) are of the same form:

$$rf''' + f'' - \frac{1}{r}f' = g(r) \tag{6.20a}$$

$$f' = 0 \text{ at } r = 1 \tag{6.20b}$$

$$f < \infty \text{ at } r = 0 \tag{6.20c}$$

where

$$f = \Phi_s \text{ and } g = -\frac{1}{2}\left(w_s'\right)^2 \tag{6.21a}$$

$$f = \Gamma_m \text{ and } g = -w_p'\phi_m' \tag{6.21b}$$

$$f = \psi_{mn} \text{ and } g = -\frac{1}{2}\phi_m'\phi_n' \tag{6.21c}$$

respectively. To solve Equations (6.20), we let $v = f'$ and rewrite Equation (6.20a) as

$$rv'' + v' - \frac{1}{r}f = g(r) \tag{6.22}$$

Using the method of variation of parameters and noting that two linear independent solutions of the homogeneous form of Equation (6.22) are r and r^{-1}, we express the general solution of Equation (6.20a) as

$$f' = c_1(r)r + c_2(r)r^{-1} \tag{6.23}$$

We then follow an approach similar to that of Nayfeh and Pai (2004) and express the solution of Equations (6.20) as

$$f' = \frac{r}{2}\int_1^r \frac{g(\xi)}{\xi}d\xi - \frac{1}{2r}\int_0^r g(\xi)\xi d\xi + \frac{r}{2}\int_0^1 g(\xi)\xi d\xi \tag{6.24}$$

Finally, substitution of Equations (6.21) into Equation (6.24) and application of Equation (6.11) yields

$$\Phi_s' = \frac{1}{4}K_1^2\left(r - r^3\right) \tag{6.25a}$$

$$\Gamma_m' = rK_1\int_1^r \phi_m' d\xi - \frac{K_1}{r}\int_0^r \xi^2\phi_m' d\xi + rK_1\int_0^1 \xi^2\phi_m' d\xi \tag{6.25b}$$

$$\psi_{mn}' = -\frac{r}{4}\int_1^r \frac{\phi_m'\phi_n'}{\xi}d\xi + \frac{1}{4r}\int_0^r \xi\phi_m'\phi_n' d\xi - \frac{r}{4}\int_0^1 \xi\phi_m'\phi_n' d\xi \tag{6.25c}$$

Consequently, having solved Equation (6.6) and its associated boundary conditions, we express the partial derivative $\partial\Phi/\partial r$ required for the first governing equation (6.5) as

$$\frac{\partial\Phi}{\partial r} = \Phi_s' + \sum_{m=1}^{N}\eta_m(t)\Gamma_m' + \sum_{m,n=1}^{N}\eta_m(t)\eta_n(t)\psi_{mn}' \tag{6.26}$$

6.4 Updated Reduced-Order Model

We substitute Equations (6.7) and (6.26) into Equation (6.5) and obtain

$$\begin{aligned}\left(\ddot{\eta}_m + 2c\dot{\eta}_m + \omega_m^2\eta_m\right)\phi_m = \frac{\beta}{r}\frac{\partial}{\partial r}\Big[\left(w_s' + \eta_m\phi_m'\right)\left(\Phi_s' + \eta_m\Gamma_m' + \eta_m\eta_n\psi_{mn}'\right)\Big] \\ + \frac{\tau}{r}\frac{\partial}{\partial r}\Big[r\left(w_s' + \eta_m\phi_m'\right)\Big] + F(r,t) + v^2(t)\Big[1 - \left(w_s + \eta_m\phi_m\right)\Big]^{-2}\end{aligned} \tag{6.27}$$

for $q = 1, 2, \ldots, N$ with the summation signs for m and n removed for notation simplification. Next, we rearrange Equation (6.27) and rewrite it as

$$\begin{aligned}\left(\ddot{\eta}_m + 2c\dot{\eta}_m + \omega_m^2\eta_m\right)\phi_m = \frac{\beta}{r}\frac{\partial}{\partial r}\left[f + \eta_m f_m + \eta_m\eta_n f_{mn} + \eta_m\eta_n\eta_p f_{mnp}\right] \\ + \frac{\tau}{r}\frac{\partial}{\partial r}\left[g + \eta_m g_m\right] + F(r,t) + v^2(t)\Big[1 - \left(w_s + \eta_m\phi_m\right)\Big]^{-2}\end{aligned} \tag{6.28}$$

where

$$f = w_s' \Phi_s' \tag{6.29a}$$

$$f_m = w_s' \Gamma_m' + \phi_m' \Phi_s' \tag{6.29b}$$

$$f_{mn} = w_s' \psi_{mn}' + \phi_m' \Gamma_n' \tag{6.29c}$$

$$f_{mnp} = \psi_{mn}' \phi_p' \tag{6.29d}$$

$$g = r w_s' \tag{6.29e}$$

$$g_m = r \phi_m' \tag{6.29f}$$

for $m,\ n,\ p = 1, 2, \ldots N$. Then, we multiply Equation (6.28) with $\Big[1 - (w_s + \eta_m \phi_m)\Big]^2$, multiply every term by $r\phi_q$, integrate the outcome over $r \in [0, 1]$, and obtain after much rearranging

$$\begin{aligned}
&\left(\ddot{\eta}_m + 2c\dot{\eta}_m + \omega_m^2 \eta_m\right) \Big[A_{mq} + \eta_i A_{imq} + \eta_i \eta_j A_{ijmq}\Big] \\
&\quad = \beta \Big[B_q + \eta_m B_{mq} + \eta_m \eta_n B_{mnq} + \eta_m \eta_n \eta_p B_{mnpq} + \eta_i \eta_m \eta_n \eta_p B_{imnpq} \\
&\qquad + \eta_i \eta_j \eta_m \eta_n \eta_p B_{ijmnpq}\Big] \\
&\qquad + \tau \Big[C_q + \eta_m C_{mq} + \eta_i \eta_m C_{imq} + \eta_i \eta_j \eta_m C_{ijmq}\Big] \\
&\qquad + I_q + \eta_i J_{iq} + \eta_i \eta_j K_{ijq} + v^2(t) L_q
\end{aligned} \tag{6.30}$$

where

$$A_{mq} = \int_0^1 (1 - w_s)^2 \, r\phi_m\phi_q dr \tag{6.31a}$$

$$A_{imq} = -2\int_0^1 (1 - w_s) \, r\phi_i\phi_m\phi_q dr \tag{6.31b}$$

$$A_{ijmq} = \int_0^1 r\phi_i\phi_j\phi_m\phi_q dr \tag{6.31c}$$

$$B_q = -\int_0^1 f\left[(1 - w_s)^2 \phi_q\right]' dr \tag{6.31d}$$

$$B_{mq} = -\int_0^1 f_m\left[(1 - w_s)^2 \phi_q\right]' dr + 2\int_0^1 f\left[(1 - w_s)\phi_m\phi_q\right]' dr \tag{6.31e}$$

$$\begin{aligned} B_{mnq} = &-\int_0^1 f_{mn}\left[(1 - w_s)^2 \phi_q\right]' dr + 2\int_0^1 f_m\left[(1 - w_s)\phi_n\phi_q\right]' dr \\ &-\int_0^1 f\left[\phi_m\phi_n\phi_q\right]' dr \end{aligned} \tag{6.31f}$$

$$\begin{aligned} B_{mnpq} = &-\int_0^1 f_{mnp}\left[(1 - w_s)^2 \phi_q\right]' dr + 2\int_0^1 f_{mn}\left[(1 - w_s)\phi_p\phi_q\right]' dr \\ &-\int_0^1 f_m\left[\phi_n\phi_p\phi_q\right]' dr \end{aligned} \tag{6.31g}$$

$$B_{imnpq} = 2\int_0^1 f_{mnp}\left[(1 - w_s)\phi_i\phi_q\right]' dr - \int_0^1 f_{mn}\left[\phi_i\phi_p\phi_q\right]' dr \tag{6.31h}$$

$$B_{ijmnpq} = -\int_0^1 f_{mnp}\left[\phi_i\phi_j\phi_q\right]' dr \tag{6.31i}$$

$$C_q = -\int_0^1 g\left[(1 - w_s)^2 \phi_q\right]' dr \tag{6.31j}$$

$$C_{mq} = -\int_0^1 g_m\left[(1 - w_s)^2 \phi_q\right]' dr + 2\int_0^1 g\left[(1 - w_s)\phi_m\phi_q\right]' dr \tag{6.31k}$$

$$C_{imq} = 2\int_0^1 g_m\left[(1 - w_s)\phi_i\phi_q\right]' dr - \int_0^1 g\left[\phi_i\phi_m\phi_q\right]' dr \tag{6.31l}$$

$$C_{ijmq} = -\int_0^1 g_m\left[\phi_i\phi_j\phi_q\right]' dr \tag{6.31m}$$

$$I_q = \int_0^1 F(1 - w_s)^2 \, r\phi_q dr \tag{6.31n}$$

$$J_{iq} = -2\int_0^1 F(1 - w_s) \, r\phi_i\phi_q dr \tag{6.31o}$$

$$K_{ijq} = \int_0^1 Fr\phi_i\phi_j\phi_q dr \tag{6.31p}$$

$$L_q = \int_0^1 r\phi_q dr \tag{6.31q}$$

We collect all of the $\eta_m(t)$ into a column vector $\boldsymbol{\eta}(t)$, rearrange Equation (6.30), and obtain

$$M(\boldsymbol{\eta})\ddot{\boldsymbol{\eta}} + 2cM(\boldsymbol{\eta})\dot{\boldsymbol{\eta}} + N(\boldsymbol{\eta})\boldsymbol{\eta} = P(\boldsymbol{\eta}) + v^2(t)\boldsymbol{L} \tag{6.32}$$

where

$$M(\boldsymbol{\eta}) = [M_{qm}(\boldsymbol{\eta})] = [(A_{mq} + \eta_i A_{imq} + \eta_i\eta_j A_{ijmq})] \tag{6.33a}$$

$$N(\boldsymbol{\eta}) = [N_{qm}(\boldsymbol{\eta})] = [\omega_m^2(A_{mq} + \eta_i A_{imq} + \eta_i\eta_j A_{ijmq})] \tag{6.33b}$$

$$\begin{aligned} P(\boldsymbol{\eta}) = \{P_q(\boldsymbol{\eta})\} = \Big\{ &\beta\big(B_q + \eta_m B_{mq} + \eta_m\eta_n B_{mnq} + \eta_m\eta_n\eta_p B_{mnpq} \\ &+ \eta_i\eta_m\eta_n\eta_p B_{imnpq} + \eta_i\eta_j\eta_m\eta_n\eta_p B_{ijmnpq}\big) \\ &+ \tau\big(C_q + \eta_m C_{mq} + \eta_i\eta_m C_{imq} + \eta_i\eta_j\eta_m C_{ijmq}\big) \\ &+ (I_q + \eta_i J_{iq} + \eta_i\eta_j K_{ijq})\Big\} \end{aligned} \tag{6.33c}$$

$$\boldsymbol{L} = \{L_q\} \tag{6.33d}$$

with Einstein's convention holding only within pairs of parentheses.

Once all of the $\eta_m(t)$ are determined by solving the nonlinear matrix equation (6.32), the plate deflection $w(r,t)$ is given approximately by Equation (6.7).

6.5 Static Behavior Under Electrostatic Actuation

Figure 6.5 shows the axisymmetric deflections at pull-in for various values of K_1 and K_2 and some chosen parameters. As seen in Figures 6.5(a), 6.5(c), and 6.5(e), the plate deflects more as K_1 increases. This behavior is expected, since a larger K_1 means that the stress at the plate boundary causes a greater static deflection $w_s(r)$, as seen in Equation (6.11). The greater deflections also lead to lower pull-in voltages, as seen in Figures 6.5(b), 6.5(d), and 6.5(f).

As seen in Figures 6.5(b), 6.5(d), and 6.5(f), the pull-in curves shift leftward with K_2 for all K_1; that is, the plate becomes more sensitive to voltage as K_2 increases. This happens because, as K_2 increases towards its limit of $1/\nu = 1/0.1 = 10$, every ϕ_i transitions from being a sliding-clamped to a sliding-simply-supported mode, seen especially in Figure 6.5(a).

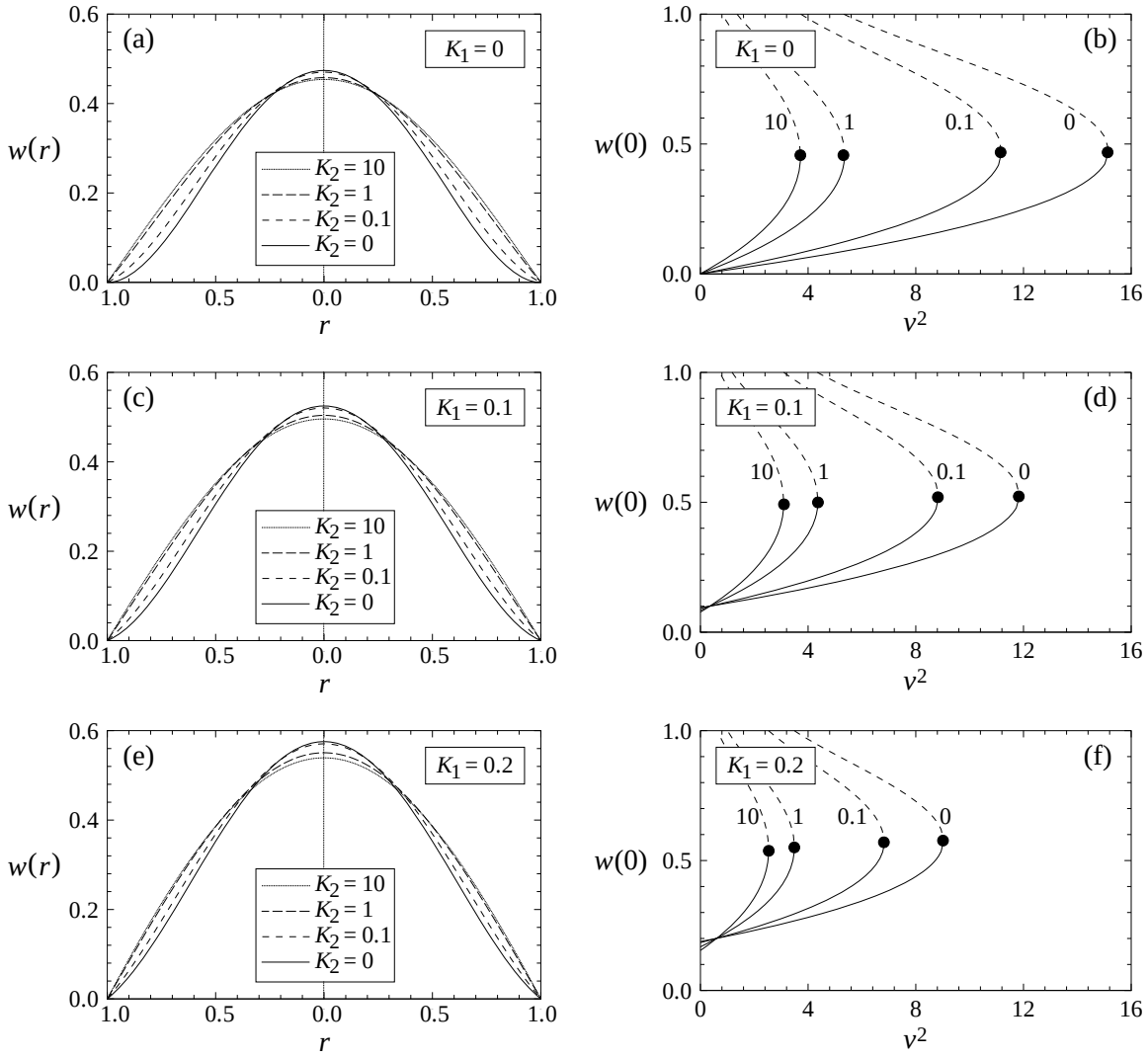

Figure 6.5: Center deflection $w(0)$ versus electric forcing v^2 in (b), (d), and (f) with the dots denoting pull-in points. The corresponding deflections $w(r)$ at pull-in are plotted in (a), (c), and (e). For all values of K_1 and K_2, Equation (6.7) was solved with $N = 2$, $\beta = 1$, $\nu = 0.1$, $\tau = 1$, and $F(r,t) = 0$.

6.6 First Validation of Static Behavior of Updated Macromodel

Bayram et al. (2001) performed FEM simulations with ANSYS to determine how sizes and

locations of embedded, centered electrodes affect the collapse voltage of a circular silicon-nitride membrane for possible applications in CMUTs. We can apply the updated reduced-order model for the case in which the electrode is of zero thickness. Figure 6.6 shows cross-sectional views of the axisymmetric CMUT for FEM and reduced-order modelings. Because the CMUT studied by Bayram et al. had no residual stress, the parameter K_1 is zero. Thus, the only unknown model parameter is K_2. It will be found using some of the results from Bayram et al. and then it will be used in the macromodel to predict their remaining numerical results.

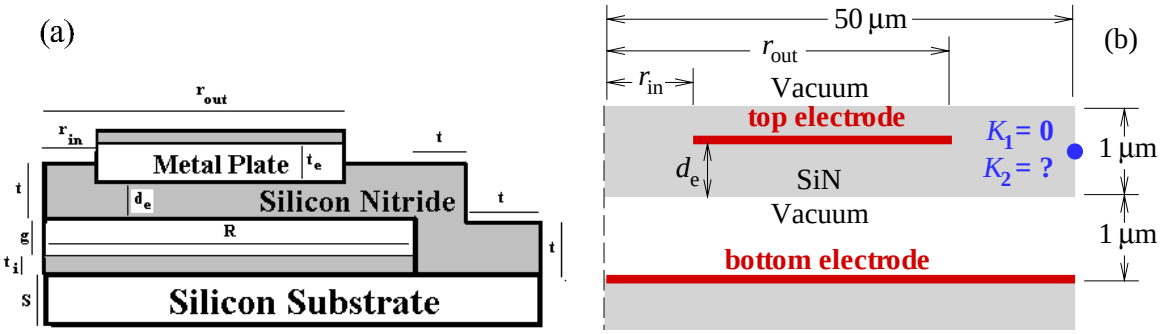

Figure 6.6: (a) A schematic of a CMUT with an electrode of variable size and position for FEM simulation (from Bayram et al. (2001)) and (b) a schematic of a similar CMUT with an electrode of zero thickness for reduced-order model simulation.

To find K_2, we first use Figure 6.6(b) to modify the macromodel. If the parallel plate assumption still holds, the electrostatic forcing term is modified in Equation (6.5) such that

$$\frac{\partial^2 w}{\partial t^2} + 2c\frac{\partial w}{\partial t} + \nabla^4 w = \frac{\beta}{r}\frac{\partial}{\partial r}\left(\frac{\partial w}{\partial r}\frac{\partial \Phi}{\partial r}\right) + \frac{\tau}{r}\frac{\partial}{\partial r}\left(r\frac{\partial w}{\partial r}\right) + F(r,t) + H(r)\frac{v^2(t)}{(1-w)^2} \tag{6.34}$$

where

$$H(r) = \begin{cases} 1, & r_{\text{in}} < r < r_{\text{out}} \\ 0, & \text{elsewhere} \end{cases} \tag{6.35}$$

with r_{in} and r_{out} being nondimensionalized with respect to R for this function. The modified Heaviside function $H(r)$ ensures that the electric forcing is only applied to the portion of the

plate that is covered by the electrode. Consequently, the macromodel is the same except that

$$L_q = \int_{r_{\text{in}}}^{r_{\text{out}}} r\phi_q dr \tag{6.36}$$

To ensure that the parallel plate assumption holds, we need to make sure that $d \ll (r_{\text{out}} - r_{\text{in}})$. Because $d \sim 1$ μm, we let

$$(r_{\text{out}} - r_{\text{in}}) \geq 20 \ \mu\text{m} \tag{6.37}$$

6.6.1 Fit of Macromodel

With the material parameters listed in Table 6.1, Bayram et al. (2001) performed FEM simulations of the configuration in Figure 6.6(a). They predicted the pull-in voltages for an upper electrode with no thickness ($t_{\text{e}} = 0$) and no inner radius ($r_{\text{in}} = 0$) but with variable outer radius r_{out}. Because the electrode has no thickness, it does not contribute any additional stiffness to the plate. Consequently, the macromodel can be used in this case, as seen in Figure 6.6(b). In fact, only the material properties for Si_3N_4 and Vacuum in Table 6.1 are required. As a result, the reduced-order model uses the parameters $\beta = 15.43$, $\nu = 0.263$, $\tau = 0$, and $F(r,t) = 0$.

Table 6.1: Material parameters used by Bayram et al. (2001) in their FEM simulations.

Material	Si_3N_4	Vacuum	Si	Al	Au
Young's Modulus (GPa)	320		169	67.6	80.6
Density (kg/m^3)	3270		2332	2700	19700
Poisson's ratio	0.263			0.3555	0.4205
Relative Permittivity	5.7	1	11.8		

We determined that $K_2 = 0.016$ by matching the macromodel pull-in voltage at $r_{\text{out}} = 50$ μm to the corresponding FEM result. The largest outer radius was used for parameter extraction because the parallel-plate approximation is most valid for a fully-metalized plate.

Figure 6.7 contains macromodel predictions for the extracted K_2 and its limiting cases of sliding-clamped ($K_2 = 0$) and sliding-simply-supported ($K_2 = 1/\nu$) boundary conditions. As

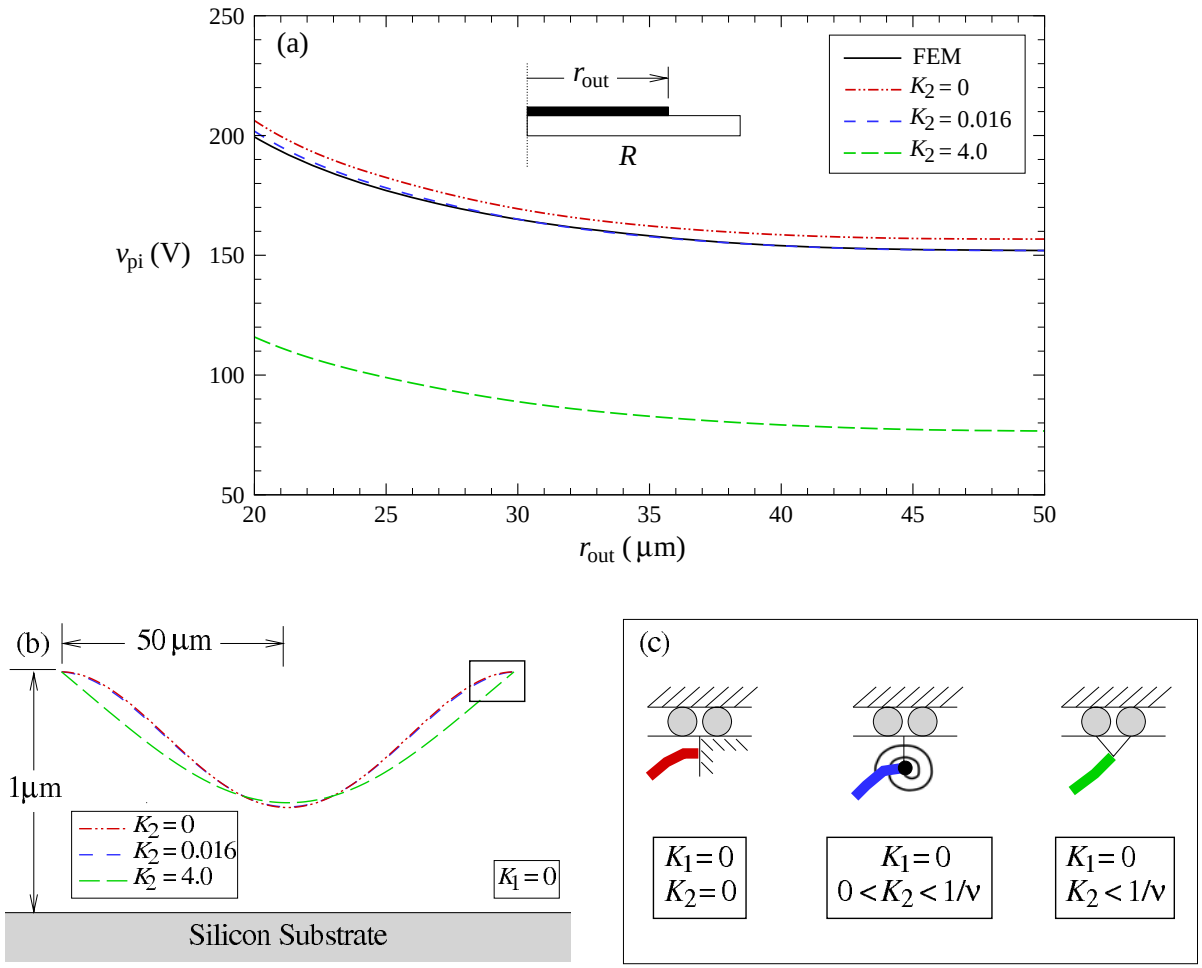

Figure 6.7: (a) Pull-in voltage versus electrode outer radius for $K_1 = 0$ and various K_2 with the system parameters from Bayram et al. (2001), (b) plate deflections at pull-in for $r_{out} = 35$ μm, and (c) schematics of the boundary conditions for the three different regimes for $K_1 = 0$.

seen in Figure 6.7(a), the pull-in voltages for the macromodel and FEM are very close to each other, even at $r_{out} = 20$ μm. The pull-in curves for $K_2 = 0$ are close to those for $K_2 = 0.016$, but can deviate by as much as 2.5%. On the other hand, the plate deflections at pull-in

for $K_2 = 0$ and $K_2 = 0.016$ in Figure 6.7(b) are visually indistinguishable. Therefore, it is important to model the boundary conditions as not being clamped in order to yield correct pull-in values, even if the plate may appear to be clamped.

Bayram et al. (2001) also predicted the pull-in voltages for an upper electrode with no thickness ($t_e = 0$) and a variable inner radius r_{in} but with a fixed outer radius ($r_{out} = 50$ μm). Using the reduced-order model with $K_2 = 0.016$, we predict the pull-in voltages for varying r_{in}, as seen in Figure 6.8(a). In this case, the macromodel results do not match the FEM results as well as in the previous case for varying outer radius. However, the pull-in voltages match to within 1% up to $r_{in} = 15$ μm, as shown in Figure 6.8(c). The difference in accuracy between the two cases is caused by the difference in forcing, since the first case is for a circular electrode while the second case is for an annular electrode. The parallel-plate approximation is less valid for the annular electrode than for the circular one because the annular electrode has greater edge effects, which have been ignored in the macromodel but accounted for in the FEM simulations.

6.6.2 Physical Validation of Boundary Condition

Even though the macromodel and FEM results match well when $K_2 = 0.016$, this number needs to be shown to be physically realistic for the given case. Otherwise, the physics of the macromodel are not validated. Consequently, we now find an approximation of K_2.

As seen in Figure 6.9, we approximate the circular CMUT post as a locally-straight clamped cantilever with thickness t_{post} and depth b. The plate force N and moment M are applied at a height L. For the given CMUT (see Figure 6.6(b)), we have $\frac{1}{2}t_{post} < L < \frac{3}{2}t_{post}$. Next, we assume that linear beam theory (Ugural and Fenster, 1995) applies to the cantilever and obtain

$$\frac{\partial \hat{w}}{\partial \hat{r}} \approx -\frac{NL^2}{2E_{post}I_{post}} - \frac{ML}{E_{post}I_{post}} \quad \text{at} \quad \hat{r} = R \tag{6.38}$$

where the hat distinguishes a dimensional quantity from its nondimensional counterpart, E_{post} is Young's modulus for the post, and $I_{post} = \frac{1}{12}bt_{post}^3$. The force and moment exerted on the approximated post by the plate are given by $N = \hat{N}_{rr}b$ and $M = -\hat{M}_{rr}b$, respectively.

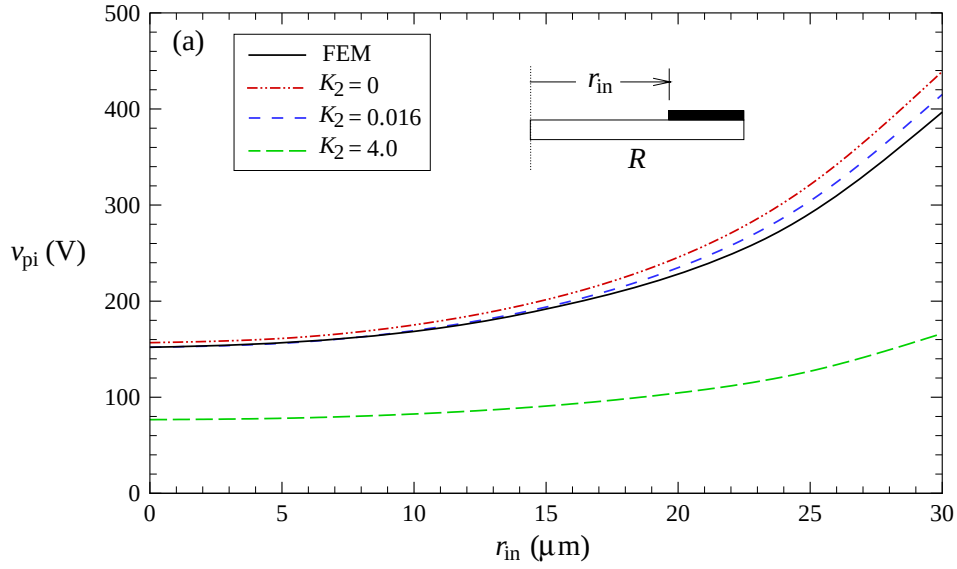

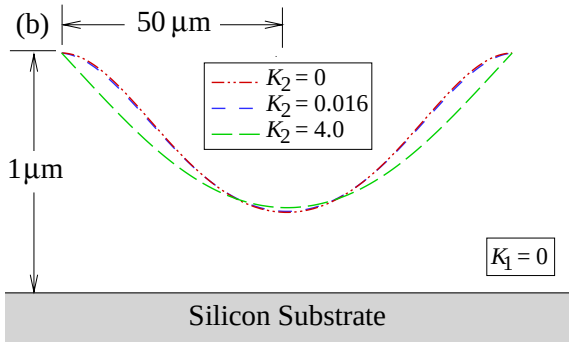

(c)

	%Error from FEM		
r_{in} (µm)	$K_2 = 0$	$K_2 = 0.016$	$K_2 = 4.0$
0	3.1	0.0	-49.6
15	5.0	1.0	-52.7
30	10.6	4.6	-58.1

Figure 6.8: (a) Pull-in voltage versus electrode inner radius for $K_1 = 0$ and various K_2 with the system parameters from Bayram et al. (2001), (b) plate deflections at pull-in for $r_{in} = 15$ μm, and (c) percentage errors of macromodel pull-in voltages from FEM results.

Hence

$$\frac{\partial \hat{w}}{\partial \hat{r}} \approx -\frac{6\hat{N}_{rr}L^2}{E_{\text{post}}t_{\text{post}}^3} + \frac{12\hat{M}_{rr}L}{E_{\text{post}}t_{\text{post}}^3} \quad \text{at} \quad \hat{r} = R \tag{6.39}$$

Furthermore, by letting $L = t_{\text{post}}$, we obtain

$$\frac{\partial \hat{w}}{\partial \hat{r}} = -\hat{k}_1\hat{N}_{rr} + \hat{k}_2\hat{M}_{rr} \quad \text{at} \quad \hat{r} = R \tag{6.40}$$

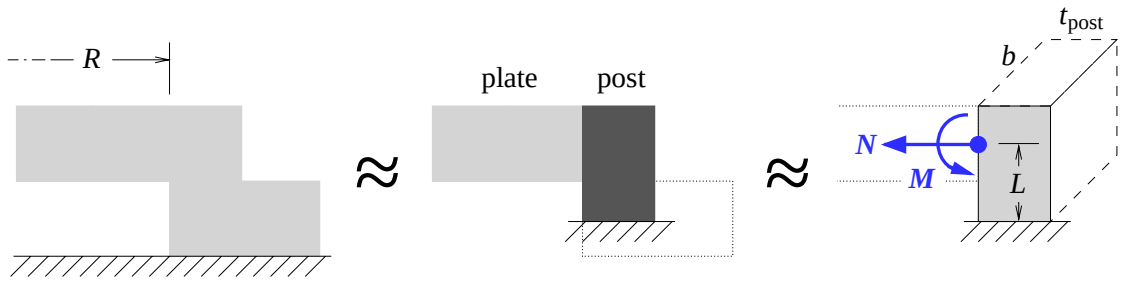

Figure 6.9: Approximation of the CMUT post as a cantilever.

where

$$\hat{k}_1 \approx \frac{6}{E_{\text{post}} t_{\text{post}}} \tag{6.41a}$$

$$\hat{k}_2 \approx \frac{12}{E_{\text{post}} t_{\text{post}}^2} \tag{6.41b}$$

Next, we nondimensionalize Equation (6.40) according to Equations (3.2) and the relations

$$\hat{N}_{rr} = \frac{D}{R^2} N_{rr} \tag{6.42a}$$

$$\hat{M}_{rr} = \frac{Dd}{R^2} M_{rr} \tag{6.42b}$$

to obtain

$$\frac{\partial w}{\partial r} = -k_1 N_{rr} + k_2 M_{rr} \quad \text{at} \quad r = 1 \tag{6.43}$$

where

$$k_1 \approx \frac{6D}{E_{\text{post}} t_{\text{post}} R d} \tag{6.44a}$$

$$k_2 \approx \frac{12D}{E_{\text{post}} t_{\text{post}}^2 R} \tag{6.44b}$$

Equations (6.44) are the needed expressions for the parameters k_1 and k_2 in Equation (6.1b). Furthermore, because $D = \frac{Eh^3}{12(1-\nu^2)}$ and $E = E_{\text{post}}$ since the plate and post are both made

of the same material, we have

$$k_1 \approx \frac{h^3}{2Rdt_{\text{post}}} \tag{6.45a}$$

$$k_2 \approx \frac{h^3}{Rt_{\text{post}}^2} \tag{6.45b}$$

Then, using the parameters in Table 6.1, we find that $k_2 \approx 0.02$. Finally, because $K_2 = \frac{k_2}{1+k_2\nu}$, we can approximate K_2 as k_2; that is,

$$K_2 \approx 0.02$$

which is close to the extracted value of 0.016. Consequently, the updated macromodel is validated for this case because (1) the pull-in voltages for the macromodel and FEM are very close to each other when $K_2 = 0.016$ and (2) the extracted K_2 is physically realistic.

6.7 Second Validation of Static Behavior of Updated Macromodel

Bozkurt et al. (1999) also performed FEM simulations with ANSYS to determine how sizes of centered electrodes affect the collapse voltage and device performance of CMUTs. Once again, we can apply the updated reduced-order model for this case in which the electrode is of zero thickness. Figure 6.10 shows cross-sectional views of the axisymmetric CMUT. Since Bozkurt et al. (1999) did not include residual stresses, K_1 is zero. Thus, the only unknown model parameter is K_2.

6.7.1 Fit of Macromodel

We used the material parameters in Table 6.1 for the CMUT of Figure 6.10 with full metalization of the plate and matched the center deflections from the FEM and macromodel deflections, resulting in $K_2 = 0.047$. For a bias voltage of 230 V, the deflections at the FEM iterations are seen in Figure 6.11 along with the macromodel result. The converged FEM and macromodel deflections are very similar, including the non-zero slope at the plate boundary. Even though the two curves deviate by as much as 7%, the maximum absolute difference is

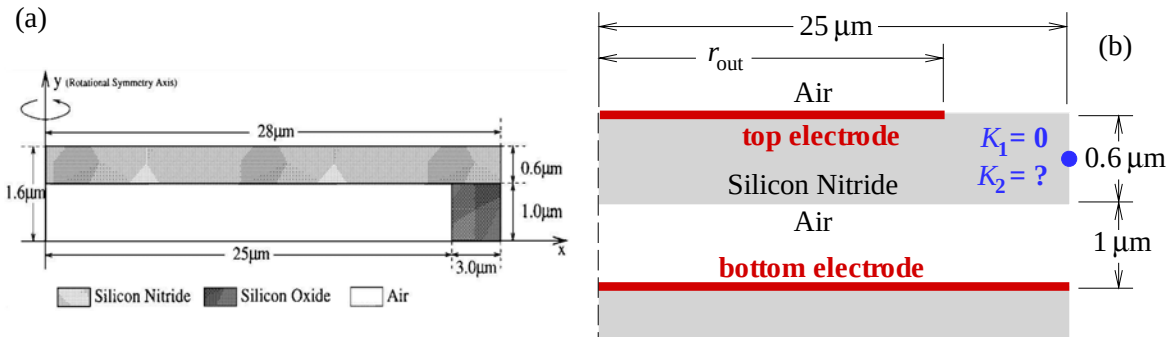

Figure 6.10: (a) A schematic of a CMUT with an electrode of variable size for FEM simulation (from Bozkurt et al. (1999)) and (b) a schematic of a similar CMUT with an electrode of zero thickness for reduced-order model simulation.

less than 0.01 μm, which is much less than the gap distance of 1 μm. In contrast, for the case of zero boundary slope (i.e., $K_2 = 0$), the deviations between the converged FEM and macromodel deflections reach almost 25%. Still worse, when the electrostatic term is additionally regarded as that for a purely parallel plate, the 'Analytic' deflection deviates even more from the FEM and macromodel results.

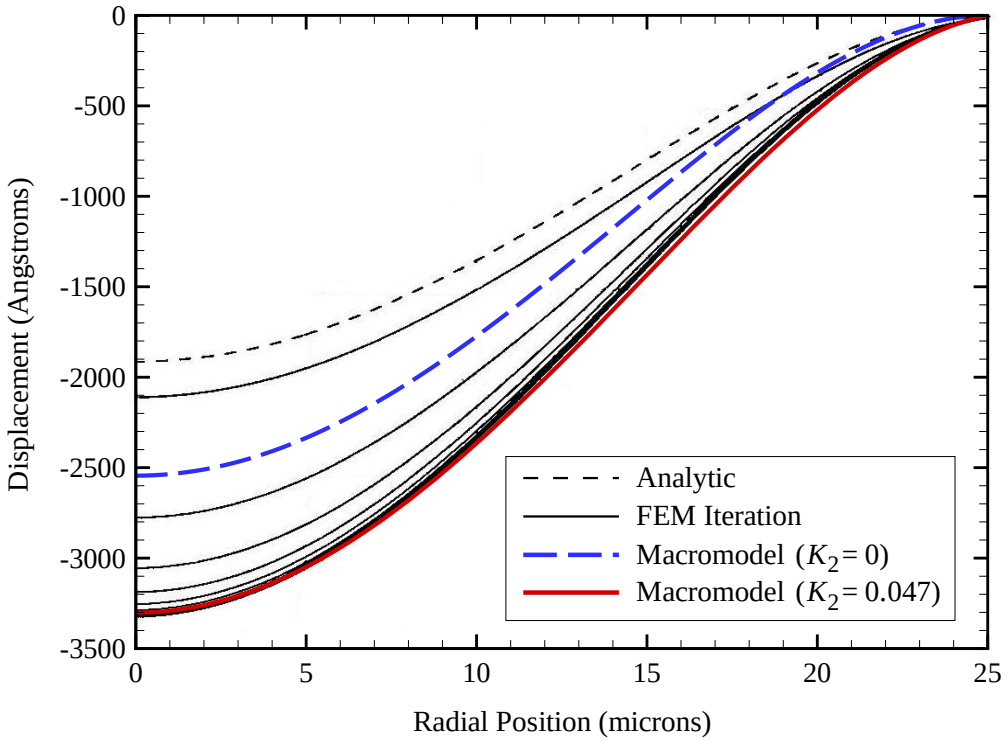

Figure 6.11: Deflection profiles for the CMUT studied by Bayram et al. (2001). The 'Analytic' profile is a special case, and the results of each FEM iteration and the macromodel are for full metalization of the plate with a bias voltage of 230 V.

Chapter 7

Effects of Electrode on CMUT Dynamics

7.1 Motivation

The model used thus far contains an electrode of infinitesimal thickness. However, actual CMUT electrodes have finite thicknesses that may considerably influence the plate behavior, such as its deflections and frequencies. In this chapter, we formulate and investigate a realistic model for CMUTs that accounts for the effects of the electrode on the plate response.

7.2 Governing Equations for Composite Part of CMUT

7.2.1 CMUT Schematic

As seen in Figure 7.1, the plate and electrode have their own Young's moduli, densities, and Poisson's ratios denoted with the 'p' and 'e' subscripts, respectively. Furthermore, the electrode has inner and outer radii of r_{in} and r_{out}, respectively.

7.2.2 Stress-Strain Relations

We now create a composite equation to govern the part of the CMUT containing the electrode. First, we rewrite the stress-strain relations in Equations (2.19) without the residual uniform

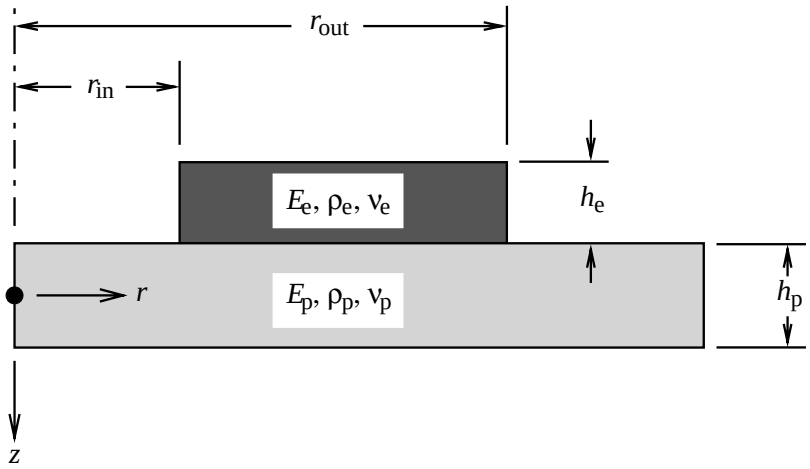

Figure 7.1: A schematic of an axisymmetric CMUT with an electrode of finite thickness and variable radii.

stress as

$$\begin{Bmatrix} \sigma_{xx} \\ \sigma_{yy} \\ \sigma_{xy} \end{Bmatrix} = [Q] \begin{Bmatrix} \epsilon_{xx} \\ \epsilon_{yy} \\ \epsilon_{xy} \end{Bmatrix} \tag{7.1}$$

where $[Q]$ is a piecewise function defined as

$$[Q] = \frac{E_\mathrm{p}}{1-\nu_\mathrm{p}^2} \begin{bmatrix} 1 & \nu_\mathrm{p} & 0 \\ \nu_\mathrm{p} & 1 & 0 \\ 0 & 0 & 1-\nu_\mathrm{p} \end{bmatrix} \quad \forall \quad -h_\mathrm{p}/2 < z \leq h_\mathrm{p}/2 \tag{7.2a}$$

$$\text{and } [Q] = \frac{E_\mathrm{e}}{1-\nu_\mathrm{e}^2} \begin{bmatrix} 1 & \nu_\mathrm{e} & 0 \\ \nu_\mathrm{e} & 1 & 0 \\ 0 & 0 & 1-\nu_\mathrm{e} \end{bmatrix} \quad \forall \quad -h_\mathrm{p}/2 - h_\mathrm{e} \leq z < -h_\mathrm{p}/2 \tag{7.2b}$$

We also rewrite Equations (2.3) in matrix form as

$$\begin{Bmatrix} \epsilon_{xx} \\ \epsilon_{yy} \\ \epsilon_{xy} \end{Bmatrix} = \begin{Bmatrix} \frac{\partial u_0}{\partial x} + \frac{1}{2}\left(\frac{\partial w}{\partial x}\right)^2 \\ \frac{\partial v_0}{\partial y} + \frac{1}{2}\left(\frac{\partial w}{\partial y}\right)^2 \\ \frac{1}{2}\left(\frac{\partial u_0}{\partial y} + \frac{\partial v_0}{\partial x}\right) + \frac{1}{2}\frac{\partial w}{\partial x}\frac{\partial w}{\partial y} \end{Bmatrix} - z \begin{Bmatrix} \frac{\partial^2 w}{\partial x^2} \\ \frac{\partial^2 w}{\partial y^2} \\ \frac{\partial^2 w}{\partial x \partial y} \end{Bmatrix} \tag{7.3}$$

which is valid for the whole composite (that is, $-h_\mathrm{p}/2 - h_\mathrm{e} \leq z \leq h_\mathrm{p}/2$) and is simplified in notation as

$$\begin{Bmatrix} \epsilon_{xx} \\ \epsilon_{yy} \\ \epsilon_{xy} \end{Bmatrix} = \begin{Bmatrix} \epsilon^0_{xx} \\ \epsilon^0_{yy} \\ \epsilon^0_{xy} \end{Bmatrix} + z \begin{Bmatrix} k_x \\ k_y \\ k_{xy} \end{Bmatrix} \tag{7.4}$$

Next, we modify Equations (2.6) as

$$\begin{Bmatrix} N_{xx} \\ N_{yy} \\ N_{xy} \end{Bmatrix} = \int_{-\frac{h_\mathrm{p}}{2}-h_\mathrm{e}}^{\frac{h_\mathrm{p}}{2}} \begin{Bmatrix} \sigma_{xx} \\ \sigma_{yy} \\ \sigma_{xy} \end{Bmatrix} dz \tag{7.5}$$

and

$$\begin{Bmatrix} M_{xx} \\ M_{yy} \\ M_{xy} \end{Bmatrix} = \int_{-\frac{h_\mathrm{p}}{2}-h_\mathrm{e}}^{\frac{h_\mathrm{p}}{2}} \begin{Bmatrix} \sigma_{xx} \\ \sigma_{yy} \\ \sigma_{xy} \end{Bmatrix} z\, dz \tag{7.6}$$

to account for the finite plate thickness. We then let the vectors in Equations (7.1), (7.4), (7.5), and (7.6) be represented by bold letters and obtain

$$\boldsymbol{\sigma} = [Q]\boldsymbol{\epsilon} \tag{7.7a}$$

$$\boldsymbol{\epsilon} = \boldsymbol{\epsilon^0} + z\,\boldsymbol{k} \tag{7.7b}$$

$$\boldsymbol{N} = \int_{z_1}^{z_2} \boldsymbol{\sigma}\, dz \tag{7.7c}$$

$$\boldsymbol{M} = \int_{z_1}^{z_2} \boldsymbol{\sigma}\, z\, dz \tag{7.7d}$$

where $z_1 = -h_\mathrm{p}/2 - h_\mathrm{e}$ and $z_2 = h_\mathrm{p}/2$. Manipulation of Equations (7.7) yields

$$\begin{Bmatrix} \boldsymbol{N} \\ \boldsymbol{M} \end{Bmatrix} = \begin{bmatrix} [A] & [B] \\ [B] & [D] \end{bmatrix} \begin{Bmatrix} \boldsymbol{\epsilon^0} \\ \boldsymbol{k} \end{Bmatrix} \tag{7.8}$$

where

$$([A],[B],[D]) = \int_{z_1}^{z_2} [Q]\left(1, z, z^2\right) dz \tag{7.9}$$

7.2.3 Equation of Motion

The equations of motion, Equations (2.17), are still valid for the non-composite regime but are not valid for the composite regime of the CMUT because of the asymmetry across the midplane, as seen in Figure 7.1. If the electrode had been included in the formulation, Equations (2.17) and (2.18) would have been

$$\frac{\partial N_{xx}}{\partial x} + \frac{\partial N_{xy}}{\partial y} - I_{\text{eff}}\ddot{u}_0 + I_1\frac{\partial^2}{\partial t^2}\frac{\partial w}{\partial x} + Q_x = 0 \quad \text{in } \Omega \tag{7.10a}$$

$$\frac{\partial N_{xy}}{\partial x} + \frac{\partial N_{yy}}{\partial y} - I_{\text{eff}}\ddot{v}_0 + I_1\frac{\partial^2}{\partial t^2}\frac{\partial w}{\partial y} + Q_y = 0 \quad \text{in } \Omega \tag{7.10b}$$

$$\begin{aligned}&\frac{\partial}{\partial x}\left(N_{xx}\frac{\partial w}{\partial x}\right) + \frac{\partial}{\partial y}\left(N_{xy}\frac{\partial w}{\partial x}\right) + \frac{\partial}{\partial x}\left(N_{xy}\frac{\partial w}{\partial y}\right) + \frac{\partial}{\partial y}\left(N_{yy}\frac{\partial w}{\partial y}\right)\\ &\quad + \frac{\partial^2 M_{xx}}{\partial x^2} + 2\frac{\partial^2 M_{xy}}{\partial x \partial y} + \frac{\partial^2 M_{yy}}{\partial y^2} - I_{\text{eff}}\ddot{w} - I_1\frac{\partial^2}{\partial t^2}\left(\frac{\partial u_0}{\partial x} + \frac{\partial v_0}{\partial y}\right)\\ &\quad + I_2\frac{\partial^2}{\partial t^2}\left(\frac{\partial^2 w}{\partial x^2} + \frac{\partial^2 w}{\partial y^2}\right) + Q_z + \left(\frac{\partial M_x}{\partial x} + \frac{\partial M_y}{\partial y}\right) = 0 \quad \text{in } \Omega\end{aligned} \tag{7.10c}$$

and

$$(N_{xx}, N_{xy})\cdot\mathbf{n} = Q_x^S \quad \text{or} \quad \delta u_0 = 0 \quad \text{on } S \tag{7.11a}$$

$$(N_{xy}, N_{yy})\cdot\mathbf{n} = Q_y^S \quad \text{or} \quad \delta v_0 = 0 \quad \text{on } S \tag{7.11b}$$

$$\begin{aligned}&\left(N_{xx}\frac{\partial w}{\partial x} + N_{xy}\frac{\partial w}{\partial y} + \frac{\partial M_{xx}}{\partial x} + \frac{\partial M_{xy}}{\partial y} + M_x - I_1\ddot{u}_0 + I_2\frac{\partial \ddot{w}}{\partial x},\right.\\ &\left.\quad N_{xy}\frac{\partial w}{\partial x} + N_{yy}\frac{\partial w}{\partial y} + \frac{\partial M_{xy}}{\partial x} + \frac{\partial M_{yy}}{\partial y} + M_y - I_1\ddot{v}_0 + I_2\frac{\partial \ddot{w}}{\partial y}\right)\cdot\mathbf{n} = Q_z^S\end{aligned}$$

$$\text{or} \quad \delta w = 0 \quad \text{on } S \tag{7.11c}$$

$$(M_{xx}, M_{xy})\cdot\mathbf{n} = M_x^S \quad \text{or} \quad \delta\frac{\partial w}{\partial x} = 0 \quad \text{on } S \tag{7.11d}$$

$$(M_{xy}, M_{yy})\cdot\mathbf{n} = M_y^S \quad \text{or} \quad \delta\frac{\partial w}{\partial y} = 0 \quad \text{on } S \tag{7.11e}$$

where the CMUT density ρ is a function of z, $I_{\text{eff}} = \int_{z_1}^{z_2}\rho(z)\,dz = \rho_{\text{p}}h_{\text{p}} + \rho_{\text{e}}h_{\text{e}}$ is the composite mass per area, and

$$(I_1, I_2) = \int_{z_1}^{z_2}\rho(z)\left(z, z^2\right)dz \tag{7.12}$$

Therefore, terms with I_1 appear in the equations of motion and boundary conditions when the electrode is taken into account. However, we neglect these terms in addition to those already neglected in the previous formulation, which means that Equations (7.10a) and (7.10b) are identical to the first two approximate equations of motion, Equations (2.22), for motion in the x-y plane. Consequently, a stress function is used again to solve Equations (2.22). We introduce an Airy stress function Φ associated with the deformation that satisfies these two equations by letting

$$\boldsymbol{N} = \begin{Bmatrix} N_{xx} \\ N_{yy} \\ N_{xy} \end{Bmatrix} = \begin{Bmatrix} \frac{\partial^2 \Phi}{\partial y^2} \\ \frac{\partial^2 \Phi}{\partial x^2} \\ -\frac{\partial^2 \Phi}{\partial x \partial y} \end{Bmatrix} \tag{7.13}$$

The only equation of motion left to satisfy is Equation (7.10c). For negligible rotary inertia terms and in-plane volumetric forces, Equation (7.10c) becomes

$$\begin{aligned} \frac{\partial}{\partial x}\left(N_{xx}\frac{\partial w}{\partial x}\right) + \frac{\partial}{\partial y}\left(N_{xy}\frac{\partial w}{\partial x}\right) + \frac{\partial}{\partial x}\left(N_{xy}\frac{\partial w}{\partial y}\right) + \frac{\partial}{\partial y}\left(N_{yy}\frac{\partial w}{\partial y}\right) \\ + \frac{\partial^2 M_{xx}}{\partial x^2} + 2\frac{\partial^2 M_{xy}}{\partial x \partial y} + \frac{\partial^2 M_{yy}}{\partial y^2} + Q_z = I_{\text{eff}}\ddot{w} \end{aligned} \tag{7.14}$$

Through manipulation of Equation (7.8), we find out that

$$\begin{Bmatrix} \boldsymbol{\epsilon^0} \\ \boldsymbol{M} \end{Bmatrix} = \begin{bmatrix} [A^*] & [B^*] \\ -[B^*]^{\mathrm{T}} & [D^*] \end{bmatrix} \begin{Bmatrix} \boldsymbol{N} \\ \boldsymbol{k} \end{Bmatrix} \tag{7.15}$$

where

$$[A^*] = [A]^{-1} \tag{7.16a}$$

$$[B^*] = -[A]^{-1}[B] \tag{7.16b}$$

$$[D^*] = [D] - [B][A]^{-1}[B] \tag{7.16c}$$

Before substituting for $\boldsymbol{M}$ from Equation (7.15) into Equation (7.14), we evaluate the inte-

grals in Equation (7.9) and rewrite the matrices $[A]$, $[B]$, and $[D]$ as

$$[A] = \begin{bmatrix} A_{11} & A_{12} & 0 \\ A_{12} & A_{11} & 0 \\ 0 & 0 & A_{11} - A_{12} \end{bmatrix} \tag{7.17a}$$

$$[B] = \begin{bmatrix} B_{11} & B_{12} & 0 \\ B_{12} & B_{11} & 0 \\ 0 & 0 & B_{11} - B_{12} \end{bmatrix} \tag{7.17b}$$

$$[D] = \begin{bmatrix} D_{11} & D_{12} & 0 \\ D_{12} & D_{11} & 0 \\ 0 & 0 & D_{11} - D_{12} \end{bmatrix} \tag{7.17c}$$

where

$$A_{11} = \frac{E_\mathrm{p} h_\mathrm{p}}{1 - \nu_\mathrm{p}^2} + \frac{E_\mathrm{e} h_\mathrm{e}}{1 - \nu_\mathrm{e}^2} \tag{7.18a}$$

$$A_{12} = \frac{E_\mathrm{p} h_\mathrm{p} \nu_\mathrm{p}}{1 - \nu_\mathrm{p}^2} + \frac{E_\mathrm{e} h_\mathrm{e} \nu_\mathrm{e}}{1 - \nu_\mathrm{e}^2} \tag{7.18b}$$

$$B_{11} = -\frac{E_\mathrm{e} h_\mathrm{e} (h_\mathrm{p} + h_\mathrm{e})}{2(1 - \nu_\mathrm{e}^2)} \tag{7.18c}$$

$$B_{12} = -\frac{E_\mathrm{e} h_\mathrm{e} (h_\mathrm{p} + h_\mathrm{e}) \nu_\mathrm{e}}{2(1 - \nu_\mathrm{e}^2)} = B_{11} \nu_\mathrm{e} \tag{7.18d}$$

$$D_{11} = \frac{E_\mathrm{p} h_\mathrm{p}^3}{12(1 - \nu_\mathrm{p}^2)} + \frac{E_\mathrm{e} h_\mathrm{e} (4h_\mathrm{e}^2 + 6h_\mathrm{e} h_\mathrm{p} + 3h_\mathrm{p}^2)}{12(1 - \nu_\mathrm{e}^2)} \tag{7.18e}$$

$$D_{12} = \frac{E_\mathrm{p} h_\mathrm{p}^3 \nu_\mathrm{p}}{12(1 - \nu_\mathrm{p}^2)} + \frac{E_\mathrm{e} h_\mathrm{e} (4h_\mathrm{e}^2 + 6h_\mathrm{e} h_\mathrm{p} + 3h_\mathrm{p}^2) \nu_\mathrm{e}}{12(1 - \nu_\mathrm{e}^2)} \tag{7.18f}$$

We then substitute for $\boldsymbol{M}$ from Equation (7.15) into Equation (7.14), use all necessary definitions, and obtain

$$I_\mathrm{eff} \ddot{w} + D_\mathrm{eff} \nabla^4 w = \left(\frac{\partial^2 \Phi}{\partial y^2} \frac{\partial^2 w}{\partial x^2} - 2 \frac{\partial^2 \Phi}{\partial x \partial y} \frac{\partial^2 w}{\partial x \partial y} + \frac{\partial^2 \Phi}{\partial x^2} \frac{\partial^2 w}{\partial y^2} \right) - \frac{F_2}{F_1} \nabla^4 \Phi + Q_z \tag{7.19}$$

where

$$D_\mathrm{eff} = D_{11} - \frac{A_{11} B_{11}^2 - 2 A_{12} B_{11} B_{12} + A_{11} B_{12}^2}{A_{11}^2 - A_{12}^2} \tag{7.20}$$

is the composite plate flexural rigidity and

$$F_1 = A_{11} - \frac{A_{12}^2}{A_{11}} \tag{7.21a}$$

$$F_2 = \frac{A_{12}B_{11}}{A_{11}} - B_{12} \tag{7.21b}$$

Finally, we add a linear damping term to Equation (7.19) with the same coefficient as that for the non-composite part of the CMUT and let Q_z be the external forces due to a pressure difference F and the electrostatic field to obtain

$$\begin{aligned} I_{\text{eff}}\frac{\partial^2 w}{\partial t^2} + 2\,c\frac{\partial w}{\partial t} + D_{\text{eff}}\nabla^4 w = &\left(\frac{\partial^2\Phi}{\partial y^2}\frac{\partial^2 w}{\partial x^2} - 2\frac{\partial^2\Phi}{\partial x\partial y}\frac{\partial^2 w}{\partial x\partial y} + \frac{\partial^2\Phi}{\partial x^2}\frac{\partial^2 w}{\partial y^2}\right) \\ &- \frac{F_2}{F_1}\nabla^4\Phi + F(x,y,t) + \frac{\epsilon_0 v^2(t)}{2(d-w)^2} \end{aligned} \tag{7.22}$$

7.2.4 Compatibility Equation

The compatibility equation (2.29) is valid for the non-composite part of the CMUT, but is not valid for the composite part. In contrast, Equation (2.27) is valid for the composite part of the CMUT and is restated here for convenience:

$$\frac{\partial^2 e_{xx}}{\partial y^2} + \frac{\partial^2 e_{yy}}{\partial x^2} - \frac{\partial^2 e_{xy}}{\partial x\partial y} = \left(\frac{\partial^2 w}{\partial x\partial y}\right)^2 - \frac{\partial^2 w}{\partial x^2}\frac{\partial^2 w}{\partial y^2} \tag{7.23}$$

where

$$e_{xx} = \epsilon_{xx}^0 = \frac{\partial u_0}{\partial x} + \frac{1}{2}\left(\frac{\partial w}{\partial x}\right)^2 \tag{7.24a}$$

$$e_{yy} = \epsilon_{yy}^0 = \frac{\partial v_0}{\partial y} + \frac{1}{2}\left(\frac{\partial w}{\partial y}\right)^2 \tag{7.24b}$$

$$e_{xy} = 2\,\epsilon_{xy}^0 = \frac{\partial u_0}{\partial y} + \frac{\partial v_0}{\partial x} + \frac{\partial w}{\partial x}\frac{\partial w}{\partial y} \tag{7.24c}$$

We substitute for $\boldsymbol{\epsilon^0}$ from Equation (7.15) into Equation (7.23), use all necessary definitions, and obtain

$$\nabla^4\Phi = F_1\left[\left(\frac{\partial^2 w}{\partial x\partial y}\right)^2 - \frac{\partial^2 w}{\partial x^2}\frac{\partial^2 w}{\partial y^2}\right] + F_2\nabla^4 w \tag{7.25}$$

which is the compatibility equation for the composite part of the CMUT.

7.2.5 Nondimensional Forms

Therefore, the dimensional equations that govern the composite part of the CMUT are Equations (7.22) and (7.25), which are

$$I_{\text{eff}}\frac{\partial^2\hat{w}}{\partial\hat{t}^2} + 2\,\hat{c}\frac{\partial\hat{w}}{\partial\hat{t}} + D_{\text{eff}}\hat{\nabla}^4\hat{w} = \left(\frac{\partial^2\hat{\Phi}}{\partial\hat{y}^2}\frac{\partial^2\hat{w}}{\partial\hat{x}^2} - 2\frac{\partial^2\hat{\Phi}}{\partial\hat{x}\partial\hat{y}}\frac{\partial^2\hat{w}}{\partial\hat{x}\partial\hat{y}} + \frac{\partial^2\hat{\Phi}}{\partial\hat{x}^2}\frac{\partial^2\hat{w}}{\partial\hat{y}^2}\right) - \frac{F_2}{F_1}\hat{\nabla}^4\hat{\Phi} + \hat{F}(\hat{x},\hat{y},\hat{t}) + \frac{\epsilon_0\hat{v}^2(\hat{t})}{2(d-\hat{w})^2} \tag{7.26a}$$

$$\hat{\nabla}^4\hat{\Phi} = F_1\left[\left(\frac{\partial^2\hat{w}}{\partial\hat{x}\partial\hat{y}}\right)^2 - \frac{\partial^2\hat{w}}{\partial\hat{x}^2}\frac{\partial^2\hat{w}}{\partial\hat{y}^2}\right] + F_2\hat{\nabla}^4\hat{w} \tag{7.26b}$$

respectively, in which the hat denotes a dimensional variable. Once again, we nondimensionalize these two equations according to Equations (3.2) and obtain

$$I_{\text{rel}}\frac{\partial^2 w}{\partial t^2} + 2\,c\frac{\partial w}{\partial t} + D_{\text{rel}}\nabla^4 w = \beta\left(\frac{\partial^2\Phi}{\partial y^2}\frac{\partial^2 w}{\partial x^2} - 2\frac{\partial^2\Phi}{\partial x\partial y}\frac{\partial^2 w}{\partial x\partial y} + \frac{\partial^2\Phi}{\partial x^2}\frac{\partial^2 w}{\partial y^2}\right) - \gamma_1\beta\nabla^4\Phi + F(x,y,t) + \frac{v^2(t)}{(1-w)^2} \tag{7.27a}$$

$$\nabla^4\Phi = \gamma_2\left[\left(\frac{\partial^2 w}{\partial x\partial y}\right)^2 - \frac{\partial^2 w}{\partial x^2}\frac{\partial^2 w}{\partial y^2} + \gamma_1\nabla^4 w\right] \tag{7.27b}$$

where

$$I_{\text{rel}} = \frac{I_{\text{eff}}}{I_0} \tag{7.28a}$$

$$D_{\text{rel}} = \frac{D_{\text{eff}}}{D} \tag{7.28b}$$

$$\gamma_1 = \frac{F_2}{F_1 d} \tag{7.28c}$$

$$\gamma_2 = \frac{F_1}{Eh} \tag{7.28d}$$

7.3 Problem Formulation for Composite Model

7.3.1 Governing Equations in Composite Regime

For simplicity, we let the non-composite and composite regimes be $\Re_{\text{nc}} = \Re_{\text{nc}}^{\text{in}} \cup \Re_{\text{nc}}^{\text{out}}$ and $\Re_{\text{c}} = (r_{\text{in}},\, r_{\text{out}})$, respectively, where $\Re_{\text{nc}}^{\text{in}} = (0,\, r_{\text{in}})$ and $\Re_{\text{nc}}^{\text{out}} = (r_{\text{out}},\, 1)$. Thus, the axisymmetric

forms of Equations (7.27) are

$$I_{\text{rel}}\frac{\partial^2 w}{\partial t^2} + 2\,c\frac{\partial w}{\partial t} + D_{\text{rel}}\nabla^4 w = \frac{\beta}{r}\frac{\partial}{\partial r}\left(\frac{\partial w}{\partial r}\frac{\partial \Phi}{\partial r}\right) - \gamma_1\beta\nabla^4\Phi + F(r,t) + \frac{v^2(t)}{(1-w)^2} \tag{7.29a}$$

$$\nabla^4\Phi = \gamma_2\left(-\frac{1}{r}\frac{\partial^2 w}{\partial r^2}\frac{\partial w}{\partial r} + \gamma_1\nabla^4 w\right) \tag{7.29b}$$

which apply for only $r \in \Re_{\text{c}}$. Equation (7.29b) can be integrated for axisymmetric motions to obtain

$$\Theta = r\frac{\partial}{\partial r}\left[\frac{1}{r}\frac{\partial}{\partial r}\left(r\frac{\partial \Phi}{\partial r}\right)\right] = \gamma_2\left\{-\frac{1}{2}\left(\frac{\partial w}{\partial r}\right)^2 + \gamma_1 r\frac{\partial}{\partial r}\left[\frac{1}{r}\frac{\partial}{\partial r}\left(r\frac{\partial w}{\partial r}\right)\right]\right\} + f_{\text{c}}(t) \;\; \forall \;\; r \in \Re_{\text{c}} \tag{7.30}$$

which is similar to Equation (6.15) for the non-composite part of the CMUT, except for the time-dependent function of integration.

7.3.2 Governing Equations in Non-Composite Regime

If we had used Equation (7.13) instead of Equations (2.23) to derive the governing equations for the non-composite part of the CMUT, Equations (3.3) and (3.4) would have been replaced by

$$\frac{\partial^2 w}{\partial t^2} + 2c\frac{\partial w}{\partial t} + \nabla^4 w = \frac{\beta}{r}\frac{\partial}{\partial r}\left(\frac{\partial w}{\partial r}\frac{\partial \Phi}{\partial r}\right) + F(r,t) \tag{7.31a}$$

$$\nabla^4\Phi = -\frac{1}{r}\frac{\partial^2 w}{\partial r^2}\frac{\partial w}{\partial r} \tag{7.31b}$$

respectively, which apply for only $r \in \Re_{\text{nc}}$. We note that the electric forcing term has been removed because the electrode does not exist in the non-composite regime of the CMUT. Furthermore, Equation (7.31b) can be integrated for axisymmetric motions to obtain

$$\Theta = r\frac{\partial}{\partial r}\left[\frac{1}{r}\frac{\partial}{\partial r}\left(r\frac{\partial \Phi}{\partial r}\right)\right] = -\frac{1}{2}\left(\frac{\partial w}{\partial r}\right)^2 + f_{\text{nc}}^{\text{in}}(t) \quad \forall \;\; r \in \Re_{\text{nc}}^{\text{in}} \tag{7.32a}$$

$$\Theta = r\frac{\partial}{\partial r}\left[\frac{1}{r}\frac{\partial}{\partial r}\left(r\frac{\partial \Phi}{\partial r}\right)\right] = -\frac{1}{2}\left(\frac{\partial w}{\partial r}\right)^2 + f_{\text{nc}}^{\text{out}}(t) \;\; \forall \;\; r \in \Re_{\text{nc}}^{\text{out}} \tag{7.32b}$$

Therefore, the composite equations, Equations (7.29), differ from the non-composite equations in that Equations (7.29) have modified mass and stiffness terms along with extra coupling from additional biharmonic terms.

7.3.3 Matching Conditions

Solution of Equations (7.29) and (7.31) requires matching conditions between the composite and non-composite regimes at the interfaces $r = r_{\text{in}}$ and $r = r_{\text{out}}$. At each matching boundary, we let

$$w^- = w^+ \tag{7.33a}$$

$$\left(\frac{\partial w}{\partial r}\right)^- = \left(\frac{\partial w}{\partial r}\right)^+ \tag{7.33b}$$

$$(N_{rr})^- = (N_{rr})^+ \tag{7.33c}$$

$$(M_{rr})^- = (M_{rr})^+ \tag{7.33d}$$

$$(Q_{\text{net}})^- = (Q_{\text{net}})^+ \tag{7.33e}$$

$$\Theta^- = \Theta^+ \tag{7.33f}$$

where the 'minus' and 'plus' superscripts denote variables to the left and right, respectively, of the matching boundary radius value, and

$$Q_{\text{net}} = \frac{\partial M_{rr}}{\partial r} + \frac{M_{rr} - M_{\theta\theta}}{r} + N_{rr}\frac{\partial w}{\partial r} \tag{7.34}$$

is the net vertical shear force per length for axisymmetric motion (Nayfeh and Pai, 2004). Equations (7.33a) and (7.33b) ensure the continuity of displacements and slopes from one regime to another, while Equations (7.33c)-(7.33e) ensure the continuity of forces and moments across each matching boundary, even though the stresses may be discontinuous. Finally, Equation (7.33f) ensures continuity in the integrated compatibility function defined in Equations (7.30) and (7.32).

To evaluate the matching conditions, we need expressions for N_{rr}, M_{rr}, and $M_{\theta\theta}$ for each regime of the CMUT. For the non-composite regime,

$$N_{rr} = \frac{\beta}{r}\left(\frac{\partial \Phi}{\partial r} + \frac{1}{r}\frac{\partial^2 \Phi}{\partial \theta^2}\right) \tag{7.35a}$$

$$M_{rr} = -\left[\frac{\partial^2 w}{\partial r^2} + \frac{\nu}{r}\left(\frac{\partial w}{\partial r} + \frac{1}{r}\frac{\partial^2 w}{\partial \theta^2}\right)\right] \tag{7.35b}$$

$$M_{\theta\theta} = -\left[\nu\frac{\partial^2 w}{\partial r^2} + \frac{1}{r}\left(\frac{\partial w}{\partial r} + \frac{1}{r}\frac{\partial^2 w}{\partial \theta^2}\right)\right] \tag{7.35c}$$

For the composite regime, Equation (7.35a) applies but Equations (7.35b) and (7.35c) do not. Instead, M_{rr} and $M_{\theta\theta}$ are found from Equation (7.15) through use of polar transformations. Accordingly, the dimensional moments $\hat{M}_{rr}$ and $\hat{M}_{\theta\theta}$ are

$$\hat{M}_{rr} = -D_{\text{eff}}\left[\frac{\partial^2\hat{w}}{\partial\hat{r}^2} + \frac{\nu_{\text{eff}}}{\hat{r}}\left(\frac{\partial\hat{w}}{\partial\hat{r}} + \frac{1}{\hat{r}}\frac{\partial^2\hat{w}}{\partial\theta^2}\right)\right] + \frac{F_3}{\hat{r}}\left(\frac{\partial\hat{\Phi}}{\partial\hat{r}} + \frac{1}{\hat{r}}\frac{\partial^2\hat{\Phi}}{\partial\theta^2}\right) - \frac{F_2}{F_1}\frac{\partial^2\hat{\Phi}}{\partial\hat{r}^2} \tag{7.36a}$$

$$\hat{M}_{\theta\theta} = -D_{\text{eff}}\left[\nu_{\text{eff}}\frac{\partial^2\hat{w}}{\partial\hat{r}^2} + \frac{1}{\hat{r}}\left(\frac{\partial\hat{w}}{\partial\hat{r}} + \frac{1}{\hat{r}}\frac{\partial^2\hat{w}}{\partial\theta^2}\right)\right] - \frac{F_2}{F_1}\frac{1}{\hat{r}}\left(\frac{\partial\hat{\Phi}}{\partial\hat{r}} + \frac{1}{\hat{r}}\frac{\partial^2\hat{\Phi}}{\partial\theta^2}\right) + F_3\frac{\partial^2\hat{\Phi}}{\partial\hat{r}^2} \tag{7.36b}$$

where D_{eff} is defined in Equation (7.20), F_1 and F_2 are defined in Equations (7.21), and

$$\nu_{\text{eff}} = \frac{A_{12}(B_{11}^2 + B_{12}^2) - A_{12}^2 D_{12} + A_{11}(-2B_{11}B_{12} + A_{11}D_{12})}{-A_{11}(B_{11}^2 + B_{12}^2) + A_{11}^2 D_{11} + A_{12}(2B_{11}B_{12} - A_{12}D_{11})} \tag{7.37a}$$

$$F_3 = \frac{A_{11}B_{11} - A_{12}B_{12}}{A_{11}^2 - A_{12}^2} \tag{7.37b}$$

Finally, we nondimensionalize Equations (7.36) to obtain

$$N_{rr} = \frac{\beta}{r}\left(\frac{\partial\Phi}{\partial r} + \frac{1}{r}\frac{\partial^2\Phi}{\partial\theta^2}\right) \tag{7.38a}$$

$$M_{rr} = -D_{\text{rel}}\left[\frac{\partial^2 w}{\partial r^2} + \frac{\nu_{\text{eff}}}{r}\left(\frac{\partial w}{\partial r} + \frac{1}{r}\frac{\partial^2 w}{\partial\theta^2}\right)\right] + h_{\text{eff}}N_{rr} - \gamma_1\beta\frac{\partial^2\Phi}{\partial r^2} \tag{7.38b}$$

$$M_{\theta\theta} = -D_{\text{rel}}\left[\nu_{\text{eff}}\frac{\partial^2 w}{\partial r^2} + \frac{1}{r}\left(\frac{\partial w}{\partial r} + \frac{1}{r}\frac{\partial^2 w}{\partial\theta^2}\right)\right] - \gamma_1 N_{rr} + h_{\text{eff}}\beta\frac{\partial^2\Phi}{\partial r^2} \tag{7.38c}$$

for the composite regime, where γ_1 is defined in Equation (7.28c) and h_{eff} is defined by

$$h_{\text{eff}} = \frac{F_3}{d} \tag{7.39}$$

7.3.4 Boundary Conditions

Solution of Equations (7.29) and (7.31) also requires boundary conditions at $r = 0$ and $r = 1$. Equations (6.4) were used previously for the updated non-composite model. For the composite model, we let the axisymmetric boundary conditions be

$$w = 0 \quad \text{at } r = 1 \tag{7.40a}$$

$$\frac{\partial w}{\partial r} = -K_\tau - K_2\frac{\partial^2 w}{\partial r^2} \quad \text{at } r = 1 \tag{7.40b}$$

$$N_{rr} = \tau \quad \text{at } r = 1 \tag{7.40c}$$

$$w < \infty \text{ and } \Phi < \infty \quad \text{at } r = 0 \tag{7.40d}$$

7.3.5 Problem Formulation

For convenience, we gather the composite model equations for axisymmetric motion in this section. First, the equation of motion is

$$I_{\text{rel}}\frac{\partial^2 w}{\partial t^2} + 2\,c\frac{\partial w}{\partial t} + D_{\text{rel}}\nabla^4 w = \frac{\beta}{r}\frac{\partial}{\partial r}\left(\frac{\partial w}{\partial r}\frac{\partial \Phi}{\partial r}\right) + F(r,t) \\ -\gamma_1\beta\nabla^4\Phi + \frac{v^2(t)}{(1-w)^2} \quad \forall \; r \in \Re_{\text{c}} \tag{7.41a}$$

$$\text{and} \quad \frac{\partial^2 w}{\partial t^2} + 2c\frac{\partial w}{\partial t} + \nabla^4 w = \frac{\beta}{r}\frac{\partial}{\partial r}\left(\frac{\partial w}{\partial r}\frac{\partial \Phi}{\partial r}\right) + F(r,t) \quad \forall \; r \in \Re_{\text{nc}} \tag{7.41b}$$

and the compatibility equation is

$$\nabla^4\Phi = \gamma_2\left(-\frac{1}{r}\frac{\partial^2 w}{\partial r^2}\frac{\partial w}{\partial r} + \gamma_1\nabla^4 w\right) \quad \forall \; r \in \Re_{\text{c}} \tag{7.42a}$$

$$\text{and} \quad \nabla^4\Phi = -\frac{1}{r}\frac{\partial^2 w}{\partial r^2}\frac{\partial w}{\partial r} \quad \forall \; r \in \Re_{\text{nc}} \tag{7.42b}$$

or its integrated form

$$\Theta = \gamma_2\left\{-\frac{1}{2}\left(\frac{\partial w}{\partial r}\right)^2 + \gamma_1 r\frac{\partial}{\partial r}\left[\frac{1}{r}\frac{\partial}{\partial r}\left(r\frac{\partial w}{\partial r}\right)\right]\right\} + f_{\text{c}}(t) \quad \forall \; r \in \Re_{\text{c}} \tag{7.43a}$$

$$\Theta = -\frac{1}{2}\left(\frac{\partial w}{\partial r}\right)^2 + f_{\text{nc}}^{\text{in}}(t) \quad \forall \; r \in \Re_{\text{nc}}^{\text{in}} \tag{7.43b}$$

$$\text{and} \quad \Theta = -\frac{1}{2}\left(\frac{\partial w}{\partial r}\right)^2 + f_{\text{nc}}^{\text{out}}(t) \quad \forall \; r \in \Re_{\text{nc}}^{\text{out}} \tag{7.43c}$$

where

$$\Theta = r\frac{\partial}{\partial r}\left[\frac{1}{r}\frac{\partial}{\partial r}\left(r\frac{\partial \Phi}{\partial r}\right)\right] \tag{7.44}$$

The matching equations at the interfaces $r = r_{\text{in}}$ and $r = r_{\text{out}}$ are

$$w^- = w^+ \tag{7.45a}$$

$$\left(\frac{\partial w}{\partial r}\right)^- = \left(\frac{\partial w}{\partial r}\right)^+ \tag{7.45b}$$

$$(N_{rr})^- = (N_{rr})^+ \tag{7.45c}$$

$$(M_{rr})^- = (M_{rr})^+ \tag{7.45d}$$

$$(Q_{\text{net}})^- = (Q_{\text{net}})^+ \tag{7.45e}$$

$$\Theta^- = \Theta^+ \tag{7.45f}$$

where

$$Q_{\text{net}} = \frac{\partial M_{rr}}{\partial r} + \frac{M_{rr} - M_{\theta\theta}}{r} + N_{rr}\frac{\partial w}{\partial r} \qquad \forall\ r \in (0,1) \tag{7.46a}$$

$$N_{rr} = \frac{\beta}{r}\frac{\partial \Phi}{\partial r} \qquad \forall\ r \in (0,1) \tag{7.46b}$$

$$M_{rr} = -D_{\text{rel}}\left(\frac{\partial^2 w}{\partial r^2} + \frac{\nu_{\text{eff}}}{r}\frac{\partial w}{\partial r}\right) + h_{\text{eff}}N_{rr} - \gamma_1\beta\frac{\partial^2 \Phi}{\partial r^2} \qquad \forall\ r \in \Re_{\text{c}} \tag{7.46c}$$

$$M_{rr} = -\left(\frac{\partial^2 w}{\partial r^2} + \frac{\nu}{r}\frac{\partial w}{\partial r}\right) \qquad \forall\ r \in \Re_{\text{nc}} \tag{7.46d}$$

$$M_{\theta\theta} = -D_{\text{rel}}\left(\nu_{\text{eff}}\frac{\partial^2 w}{\partial r^2} + \frac{1}{r}\frac{\partial w}{\partial r}\right) - \gamma_1 N_{rr} + h_{\text{eff}}\beta\frac{\partial^2 \Phi}{\partial r^2} \qquad \forall\ r \in \Re_{\text{c}} \tag{7.46e}$$

$$M_{\theta\theta} = -\left(\nu\frac{\partial^2 w}{\partial r^2} + \frac{1}{r}\frac{\partial w}{\partial r}\right) \qquad \forall\ r \in \Re_{\text{nc}} \tag{7.46f}$$

for axisymmetric motions. Finally, the boundary conditions are

$$w = 0 \qquad \text{at } r = 1 \tag{7.47a}$$

$$\frac{\partial w}{\partial r} = -K_\tau - K_2\frac{\partial^2 w}{\partial r^2} \qquad \text{at } r = 1 \tag{7.47b}$$

$$N_{rr} = \tau \qquad \text{at } r = 1 \tag{7.47c}$$

$$w < \infty \text{ and } \Phi < \infty \qquad \text{at } r = 0 \tag{7.47d}$$

Thus, the equation of motion, Equations (7.41), will be solved in conjunction with the compatibility equation, Equations (7.42) or Equations (7.43), subject to Equations (7.45) for matching at $r = r_{\text{in}}$ and $r = r_{\text{out}}$ and Equations (7.47) for boundary conditions.

7.4 Galerkin Approach for Axisymmetric Motion

7.4.1 Approximate Solutions

Once again, we approximate $w(r,t)$ and $\Phi(r,t)$ as

$$w(r,t) = w_s(r) + \sum_{m=1}^{N}\eta_m(t)\phi_m(r) \tag{7.48a}$$

$$\Phi(r,t) = \Phi_s(r) + \sum_{m=1}^{N}\eta_m(t)\Gamma_m(r) + \sum_{m,n=1}^{N}\eta_m(t)\eta_n(t)\psi_{mn}(r) \tag{7.48b}$$

where $\eta_m(t)$ is the mth generalized coordinate for the mth shape function.

7.4.2 Solution of Static Terms

We let $w_s(r)$ and $\Phi_s(r)$ solve

$$D_{\text{rel}}\nabla^4 w_s = -\gamma_1\beta\nabla^4\Phi_s \;\; \forall \;\; r \in \Re_{\text{c}} \tag{7.49a}$$

$$\text{and} \;\; \nabla^4 w_s = 0 \qquad\qquad \forall \;\; r \in \Re_{\text{nc}} \tag{7.49b}$$

with the compatibility equation, which is

$$\nabla^4\Phi_s = \gamma_2\left(-\frac{1}{r}w_s''w_s' + \gamma_1\nabla^4 w_s\right) \;\; \forall \;\; r \in \Re_{\text{c}} \tag{7.50a}$$

$$\text{and} \;\; \nabla^4\Phi_s = -\frac{1}{r}w_s''w_s' \qquad\qquad \forall \;\; r \in \Re_{\text{nc}} \tag{7.50b}$$

The functions $w_s(r)$ and $\Phi_s(r)$ also satisfy the matching equations, Equations (7.45), at $r = r_{\text{in}}$ and $r = r_{\text{out}}$ and the boundary conditions from Equations (7.47), which are

$$w_s = 0 \qquad \text{at} \;\; r = 1 \tag{7.51a}$$

$$w_s' = -K_\tau - K_2 w_s'' \qquad \text{at} \;\; r = 1 \tag{7.51b}$$

$$\beta\Phi_s' = \tau \qquad \text{at} \;\; r = 1 \tag{7.51c}$$

$$w_s < \infty \;\; \text{and} \;\; \Phi_s < \infty \qquad \text{at} \;\; r = 0 \tag{7.51d}$$

To solve for $w_s(r)$ and $\Phi_s(r)$, we find their general forms for each regime of the CMUT.

First, when Equation (7.50a) is substituted into Equation (7.49a), we obtain

$$\nabla^4 w_s = \frac{K_4}{r}w_s''w_s' \;\; \forall \;\; r \in \Re_{\text{c}} \tag{7.52}$$

where the parameter K_4 is

$$K_4 = \frac{\gamma_1\gamma_2\beta}{D_{\text{rel}} + \gamma_1^2\gamma_2\beta} \tag{7.53}$$

The general series solution of Equation (7.52) is

$$w_s(r) = \sum_{i=0}^{\infty} c_i r^i \;\; \forall \;\; r \in \Re_{\text{c}} \tag{7.54}$$

where

$$c_i = \begin{cases} 0 & , \;\; i = 1, 3, 5 \ldots \\ d_i K_4^{(i/2-1)} c_2^{i/2} & , \;\; i = 4, 6, 8 \ldots \end{cases} \tag{7.55a}$$

$$d_i = \begin{cases} c_2 & , \;\; i = 2 \\ \sum_{j=1}^{i-1} \frac{j(j-1)(i-j)d_j d_{i-j}}{i^2(i-2)^2} & , \;\; i \neq 2 \end{cases} \tag{7.55b}$$

which yields

$$w_s = c_0 + c_2 r^2 + \frac{K_4}{16} c_2^2 r^4 + \frac{K_4^2}{288} c_2^3 r^6 + \frac{7K_4^3}{36864} c_2^4 r^8 + \cdots \tag{7.56}$$

Second, the general solution of Equation (7.49b) is

$$w_s = n_0 + n_2 r^2 + n_3 \ln r + n_4 r^2 \ln r \quad \forall \quad r \in \Re_{\text{nc}} \tag{7.57}$$

However, this general solution applies for the inner non-composite regime $\Re_{\text{nc}}^{\text{in}}$ and the outer non-composite regime $\Re_{\text{nc}}^{\text{out}}$. Accordingly, we let

$$w_s = n_0^{\text{in}} + n_2^{\text{in}} r^2 + n_3^{\text{in}} \ln r + n_4^{\text{in}} r^2 \ln r \qquad \forall \quad r \in \Re_{\text{nc}}^{\text{in}} \tag{7.58a}$$

$$w_s = n_0^{\text{out}} + n_2^{\text{out}} r^2 + n_3^{\text{out}} \ln r + n_4^{\text{out}} r^2 \ln r \quad \forall \quad r \in \Re_{\text{nc}}^{\text{out}} \tag{7.58b}$$

Thus, only two parameters (c_0 and c_2) need to be solved for the composite regime, while eight parameters need to be solved, in general, for the non-composite regime. However, if there is no inner radius, then there are only four parameters for the non-composite regime.

We also need the general expression for Φ_s'. First, we substitute Equation (7.52) into Equation (7.50a) to obtain

$$\nabla^4 \Phi_s = -\frac{K_5}{r} w_s'' w_s' \quad \forall \quad r \in \Re_{\text{c}} \tag{7.59}$$

where the parameter K_5 is

$$K_5 = \frac{D_{\text{rel}} K_4}{\gamma_1 \beta} \tag{7.60}$$

Consequently, the compatibility equation for the composite regime has the same form as Equation (7.43b) for the non-composite regime; that is,

$$\Theta_s = r\Phi_s''' + \Phi_s'' - \frac{1}{r}\Phi_s' = g(r) \tag{7.61}$$

where

$$g(r) = \begin{cases} -\frac{K_5}{2}(w_s')^2 + f_{\text{c}} & \forall \quad r \in \Re_{\text{c}} \\ -\frac{1}{2}(w_s')^2 + f_{\text{nc}}^{\text{in}} & \forall \quad r \in \Re_{\text{nc}}^{\text{in}} \\ -\frac{1}{2}(w_s')^2 + f_{\text{nc}}^{\text{out}} & \forall \quad r \in \Re_{\text{nc}}^{\text{out}} \end{cases} \tag{7.62}$$

Once again, the method of variation of parameters is used to obtain Φ_s' as

$$\Phi_s' = \frac{r}{2}\int_0^r \frac{g(\xi)}{\xi}d\xi - \frac{1}{2r}\int_0^r g(\xi)\xi d\xi + p_1 r \tag{7.63}$$

where p_1 is a constant.

Substituting the general solutions given in Equations (7.54), (7.57), and (7.63) into the matching and boundary conditions, we determine the unknown parameter p_1 along with the other parameters. For example, Figure 7.2 shows the static deflection w_s for a CMUT made of a silicon nitride plate and an aluminum electrode (see material properties in Table 6.1) that has an applied boundary stress of 100 MPa. The electrode does not have a hole ($r_{\text{in}} = 0$), but its thickness h_{e} and outer radius r_{out} vary. Consequently, we solve for the nine parameters (c_0, c_2, n_0^{out}, n_2^{out}, n_3^{out}, n_4^{out}, p_1, f_{c} and $f_{\text{nc}}^{\text{out}}$) using nine matching and boundary conditions, because Equation (7.45c) is already satisfied by Equation (7.63). As seen in Figure 7.2, the static deflection w_s hardly changes with increasing stiffness and electrode size.

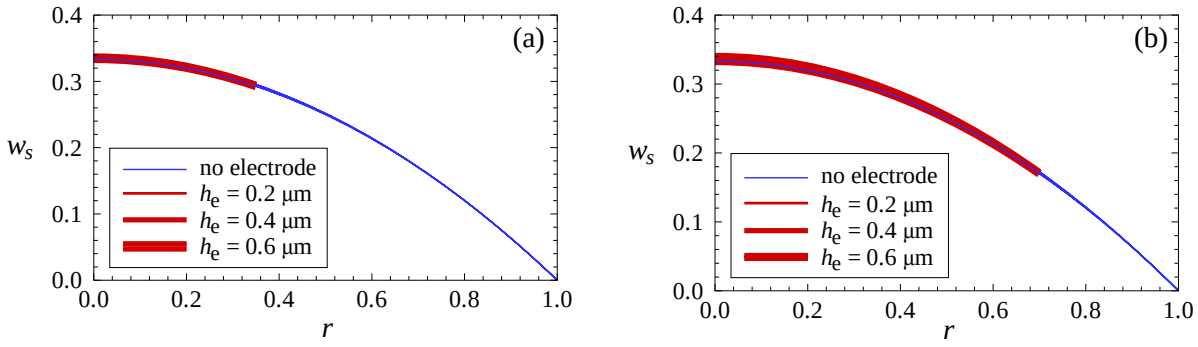

Figure 7.2: w_s versus r for various h_{e} with (a) $r_{\text{out}} = 0.35$ and (b) $r_{\text{out}} = 0.7$ with no inner electrode radius ($r_{\text{in}} = 0$). For all cases, $h_{\text{p}} = 1.0$ μm, $R = 50$ μm, $d = 1.05$ μm, $E_{\text{p}} = 320$ GPa, $E_{\text{e}} = 67.6$ GPa, $\nu_{\text{p}} = 0.263$, $\nu_{\text{e}} = 0.3555$, $\hat{\tau} = 100$ MPa, $K_\tau = 0.8$, and $K_2 = 0.2$.

7.4.3 Dynamic Solutions

We choose the shape functions $\phi_m(r)$ to be the axisymmetric modes of the linear undamped and unforced cases of Equations (7.41), which are

$$I_{\text{rel}}\ddot{w} + D_{\text{rel}}\nabla^4 w = 0 \quad \forall \quad r \in \Re_{\text{c}} \tag{7.64a}$$

$$\text{and} \quad \ddot{w} + \nabla^4 w = 0 \quad \forall \quad r \in \Re_{\text{nc}} \tag{7.64b}$$

Thus, $\phi_m(r)$ is the mth shape function that is a solution of

$$D_{\text{rel}}\nabla^4\phi_m - I_{\text{rel}}\Omega_m^2\phi_m = 0 \quad \forall \quad r \in \Re_{\text{c}} \tag{7.65a}$$

$$\text{and} \quad \nabla^4\phi_m - \Omega_m^2\phi_m = 0 \quad \forall \quad r \in \Re_{\text{nc}} \tag{7.65b}$$

where Ω_m is the natural frequency corresponding to $\phi_m(r)$. The solution of Equations (7.65) is

$$\phi_m = \begin{cases} c_1 J_0(r\Lambda\sqrt{\Omega_m}) + c_2 I_0(r\Lambda\sqrt{\Omega_m}) + c_3 Y_0(r\Lambda\sqrt{\Omega_m}) + c_4 K_0(r\Lambda\sqrt{\Omega_m}) \,, & r \in \Re_{\text{c}} \\ n_1 J_0(r\sqrt{\Omega_m}) + n_2 I_0(r\sqrt{\Omega_m}) + n_3 Y_0(r\sqrt{\Omega_m}) + n_4 K_0(r\sqrt{\Omega_m}) \quad , & r \in \Re_{\text{nc}}^{\text{in}} \\ n_5 J_0(r\sqrt{\Omega_m}) + n_6 I_0(r\sqrt{\Omega_m}) + n_7 Y_0(r\sqrt{\Omega_m}) + n_8 K_0(r\sqrt{\Omega_m}) \quad , & r \in \Re_{\text{nc}}^{\text{out}} \end{cases} \tag{7.66}$$

where $\Lambda = \sqrt[4]{\frac{I_{\text{rel}}}{D_{\text{rel}}}}$, J_0 and Y_0 are the respective zero-order Bessel functions of the first and second kinds, and I_0 and K_0 are the respective modified zero-order Bessel functions of the first and second kinds (O'Neil, 1995).

For the boundary conditions (7.47) to be satisfied by $w(r,t)$ given in Equation (7.48a) for arbitrary $\eta_m(t)$, each $\phi_m(r)$ must satisfy the boundary conditions

$$\phi_m = 0 \qquad \text{at} \quad r = 1 \tag{7.67a}$$

$$\phi_m' = -K_2\phi_m'' \qquad \text{at} \quad r = 1 \tag{7.67b}$$

$$\phi_m < \infty \qquad \text{at} \quad r = 0 \tag{7.67c}$$

We note that the boundary condition (7.47c) is not yet satisfied but will be satisfied later.

Because $w(r,t)$ needs to satisfy the matching conditions (7.45), we let each $\phi_m(r)$ satisfy

the linear parts of the matching conditions. Consequently,

$$\phi_m^- = \phi_m^+ \tag{7.68a}$$

$$\left(\frac{\partial \phi_m}{\partial r}\right)^- = \left(\frac{\partial \phi_m}{\partial r}\right)^+ \tag{7.68b}$$

$$(M_{rr}^*)^- = (M_{rr}^*)^+ \tag{7.68c}$$

$$(Q_{\text{net}}^*)^- = (Q_{\text{net}}^*)^+ \tag{7.68d}$$

at the interfaces $r = r_{\text{in}}$ and $r = r_{\text{out}}$, where

$$Q_{\text{net}}^* = \frac{\partial M_{rr}^*}{\partial r} + \frac{M_{rr}^* - M_{\theta\theta}^*}{r} \qquad \forall\ r \in (0,1) \tag{7.69a}$$

$$M_{rr}^* = -D_{\text{rel}}\left(\frac{\partial^2 \phi_m}{\partial r^2} + \frac{\nu_{\text{eff}}}{r}\frac{\partial \phi_m}{\partial r}\right) \qquad \forall\ r \in \Re_{\text{c}} \tag{7.69b}$$

$$M_{rr}^* = -\left(\frac{\partial^2 \phi_m}{\partial r^2} + \frac{\nu}{r}\frac{\partial \phi_m}{\partial r}\right) \qquad \forall\ r \in \Re_{\text{nc}} \tag{7.69c}$$

$$M_{\theta\theta}^* = -D_{\text{rel}}\left(\nu_{\text{eff}}\frac{\partial^2 \phi_m}{\partial r^2} + \frac{1}{r}\frac{\partial \phi_m}{\partial r}\right) \qquad \forall\ r \in \Re_{\text{c}} \tag{7.69d}$$

$$\text{and}\quad M_{\theta\theta}^* = -\left(\nu\frac{\partial^2 \phi_m}{\partial r^2} + \frac{1}{r}\frac{\partial \phi_m}{\partial r}\right) \qquad \forall\ r \in \Re_{\text{nc}} \tag{7.69e}$$

The mode shapes are orthogonal with respect to the plate mass and are orthonormalized at our discretion; that is,

$$\int_0^1 r I_{\text{CMUT}}(r)\phi_m(r)\phi_n(r)dr = \delta_{mn} \tag{7.70}$$

where

$$I_{\text{CMUT}}(r) = \begin{cases} I_{\text{rel}}\,, & r \in \Re_{\text{c}} \\ 1 \quad , & r \in \Re_{\text{nc}} \end{cases} \tag{7.71}$$

Every mode shape $\phi_m(r)$ can now be determined with its associated modal frequency Ω_m. First, substitution of Equation (7.66) into Equations (7.67) and (7.68) results in a set of ten or six linear homogeneous equations in the unknown coefficients of $\phi_m(r)$, depending upon whether or not the electrode has a hole. As usual, the characteristic equation that enables solvability of the equation set can be solved for every modal frequency Ω_m. For every Ω_m, the resulting equation set has a rank of nine(five), but ten(six) unknowns still remain to be determined for $\phi_m(r)$. Finally, the orthonormal condition (Equation (7.70)) with $m = n$ gives

the extra condition needed to determine $\phi_m(r)$. For example, Figure 7.3 shows the first three modes for the same CMUT of Figure 7.2. Comparing Figures 7.2 and 7.3, we see that the electrode can affect any mode shape ϕ_i much more than the static deflection w_s, especially for larger electrodes.

Table 7.1 shows the first six modal frequencies for the CMUT of Figure 7.2 with various electrode thicknesses ($h_e = 0$, 0.2, 0.4, 0.6, or 0.8 μm) and radii ($r_{out} = 0.35$ or 0.70). The first modal frequency initially decreases with increasing electrode thickness (because of the increased mass) but then increases (due to the increased composite flexural rigidity). Both effects are greater for the larger electrode, whose values are bolded in Table 7.1, with Ω_1 decreasing from its initial value of 1.48 MHz to 1.43 MHz for $h_e = 0.4$ μm and rising to 1.50 MHz for $h_e = 0.8$ μm. The initial frequency decreases for all modes, even though this effect is not seen for modes higher than the second in Table 7.1 because of the jump in h_e from 0 to 0.2. However, the latter frequency increase is surely evident, especially for higher modes.

Table 7.1: Modal frequencies for the CMUT of Figure 7.3 with various electrode thicknesses and radii.

	h_e (μm)								
	0	0.2		0.4		0.6		0.8	
	r_{out}	r_{out}		r_{out}		r_{out}		r_{out}	
	N/A	0.35	0.70	0.35	0.70	0.35	0.70	0.35	0.70
Ω_1 (MHz)	**1.48**	1.46	**1.44**	1.45	**1.43**	1.46	**1.46**	1.46	**1.50**
Ω_2 (MHz)	6.27	6.25	6.30	6.32	6.48	6.47	6.75	6.67	7.05
Ω_3 (MHz)	14.71	14.73	14.79	14.91	15.26	15.20	16.01	15.56	16.97
Ω_4 (MHz)	26.82	26.91	27.01	27.35	28.01	27.96	29.61	28.59	31.54
Ω_5 (MHz)	42.65	42.78	42.95	43.55	44.43	44.78	46.67	46.22	49.25
Ω_6 (MHz)	62.18	62.38	62.60	63.34	64.70	64.87	68.05	66.81	72.29

At this point, the approximate solution for $w(r,t)$ in Equation (7.48a) satisfies the boundary conditions in Equations (7.47a), (7.47b), and (7.47d) for general $\eta_m(t)$. However, Equa-

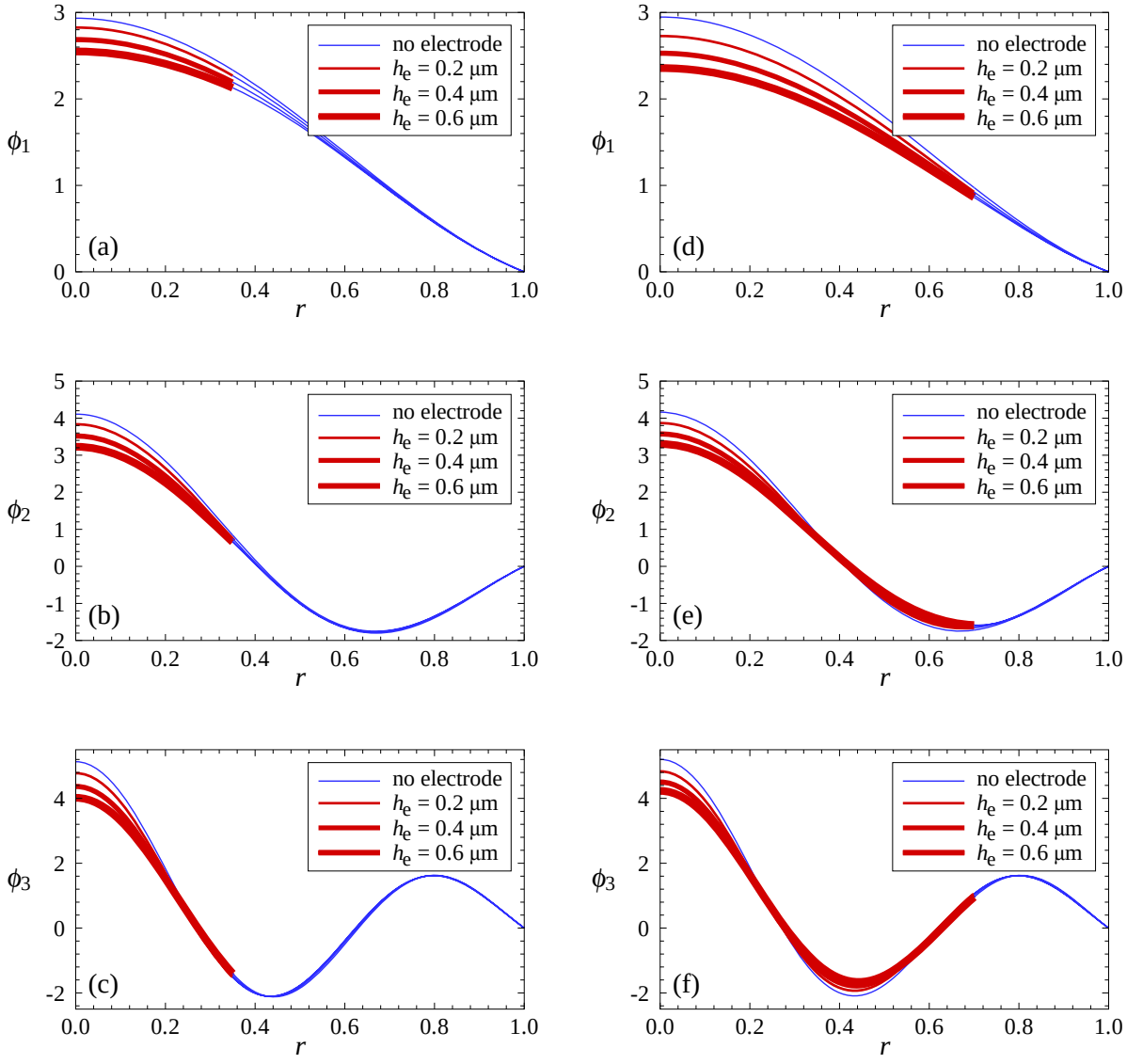

Figure 7.3: ϕ_i versus r for various h_e with (a) $r_{out} = 0.35$ and (b) $r_{out} = 0.7$ with no inner electrode radius ($r_{in} = 0$). For all cases, $h_p = 1.0$ μm, $R = 50$ μm, $d = 1.05$ μm, $E_p = 320$ GPa, $E_e = 67.6$ GPa, $\nu_p = 0.263$, $\nu_e = 0.3555$, $\hat{\tau} = 100$ MPa, $K_\tau = 0.8$, and $K_2 = 0.2$.

tion (7.47c) is still not satisfied. To satisfy this equation, we need the general expression for $\partial\Phi/\partial r$, which is a solution of the following compatibility equation for the CMUT:

$$r\frac{\partial^3\Phi}{\partial r^3} + \frac{\partial^2\Phi}{\partial r^2} - \frac{1}{r}\frac{\partial\Phi}{\partial r} = g(r,t) \tag{7.72}$$

where

$$g(r,t) = \begin{cases} \gamma_2 \left\{ -\frac{1}{2}\left(\frac{\partial w}{\partial r}\right)^2 + \gamma_1 r \frac{\partial}{\partial r}\left[\frac{1}{r}\frac{\partial}{\partial r}\left(r\frac{\partial w}{\partial r}\right)\right] \right\} + f_{\rm c}(t)\,, & r \in \Re_{\rm c} \\ -\frac{1}{2}\left(\frac{\partial w}{\partial r}\right)^2 + f_{\rm nc}^{\rm in}(t) & , \; r \in \Re_{\rm nc}^{\rm in} \\ -\frac{1}{2}\left(\frac{\partial w}{\partial r}\right)^2 + f_{\rm nc}^{\rm out}(t) & , \; r \in \Re_{\rm nc}^{\rm out} \end{cases} \tag{7.73}$$

according to Equations (7.43) and (7.44). The method of variation of parameters is used to obtain $\partial\Phi/\partial r$ as

$$\frac{\partial \Phi}{\partial r} = \frac{r}{2}\int_0^r \frac{g(\xi,t)}{\xi} d\xi - \frac{1}{2r}\int_0^r g(\xi,t)\xi d\xi + p_1(t)\, r \tag{7.74}$$

Using Equation (7.47c) to determine $p_1(t)$, we obtain

$$\frac{\partial \Phi}{\partial r} = \frac{\tau}{\beta} r - \frac{r}{2}\int_r^1 \frac{g(\xi,t)}{\xi} d\xi - \frac{1}{2r}\int_0^r g(\xi,t)\xi d\xi + \frac{r}{2}\int_0^1 g(\xi,t)\xi d\xi \tag{7.75}$$

Consequently, all of the boundary conditions in Equations (7.47) are satisfied by the approximate solution for $w(r,t)$ and its associated $\partial\Phi/\partial r$.

Using the condition that $g(r,t)$ is continuous at $r = r_{\rm in}$ and $r = r_{\rm out}$, we solve for $f_{\rm c}(t)$, $f_{\rm nc}^{\rm in}(t)$, and $f_{\rm nc}^{\rm out}(t)$ and obtain

$$g(r,t) = G_s(r) + \eta_i(t) G_i(r) + \eta_i(t)\eta_j(t) G_{ij}(r) \tag{7.76}$$

for the Galerkin approach, where Einstein's convention holds in Equation (7.76),

$$G_s = \begin{cases} -\frac{\gamma_2}{2}\left(w_s'\right)^2 + \gamma_1\gamma_2 r\left[\frac{1}{r}\left(r\, w_s'\right)'\right]' + F_s(r_{\rm in})\,, & r \in \Re_{\rm c} \\ -\frac{1}{2}\left(w_s'\right)^2 & , \; r \in \Re_{\rm nc}^{\rm in} \\ -\frac{1}{2}\left(w_s'\right)^2 + F_s(r_{\rm in}) - F_s(r_{\rm out}) & , \; r \in \Re_{\rm nc}^{\rm out} \end{cases} \tag{7.77a}$$

$$G_i = \begin{cases} -\gamma_2 w_s'\phi_i' + \gamma_1\gamma_2 r\left[\frac{1}{r}\left(r\,\phi_i'\right)'\right]' + F_i(r_{\rm in})\,, & r \in \Re_{\rm c} \\ -w_s'\phi_i' & , \; r \in \Re_{\rm nc}^{\rm in} \\ -w_s'\phi_i' + F_i(r_{\rm in}) - F_i(r_{\rm out}) & , \; r \in \Re_{\rm nc}^{\rm out} \end{cases} \tag{7.77b}$$

$$G_{ij} = \begin{cases} -\frac{\gamma_2}{2}\phi_i'\phi_j' + F_{ij}(r_{\rm in}) & , \; r \in \Re_{\rm c} \\ -\frac{1}{2}\phi_i'\phi_j' & , \; r \in \Re_{\rm nc}^{\rm in} \\ -\frac{1}{2}\phi_i'\phi_j' + F_{ij}(r_{\rm in}) - F_{ij}(r_{\rm out})\,, & r \in \Re_{\rm nc}^{\rm out} \end{cases} \tag{7.77c}$$

and

$$F_s = \frac{\gamma_2 - 1}{2}\left(w_s'\right)^2 - \gamma_1\gamma_2 r\left[\frac{1}{r}\left(r\, w_s'\right)'\right]' \tag{7.78a}$$

$$F_i = \left(\gamma_2 - 1\right) w_s'\phi_i' - \gamma_1\gamma_2 r\left[\frac{1}{r}\left(r\, \phi_i'\right)'\right]' \tag{7.78b}$$

$$F_{ij} = \frac{\gamma_2 - 1}{2}\phi_i'\phi_j' \tag{7.78c}$$

Substitution of Equation (7.76) into Equation (7.75) yields

$$\frac{\partial \Phi}{\partial r} = \Phi_s'(r) + \eta_i(t)\Gamma_i'(r) + \eta_i(t)\eta_j(t)\psi_{ij}'(r) \tag{7.79}$$

where

$$\Phi_s' = \frac{\tau}{\beta}r - \frac{r}{2}\int_r^1 \frac{G_s(\xi)}{\xi}d\xi - \frac{1}{2r}\int_0^r G_s(\xi)\xi d\xi + \frac{r}{2}\int_0^1 G_s(\xi)\xi d\xi \tag{7.80a}$$

$$\Gamma_i' = -\frac{r}{2}\int_r^1 \frac{G_i(\xi)}{\xi}d\xi - \frac{1}{2r}\int_0^r G_i(\xi)\xi d\xi + \frac{r}{2}\int_0^1 G_i(\xi)\xi d\xi \tag{7.80b}$$

$$\psi_{ij}' = -\frac{r}{2}\int_r^1 \frac{G_{ij}(\xi)}{\xi}d\xi - \frac{1}{2r}\int_0^r G_{ij}(\xi)\xi d\xi + \frac{r}{2}\int_0^1 G_{ij}(\xi)\xi d\xi \tag{7.80c}$$

7.5 Reduced-Order Composite Model

Equations (7.41) can be combined into

$$\begin{aligned} I_{\mathrm{CMUT}}(r)\frac{\partial^2 w}{\partial t^2} + 2\,c\frac{\partial w}{\partial t} + D_{\mathrm{CMUT}}(r)\nabla^4 w = \frac{\beta}{r}\frac{\partial}{\partial r}\left(\frac{\partial w}{\partial r}\frac{\partial \Phi}{\partial r}\right) \\ + F(r,t) + H_{\mathrm{CMUT}}(r)\left[-\gamma_1\beta\nabla^4\Phi + \frac{v^2(t)}{(1-w)^2}\right] \end{aligned} \tag{7.81}$$

where $I_{\mathrm{CMUT}}(r)$ is defined in Equation (7.71) and

$$D_{\mathrm{CMUT}}(r) = \begin{cases} D_{\mathrm{rel}}\,, & r \in \Re_{\mathrm{c}} \\ 1 \quad\;, & r \in \Re_{\mathrm{nc}} \end{cases} \tag{7.82a}$$

$$H_{\mathrm{CMUT}}(r) = \begin{cases} 1\,, & r \in \Re_{\mathrm{c}} \\ 0\,, & r \in \Re_{\mathrm{nc}} \end{cases} \tag{7.82b}$$

We substitute Equations (7.48a) and (7.79) into Equation (7.81) and obtain

$$\begin{aligned}
&\left(I_{\mathrm{CMUT}}\,\ddot{\eta}_m + 2\,c\,\dot{\eta}_m\right)\phi_m + D_{\mathrm{CMUT}}\,\eta_m\nabla^4\phi_m \\
&\quad = \frac{\beta}{r}\frac{\partial}{\partial r}\Big[\left(w_s' + \eta_m\phi_m'\right)\left(\Phi_s' + \eta_m\Gamma_m' + \eta_m\eta_n\psi_{mn}'\right)\Big] + F(r,t) \\
&\quad + H_{\mathrm{CMUT}}\left\{-\gamma_1\beta\nabla^4\Phi + v^2(t)\Big[1 - \left(w_s + \eta_m\phi_m\right)\Big]^{-2}\right\}
\end{aligned} \tag{7.83}$$

for $q = 1,\, 2, \ldots,\, N$ with the summations signs for m and n removed for notation simplification.

Next, to determine a reduced-order composite model, we rearrange Equation (7.83) as

$$\begin{aligned}
&\left(I_{\mathrm{CMUT}}\,\ddot{\eta}_m + 2\,c\,\dot{\eta}_m\right)\phi_m + D_{\mathrm{CMUT}}\,\nabla^4 w \\
&\quad = \frac{\beta}{r}\frac{\partial}{\partial r}\big[f + \eta_m f_m + \eta_m\eta_n f_{mn} + \eta_m\eta_n\eta_p f_{mnp}\big] + F(r,t) \\
&\quad + H_{\mathrm{CMUT}}\left\{-\gamma_1\beta\nabla^4\Phi + v^2(t)\Big[1 - \left(w_s + \eta_m\phi_m\right)\Big]^{-2}\right\}
\end{aligned} \tag{7.84}$$

where f, f_m, f_{mn}, and f_{mnp} and defined in Equations (6.29). Next, according to Equation (7.42a), we have

$$H_{\mathrm{CMUT}}\,\nabla^4\Phi = \begin{cases} \gamma_2\left(-\frac{1}{r}\frac{\partial^2 w}{\partial r^2}\frac{\partial w}{\partial r} + \gamma_1\nabla^4 w\right), & r \in \Re_{\mathrm{c}} \\ 0 \qquad\qquad\qquad\qquad\quad , & r \in \Re_{\mathrm{nc}} \end{cases} \tag{7.85}$$

Equations (7.48a) and (7.65a) are then used in Equation (7.85) to obtain

$$H_{\mathrm{CMUT}}\,\nabla^4\Phi = H_{\mathrm{CMUT}}\left[R_s(r) + \eta_i(t)R_i(r) + \eta_i(t)\eta_j(t)R_{ij}(r)\right] \tag{7.86}$$

where

$$R_s = -\frac{\gamma_2}{r}w_s''w_s' + \gamma_1\gamma_2\nabla^4 w_s \tag{7.87a}$$

$$R_i = -\frac{\gamma_2}{r}\left(w_s''\phi_i' + w_s'\phi_i''\right) + \gamma_1\gamma_2\frac{I_{\mathrm{rel}}}{D_{\mathrm{rel}}}\Omega_i^2\phi_i \tag{7.87b}$$

$$R_{ij} = -\frac{\gamma_2}{r}\phi_i''\phi_j' \tag{7.87c}$$

Then, we multiply Equation (7.84) with $\Big[1 - \left(w_s + \eta_m\phi_m\right)\Big]^2$, multiply every term by $r\phi_q$,

integrate the outcome over $r \in [0,1]$, and obtain

$$\begin{aligned}
&\ddot{\eta}_m\Big[A^*_{mq} + \eta_i A^*_{imq} + \eta_i\eta_j A^*_{ijmq}\Big] + 2\,c\,\dot{\eta}_m\Big[A_{mq} + \eta_i A_{imq} + \eta_i\eta_j A_{ijmq}\Big] \\
&\quad + \int_0^1 (1-w)^2\, D_{\mathrm{CMUT}}\, r\,\phi_q \nabla^4 w\, dr = \beta\Big[B_q + \eta_m B_{mq} + \eta_m\eta_n B_{mnq} \\
&\qquad + \eta_m\eta_n\eta_p B_{mnpq} + \eta_i\eta_m\eta_n\eta_p B_{imnpq} + \eta_i\eta_j\eta_m\eta_n\eta_p B_{ijmnpq}\Big] \\
&\qquad - \gamma_1\beta\Big[T_q + \eta_m T_{mq} + \eta_m\eta_n T_{mnq} + \eta_m\eta_n\eta_p T_{mnpq} + \eta_i\eta_m\eta_n\eta_p T_{imnpq}\Big] \\
&\qquad + I_q + \eta_i J_{iq} + \eta_i\eta_j K_{ijq} + v^2(t) L_q
\end{aligned} \tag{7.88}$$

where

$$A^*_{mq} = \int_0^1 I_{\mathrm{CMUT}}\,(1-w_s)^2\, r\phi_m\phi_q dr \tag{7.89a}$$

$$A^*_{imq} = -2\int_0^1 I_{\mathrm{CMUT}}\,(1-w_s)\, r\phi_i\phi_m\phi_q dr \tag{7.89b}$$

$$A^*_{ijmq} = \int_0^1 I_{\mathrm{CMUT}}\, r\phi_i\phi_j\phi_m\phi_q dr \tag{7.89c}$$

$$T_q = \int_{r_{\mathrm{in}}}^{r_{\mathrm{out}}} (1-w_s)^2\, R_s r\phi_q dr \tag{7.89d}$$

$$T_{mq} = \int_{r_{\mathrm{in}}}^{r_{\mathrm{out}}} \Big[(1-w_s)^2\, R_m r\phi_q - 2\,(1-w_s)\, R_s r\phi_m\phi_q\Big]\, dr \tag{7.89e}$$

$$T_{mnq} = \int_{r_{\mathrm{in}}}^{r_{\mathrm{out}}} \Big[(1-w_s)^2\, R_{mn} r\phi_q - 2\,(1-w_s)\, R_m r\phi_n\phi_q + R_s r\phi_m\phi_n\phi_q\Big]\, dr \tag{7.89f}$$

$$T_{mnpq} = \int_{r_{\mathrm{in}}}^{r_{\mathrm{out}}} \left[R_p r\phi_m\phi_n\phi_p\phi_q - 2\,(1-w_s)\, R_{mn} r\phi_p\phi_q\right] dr \tag{7.89g}$$

$$T_{imnpq} = \int_{r_{\mathrm{in}}}^{r_{\mathrm{out}}} R_{im} r\phi_n\phi_p\phi_q\, dr \tag{7.89h}$$

$$L_q = \int_{r_{\mathrm{in}}}^{r_{\mathrm{out}}} r\phi_q dr \tag{7.89i}$$

and all of the other indexed parameters were already defined in Equations (6.31).

To complete the reduced-order composite model, we must determine the remaining integral term in Equation (7.88). To this end, we first write the integral as

$$\begin{aligned}
&\int_0^1 (1-w)^2\, D_{\mathrm{CMUT}}\, r\,\phi_q \nabla^4 w\, dr = \int_0^1 D_{\mathrm{CMUT}}\, r\,\phi_q \nabla^4 w\, dr \\
&- 2\int_0^1 w D_{\mathrm{CMUT}}\, r\,\phi_q \nabla^4 w\, dr + \int_0^1 w^2 D_{\mathrm{CMUT}}\, r\,\phi_q \nabla^4 w\, dr
\end{aligned} \tag{7.90}$$

Now, the equation of motion in Equation (7.84) needs to be satisfied along with the matching conditions in Equations (7.45) and the boundary conditions in Equations (7.47). Thus far, the boundary conditions are satisfied, but the matching conditions are only partially satisfied through the shape functions. Specifically, the matching conditions for the shape functions in Equations (7.68) do not include the nonlinearities present in the full matching conditions.

To satisfy the matching conditions, we need to incorporate them into Equation (7.88). To do so, we use the first integral on the right-hand side in Equation (7.90), which can be broken into parts as

$$\begin{aligned}\int_0^1 D_{\mathrm{CMUT}}\, r\, \phi_q \nabla^4 w\, dr &= \int_0^{r_{\mathrm{in}}} r\, \phi_q \nabla^4 w\, dr \\ &+ D_{\mathrm{rel}} \int_{r_{\mathrm{in}}}^{r_{\mathrm{out}}} r\, \phi_q \nabla^4 w\, dr + \int_{r_{\mathrm{out}}}^1 r\, \phi_q \nabla^4 w\, dr \end{aligned} \tag{7.91}$$

Through two successive integrations by parts, the general form of the integrals on the right-hand side of Equation (7.91) can be shown to be

$$\int_{r_{\mathrm{a}}}^{r_{\mathrm{b}}} r\, \phi_q \nabla^4 w\, dr = \int_{r_{\mathrm{a}}}^{r_{\mathrm{b}}} \frac{1}{r}\frac{\partial}{\partial r}\left(r\frac{\partial w}{\partial r}\right)\left(r\phi_q'\right)' dr + \varphi(r_{\mathrm{a}}, r_{\mathrm{b}}, t) \tag{7.92}$$

where

$$\varphi(r_{\mathrm{a}}, r_{\mathrm{b}}, t) = \left\{ r\frac{\partial}{\partial r}\left[\frac{1}{r}\frac{\partial}{\partial r}\left(r\frac{\partial w}{\partial r}\right)\right]\phi_q - \frac{\partial}{\partial r}\left(r\frac{\partial w}{\partial r}\right)\phi_q' \right\}\Bigg|_{r_{\mathrm{a}}}^{r_{\mathrm{b}}} \tag{7.93}$$

for general r_{a} and r_{b}. Consequently, Equation (7.91) is rearranged into

$$\begin{aligned}\int_0^1 D_{\mathrm{CMUT}}\, r\, \phi_q \nabla^4 w\, dr &= \int_0^1 D_{\mathrm{CMUT}}\, \frac{1}{r}\frac{\partial}{\partial r}\left(r\frac{\partial w}{\partial r}\right)\left(r\phi_q'\right)' dr \\ &+ \varphi(0, r_{\mathrm{in}}, t) + D_{\mathrm{rel}}\, \varphi(r_{\mathrm{in}}, r_{\mathrm{out}}, t) + \varphi(r_{\mathrm{out}}, 1, t) \end{aligned} \tag{7.94}$$

Every derivative of ϕ_q in Equation (7.93) is known, but the derivatives of $w(r,t)$ depend on the matching conditions, which we use to show that, after much rearranging,

$$\begin{aligned}\int_0^1 D_{\mathrm{CMUT}}\, r\, \phi_q \nabla^4 w\, dr &= \int_0^1 D_{\mathrm{CMUT}}\, \frac{1}{r}\frac{\partial}{\partial r}\left(r\frac{\partial w}{\partial r}\right)\left(r\phi_q'\right)' dr \\ &+ B_q(r_{\mathrm{in}}, t) - B_q(r_{\mathrm{out}}, t) - \left[\phi_q'\left(\frac{\partial w}{\partial r} + \frac{\partial^2 w}{\partial r^2}\right)\right]\Bigg|_{r=1} \end{aligned} \tag{7.95}$$

where

$$B_q(r,t) = \beta\left[\gamma_1\, g(r,t)\,\phi_q + \phi_q'\left(h_{\text{eff}}\frac{\partial\Phi}{\partial r} - r\,\gamma_1\frac{\partial^2\Phi}{\partial r^2}\right)\right] + \phi_q'\left[D_{\text{rel}}\left(1-\nu_{\text{eff}}\right) - \left(1-\nu_{\text{p}}\right)\right]\frac{\partial w}{\partial r} \tag{7.96}$$

which accounts for the nonlinear matching conditions. Substitution of Equation (7.95) into Equation (7.90) yields

$$\begin{aligned}\int_0^1 (1-w)^2 D_{\text{CMUT}}\, r\,\phi_q\nabla^4 w\, dr &= \int_0^1 D_{\text{CMUT}}\left[\frac{1}{r}\frac{\partial}{\partial r}\left(r\frac{\partial w}{\partial r}\right)\left(r\phi_q'\right)' + w\,(w-2)\,r\,\phi_q\nabla^4 w\right] dr \\ &\quad + B_q(r_{\text{in}},t) - B_q(r_{\text{out}},t) - \left[\phi_q'\left(\frac{\partial w}{\partial r} + \frac{\partial^2 w}{\partial r^2}\right)\right]\Bigg|_{r=1}\end{aligned} \tag{7.97}$$

Finally, for the Galerkin approach, Equation (7.97) is

$$\begin{aligned}\int_0^1 (1-w)^2\, D_{\text{CMUT}}\, r\,\phi_q\nabla^4 w\, dr &= U_q + \eta_i U_{iq} + \eta_i\eta_j U_{ijq} + \eta_i\eta_j\eta_k U_{ijkq} \\ &\quad + [W_q(r_{\text{in}}) - W_q(r_{\text{out}})] + \eta_i[W_{iq}(r_{\text{in}}) - W_{iq}(r_{\text{out}})] \\ &\quad + \eta_i\eta_j[W_{ijq}(r_{\text{in}}) - W_{ijq}(r_{\text{out}})]\end{aligned} \tag{7.98}$$

where

$$U_q = \int_0^1 D_{\text{CMUT}}\left[\frac{1}{r}\left(r\,w_s'\right)'\left(r\,\phi_q'\right)' + w_s\,(w_s-2)\,r\,\phi_q\nabla^4 w_s\right] dr - \left[\phi_q'\left(w_s' + w_s''\right)\right]\Big|_{r=1} \tag{7.99a}$$

$$U_{iq} = \int_0^1 D_{\text{CMUT}}\left[\frac{1}{r}\left(r\,\phi_i'\right)'\left(r\,\phi_q'\right)' + 2\,(w_s-1)\,r\,\phi_i\,\phi_q\nabla^4 w_s + w_s\,(w_s-2)\,r\,\phi_q\nabla^4\phi_i\right] dr - \left[\phi_q'\left(\phi_i' + \phi_i''\right)\right]\Big|_{r=1} \tag{7.99b}$$

$$U_{ijq} = \int_0^1 D_{\text{CMUT}}\left[r\,\phi_i\,\phi_j\,\phi_q\,\nabla^4 w_s + 2\,(w_s-1)\,r\,\phi_i\,\phi_q\nabla^4\phi_j\right] dr \tag{7.99c}$$

$$U_{ijkq} = \int_0^1 D_{\text{CMUT}}\, r\,\phi_j\,\phi_k\,\phi_q\,\nabla^4\phi_i\, dr \tag{7.99d}$$

$$W_q = \beta\Big[\gamma_1\,\phi_q\,G_s + h_{\text{eff}}\,\phi_q'\,\Phi_s' - r\,\gamma_1\phi_q'\Phi_s''\Big] + \phi_q'\left[D_{\text{rel}}\left(1-\nu_{\text{eff}}\right) - \left(1-\nu_{\text{p}}\right)\right] w_s' \tag{7.99e}$$

$$W_{iq} = \beta\Big[\gamma_1\,\phi_q\,G_i + h_{\text{eff}}\,\phi_q'\,\Gamma_i' - r\,\gamma_1\phi_q'\Gamma_i''\Big] + \phi_q'\left[D_{\text{rel}}\left(1-\nu_{\text{eff}}\right) - \left(1-\nu_{\text{p}}\right)\right]\phi_i' \tag{7.99f}$$

$$W_{ijq} = \beta\Big[\gamma_1\,\phi_q\,G_{ij} + h_{\text{eff}}\,\phi_q'\,\psi_{ij}' - r\,\gamma_1\phi_q'\psi_{ij}''\Big] \tag{7.99g}$$

When Equation (7.98) is substituted into Equation (7.88), we obtain

$$\begin{aligned}
&\ddot{\eta}_m\Big[A^*_{mq}+\eta_i A^*_{imq}+\eta_i\eta_j A^*_{ijmq}\Big]+2\,c\,\dot{\eta}_m\Big[A_{mq}+\eta_i A_{imq}+\eta_i\eta_j A_{ijmq}\Big]\\
&\quad+U_q+\eta_i U_{iq}+\eta_i\eta_j U_{ijq}+\eta_i\eta_j\eta_k U_{ijkq}\\
&\qquad=[W_q(r_{\text{out}})-W_q(r_{\text{in}})]+\eta_i[W_{iq}(r_{\text{out}})-W_{iq}(r_{\text{in}})]\\
&\qquad\quad+\eta_i\eta_j[W_{ijq}(r_{\text{out}})-W_{ijq}(r_{\text{in}})]\\
&\qquad+\beta\Big[B_q+\eta_m B_{mq}+\eta_m\eta_n B_{mnq}+\eta_m\eta_n\eta_p B_{mnpq}\\
&\qquad\quad+\eta_i\eta_m\eta_n\eta_p B_{imnpq}+\eta_i\eta_j\eta_m\eta_n\eta_p B_{ijmnpq}\Big]\\
&\qquad-\gamma_1\beta\Big[T_q+\eta_m T_{mq}+\eta_m\eta_n T_{mnq}+\eta_m\eta_n\eta_p T_{mnpq}+\eta_i\eta_m\eta_n\eta_p T_{imnpq}\Big]\\
&\qquad+I_q+\eta_i J_{iq}+\eta_i\eta_j K_{ijq}+v^2(t)L_q
\end{aligned}\tag{7.100}$$

We collect all of the $\eta_m(t)$ into a column vector $\boldsymbol{\eta}(t)$, rearrange Equation (7.100), and obtain

$$M^*(\boldsymbol{\eta})\ddot{\boldsymbol{\eta}}+2cM(\boldsymbol{\eta})\dot{\boldsymbol{\eta}}+N^*(\boldsymbol{\eta})\boldsymbol{\eta}=P^*(\boldsymbol{\eta})+v^2(t)\boldsymbol{L}^*\tag{7.101}$$

where

$$M(\boldsymbol{\eta})=[M_{qm}(\boldsymbol{\eta})]=[A_{mq}+\eta_i A_{imq}+\eta_i\eta_j A_{ijmq}]\tag{7.102a}$$

$$M^*(\boldsymbol{\eta})=[M^*_{qm}(\boldsymbol{\eta})]=[A^*_{mq}+\eta_i A^*_{imq}+\eta_i\eta_j A^*_{ijmq}]\tag{7.102b}$$

$$N^*(\boldsymbol{\eta})=[N^*_{qm}(\boldsymbol{\eta})]=[U_{mq}+\eta_i U_{imq}+\eta_i\eta_j U_{ijmq}]\tag{7.102c}$$

$$\begin{aligned}
P^*(\boldsymbol{\eta})=\{P_q(\boldsymbol{\eta})\}=\Big\{&[W_q(r_{\text{out}})-W_q(r_{\text{in}})]+\eta_i[W_{iq}(r_{\text{out}})-W_{iq}(r_{\text{in}})]\\
&+\eta_i\eta_j[W_{ijq}(r_{\text{out}})-W_{ijq}(r_{\text{in}})]-U_q\\
&+\beta\big(B_q+\eta_m B_{mq}+\eta_m\eta_n B_{mnq}+\eta_m\eta_n\eta_p B_{mnpq}\\
&\quad+\eta_i\eta_m\eta_n\eta_p B_{imnpq}+\eta_i\eta_j\eta_m\eta_n\eta_p B_{ijmnpq}\big)\\
&-\gamma_1\beta\Big(T_q+\eta_m T_{mq}+\eta_m\eta_n T_{mnq}+\eta_m\eta_n\eta_p T_{mnpq}\\
&\quad+\eta_i\eta_m\eta_n\eta_p T_{imnpq}\Big)+I_q+\eta_i J_{iq}+\eta_i\eta_j K_{ijq}\Big\}
\end{aligned}\tag{7.102d}$$

$$\boldsymbol{L}^*=\{L_q\}\tag{7.102e}$$

with Einstein's convention holding for all terms.

Once all of the $\eta_m(t)$ are determined by solving the reduced-order composite model, Equation (7.101), the CMUT deflection $w(r,t)$ is given approximately by Equation (7.48a).

7.6 Validation of Composite Macromodel

7.6.1 Validation of Deflections and First Natural Frequency

Yaralioglu et al. (2001) performed FEM simulations of a circular silicon-nitride plate that is mounted with a centered aluminum electrode, in order to determine how the residual stress and Young's modulus affect the deflection. A circular cross section of the CMUT used for the simulation is shown in Figure 7.4(a), and the material properties of the CMUT are listed in Table 7.2. For Figure 7.4(a), $w = 46$ μm, $t = 0.88$ μm, $g = 0.113$ μm, and the aluminum electrode has a thickness of 0.30 μm and a diameter half that of the silicon-nitride plate. Furthermore, the CMUT is sealed with a vacuum underneath, meaning that a net pressure exists over the CMUT, which was assumed to be 1 atm (101.325 kPa) for the FEM simulations.

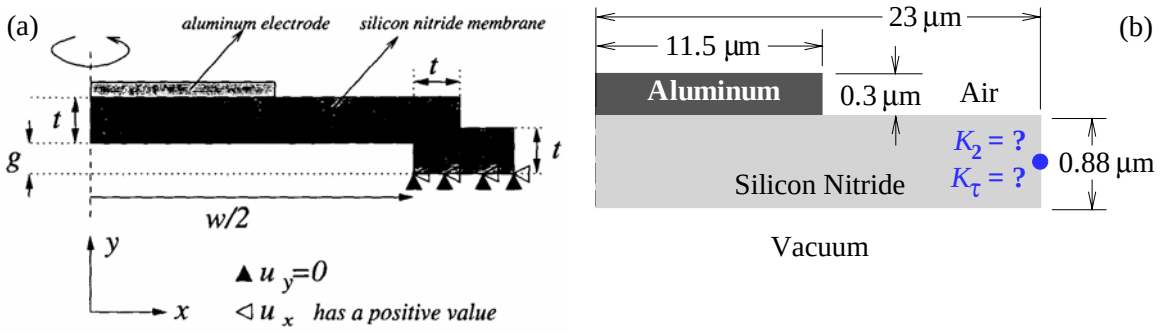

Figure 7.4: (a) A schematic of the CMUT for FEM simulation (from Yaralioglu et al. (2001)) and (b) a schematic of a similar CMUT for composite macromodel simulation.

Table 7.2: Material parameters used by Yaralioglu et al. (2001) in their FEM simulations.

Material	Young's modulus (GPa)	Poisson's ratio	density (kg/m^3)
Silicon Nitride	100−400	0.263	3270
Aluminum	67.6	0.355	2700

We apply the composite macromodel for this case, as seen in Figure 7.4(b), by choosing appropriate values for the parameters K_2 and K_τ. Based on the FEM results in Figure 7.5 for varying residual stress $\hat{\tau}$ and Young's modulus E_p, only two points are required to independently determine K_2 and K_τ. Using a gap width of 1 μm (to allow for a deflection larger than g), we fitted the macromodel to the FEM simulation at the red square ($\hat{\tau} = 0$ MPa, $E_\mathrm{p} = 100$ GPa) and obtained $K_2 = 0.01$ and at the red circle ($\hat{\tau} = 400$ MPa, $E_\mathrm{p} = 400$ GPa) and obtained $K_\tau = 0.011\,\tau$.

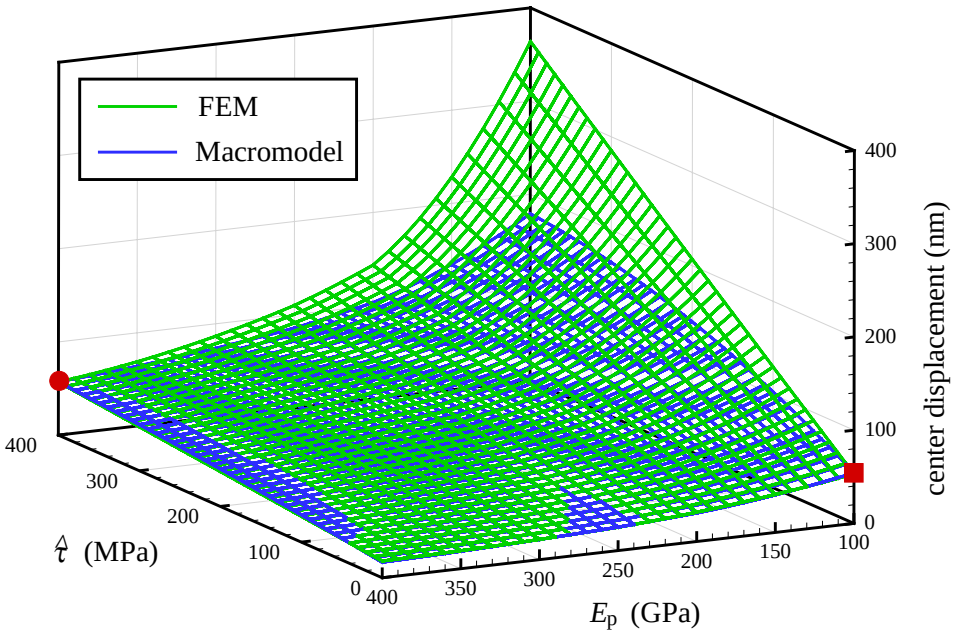

Figure 7.5: Deflection at the center of the CMUT as a function of residual stress and the plate's Young's modulus. The FEM results were adapted from Yaralioglu et al. (2001) and the composite macromodel was fitted to yield $K_2 = 0.01$ and $K_\tau = 0.011\,\tau$.

In general, the center deflections from the macromodel fall below those from the FEM simulation, with the largest differences between the two data sets occuring at higher residual stresses and reaching more than 50% in relative error. However, the first natural frequencies that accompany the deflections in Figure 7.5 are close to those obtained with the FEM

simulations, as seen in Figure 7.6. Once again, the largest error between the two frequency sets occurs at higher residual stresses, but is only 2.5% at most.

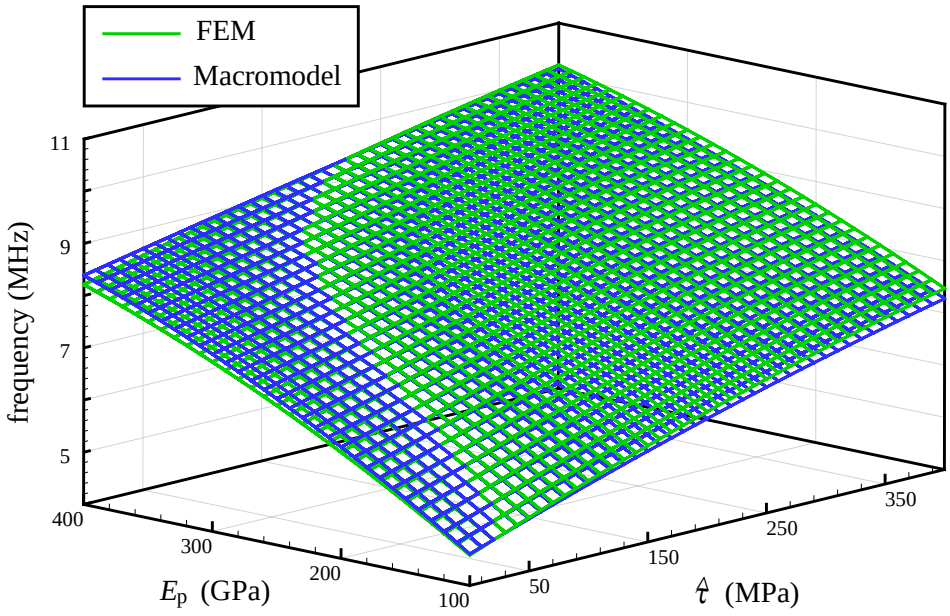

Figure 7.6: First natural frequency of the CMUT as a function of residual stress and the plate's Young's modulus. The FEM results were adapted from Yaralioglu et al. (2001) and $K_2 = 0.01$ and $K_\tau = 0.011\,\tau$ are used in the composite macromodel.

The large errors in the deflection at higher stresses may be due to several factors. First, even though numerical convergence was achieved, perhaps the large errors are due to the Galerkin approach. Figure 7.7 shows the ratio of the nondimensional stress τ to the relative plate flexural rigidity D_{rel}. The relative errors from Figure 7.5 are smallest(largest) when τ/D_{rel} is small(large). When τ/D_{rel} is at its largest value of about 15, the first term on the right-hand side of Equations (7.41) dominates over the biharmonic plate term on the left-hand side. Therefore, perhaps most of the error for large relative stresses occurs because the modes used in the Galerkin model do not include the in-plane stress, which dominates the physics for this case. Second, because the macromodel and FEM frequencies match very

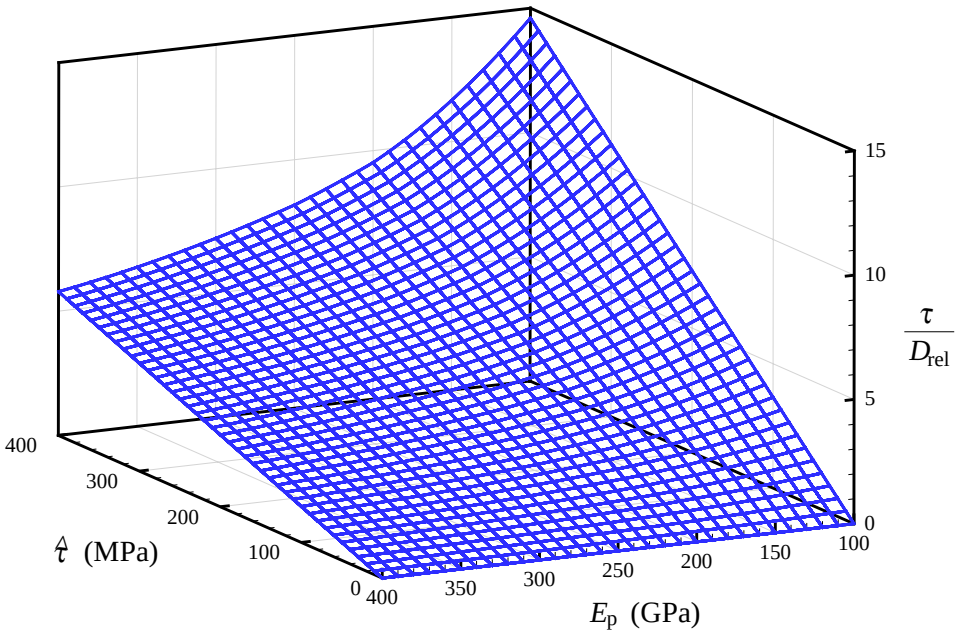

Figure 7.7: Ratio of nondimensional stress to relative plate flexural rigidity of the composite regime for the CMUT investigated by Yaralioglu et al. (2001).

well, it appears that the macromodel captures the physics well. And since the deflections for this case are fairly uncoupled from the frequencies (due to a lack of electric forcing), perhaps most of the error in the deflection occurs because the assumed boundary conditions for $\partial w/\partial r$, which highly affect the plate deflection, are too simplistic and ignore significant boundary effects that are captured in the FEM simulations.

Thus, the composite macromodel may be used to approximate the CMUT frequencies due to the residual and atmospheric forces within the physical ranges for the residual stress and Young's modulus in Figure 7.5, which are fairly representative of actual CMUT ranges (Ladabaum et al., 1998). However, the composite macromodel might not be useful as an effective modeling tool with the current boundary conditions because the deflections may be severely underestimated. By fitting the FEM results to experimental data, Yaralioglu et al. determined that $\hat{\tau} = 124.5$ MPa and $E_{\text{p}} = 255.4$ GPa for a given experimental CMUT. Using these

values in the macromodel, we determined the deflection of the CMUT to compare it with the experimental data, of which a typical experimental deflection is seen in Figure 7.8. The macromodel deflection matches the actual behavior, despite the asymmetry of the typical experimental curve. In fact, out of ten trials, the average experimental deflection at the plate center was about 50 nm, which is close to the predicted value of about 49 nm.

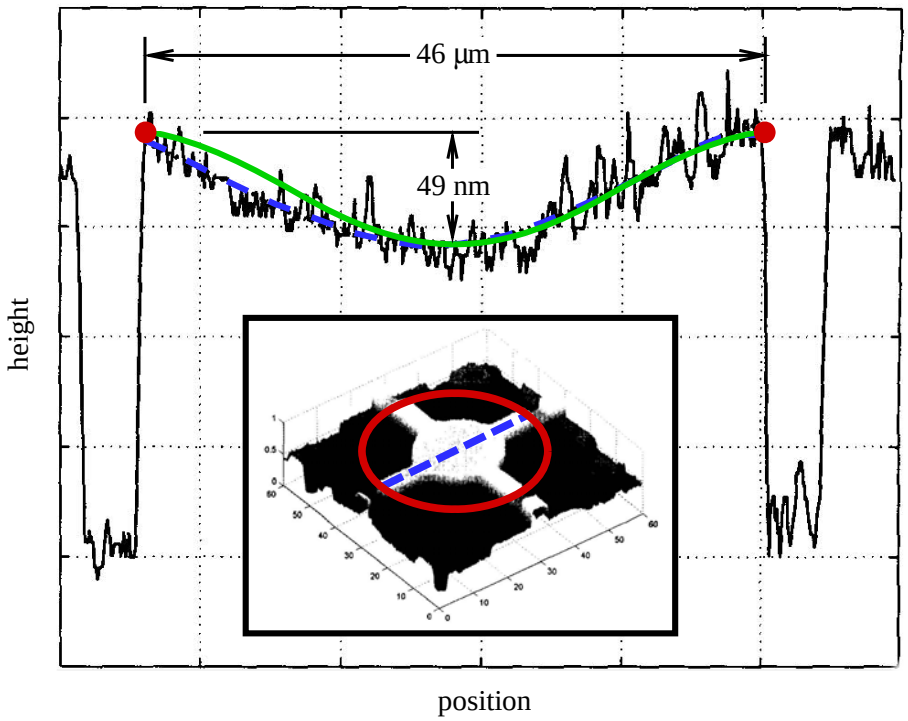

Figure 7.8: Experimental and predicted deflections of the CMUT. The experimental results were adapted from Yaralioglu et al. (2001) and the composite macromodel used $\hat{\tau} = 124.5$ MPa and $E_{\mathrm{p}} = 255.4$ GPa.

7.6.2 Validation of Pull-in Voltages

Caronti et al. (2004) performed FEM simulations to determine the deflections and pull-in voltages of a circular silicon-nitride plate that has an embedded aluminum electrode of varying radius. A circular cross section of the CMUT used for the simulation is shown in

Figure 7.9 and the material properties of the CMUT are listed in Table 7.3.

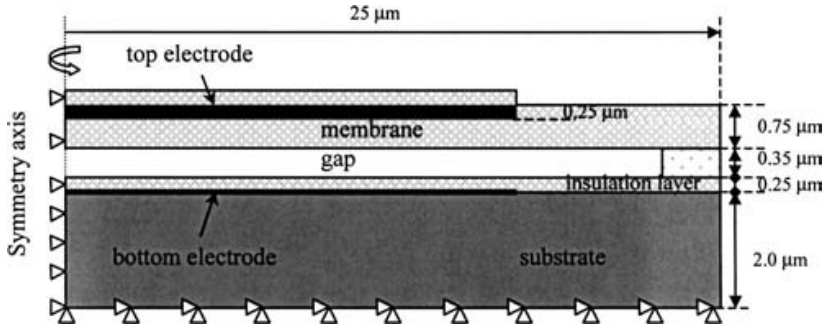

Figure 7.9: A schematic of the CMUT for FEM simulation (from Caronti et al. (2004)).

Table 7.3: Material parameters used by Caronti et al. (2004) in their FEM simulations.

Material	Young's modulus (GPa)	Poisson's ratio	density (kg/m^3)
Silicon Nitride	280	0.26	3200
Aluminum	67.6	0.35	2700

Because the membrane for the FEM simulation had no tensile stress, we let $K_\tau = 0$ in the composite macromodel. We found out that when $K_2 = 0.04$ both of the resulting plate center deflections for a bias voltage of 80 V and the collapse voltages are very similar to those of the FEM simulation, as seen in Figure 7.10. As the normalized electrode radius decreases, the CMUT initially deflects more and the pull-in voltage initially decreases. These effects are due to the decrease in the overall CMUT stiffness for smaller electrodes. However, as the electrode becomes even smaller, the deflection magnitude eventually reaches a maximum and then decreases. Likewise, the pull-in voltage eventually reaches a minimum with decreasing electrode size. These effects are due to the decrease in the electrostatic force for a smaller electrode. As shown in Figure 7.11(b), the deflection increases and then decreases in magnitude as the electrode size decreases. In contrast, for an electrode of zero thickness, the plate deflection will always decrease in magnitude as the electrode becomes smaller, as seen

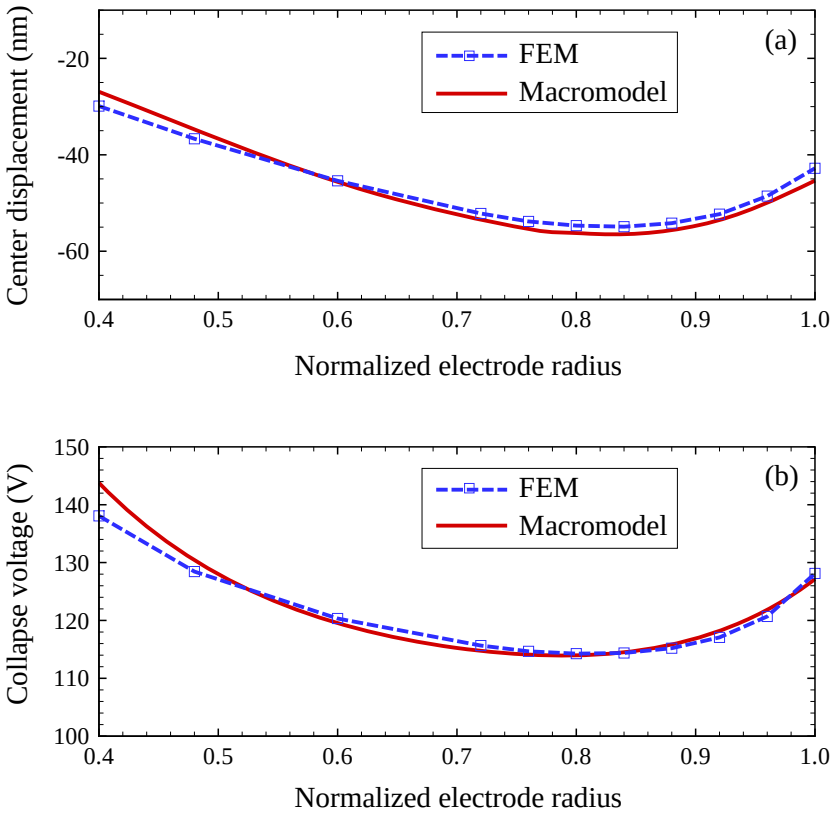

Figure 7.10: (a) Deflection at the center of the CMUT for a bias voltage of 80 V and (b) pull-in voltages as a function of the normalized electrode radius. The FEM results were adapted from Caronti et al. (2004) and the composite macromodel was fitted to yield $K_2 = 0.04$ for $K_\tau = 0$.

in Figure 7.11(a), because there is no electrode stiffness to affect the deflection.

7.6.3 Validation of Nonlinear Dynamics

The forced vibration characteristics obtained with the macromodel predictions are in good agreement with experimental data from Yaralioglu et al. (2001). First, in order to predict the amplitudes of vibration, we need to choose a damping coefficient. When $\hat{c} = 304$ Pa s/m, the vibration response compares well to the experimental curve, as seen in Figure 7.12. First, the experimental and predicted resonance frequencies are both about 7.54 MHz. Second, both resonance curves bend to the right because the CMUT is a hardening-type system ($\alpha_1 > 0$).

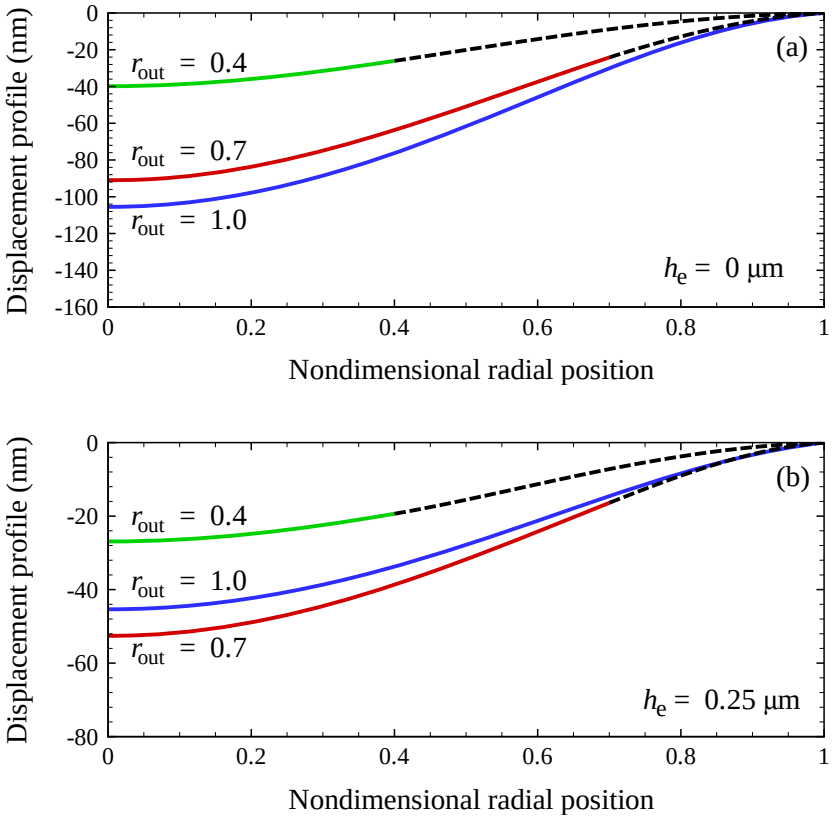

Figure 7.11: Displacement profile of the CMUT with a bias voltage of 80 V for (a) the electrode of zero thickness and (b) the 0.25 μm-thick electrode.

Despite the agreement between theory and experiment, the chosen damping coefficient must be physically realistic. Because the operating frequencies are in the megahertz range, the wavelength ($\sim 50\,\mu$m) of sound irradiated into the air is on the order of the active area of the CMUT ($\sim 50\,\mu$m). However, if the active area was much larger, the radiation impedance would be reduced to a pure resistive load (Caronti et al., 2002a); that is,

$$2\,\hat{c} \simeq \rho_{\text{air}}\, c_{\text{air}} \tag{7.103}$$

where ρ_{air} is the density of air and c_{air} is the speed of sound in air. For normal CMUT operating conditions, the specific acoustic impedance of air ($\rho_{\text{air}}\, c_{\text{air}}$) is about 400 Pa s/m (White, 1994), which means that $\hat{c} \simeq 200$ Pa s/m. Consequently, the fitted value of 304 Pa s/m is plausible.

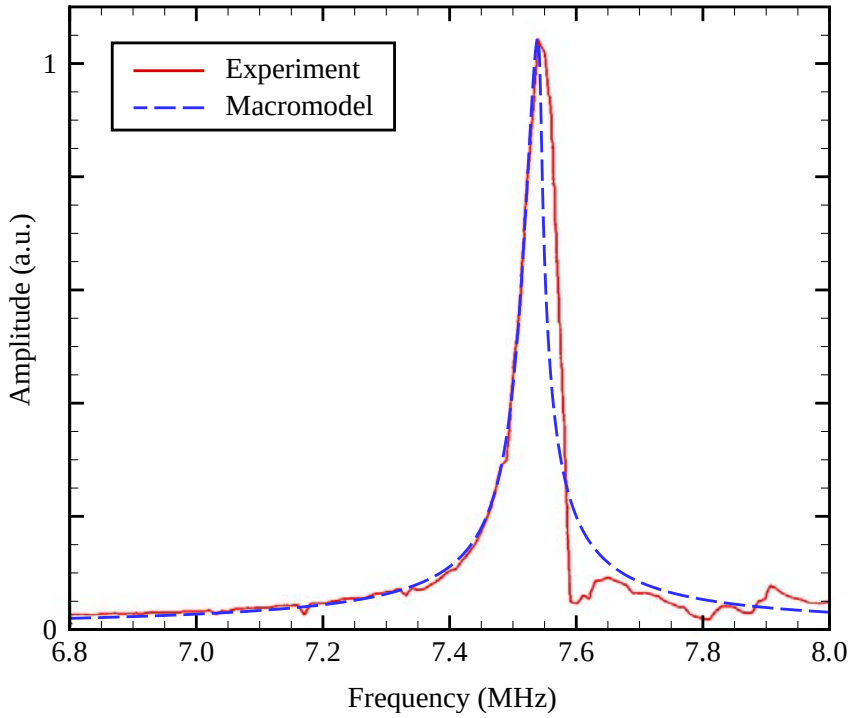

Figure 7.12: Amplitude of vibration versus driving frequency for the CMUT of Figure 7.4(a) with $\hat{\tau} = 124.5$ MPa and $E_{\mathrm{p}} = 255.4$ GPa. The FEM results were adapted from Yaralioglu et al. (2001) and $\hat{\tau} = 124.5$ MPa, $E_{\mathrm{p}} = 255.4$ GPa, and $\hat{c} = 304$ Pa s/m are used in the composite macromodel.

Chapter 8

Summary, Conclusions, and Recommendations for Future Work

In this chapter, we summarize the work presented in this Dissertation and present concluding remarks and recommendations for future work.

8.1 Summary and Conclusions

8.1.1 A Model of CMUTs under In-Plane and Electrostatic Forcings

We presented a new approach to the modeling and simulation of capacitive micromachined ultrasonic transducers (CMUTs) under the effects of in-plane loading, the inherent electrostatic forces, and pressure differences. The nonlinear governing equations were derived for a plate with an infinitesimally thin electrode and included the first geometric nonlinearity of the von Kármán type. The electrostatic term was regarded as a parallel-plate approximation and modes for a clamped-clamped case were then used in a Galerkin approach to obtain the governing system of differential equations. An approximate solution for the case of primary resonance excitation was then developed through utilization of the method of multiple scales (MMS).

For the first time, the axisymmetric nonlinear behavior of a vibrating CMUT was captured. Because of the use of MMS, nonlinear frequency-response curves can be generated

without resorting to finite element method (FEM) simulations. In fact, the transition of the CMUT from a hardening- to softening-type system up to pull-in was shown by the approximate solution. Furthermore, the static solution was also validated with experimental data and various design curves were generated to show how the reduced-order model can be used as an effective design tool.

8.1.2 An Updated Model with More Realistic Boundary Conditions

Because the response of CMUTs is highly influenced by the boundary conditions, an updated reduced-order model was developed to account for more realistic boundary conditions. Instead of using clamped-clamped conditions, we let the boundary force and moment affect the slope of the plate at the boundary in a linear manner. The electrode was still considered to be infinitesimally thin, but the electrode was allowed to have general inner and outer radii. The Galerkin approach was then utilized with an additional static solution and modes that transition from being sliding-clamped to sliding-simply-supported modes through the change of a boundary parameter. The resulting updated reduced-order model could be used to investigate the axisymmetric motion of CMUTs with relatively thin electrodes.

The updated reduced-order model was used to show the sensitivity of the pull-in voltage to the boundary conditions. The boundary parameters were extracted by matching the pull-in voltages from the macromodel to those from FEM simulations for CMUTs with varying outer and inner radii. The static behavior of the updated macromodel was validated because the pull-in voltages for the macromodel and FEM simulations were very close to each other and the extracted boundary parameters were physically realistic.

8.1.3 A Model of CMUTs that Accounts for Electrode Effects

A macromodel for CMUTs was then developed by including boundary effects and finite-thickness electrodes. First, we derived the equations governing the composite and non-composite regimes of the CMUT. This approach requires matching conditions between the composite and non-composite regimes at the interfaces of the inner and outer electrode boundaries. The matching conditions used ensure the continuity of displacements, slopes, forces, and moments from one regime to another, even though the internal stresses may be discon-

tinuous across the interfaces. Second, the Galerkin approach was used as before with the more realistic boundary conditions for the plate of the CMUT to obtain a comprehensive macromodel.

We attempted to validate this model with results from FEM simulations. For example, we used the variation of the center deflections of the CMUT with residual stress and the plate's Young's modulus to extract the two boundary parameters for the reduced-order model. In general, the center deflections obtained with the macromodel fell below those from the FEM simulation, especially for relatively high residual stresses, but the first natural frequencies that accompany the deflections were very close to those from the FEM simulations. Therefore, the composite macromodel might not be useful as an effective modeling tool with the current boundary conditions because the deflections may be severely underestimated. On the other hand, without the electrode effects included in the model, the CMUT deflection, pull-in voltages, and other characteristics are severely misrepresented. Furthermore, without a residual stress, the pull-in voltages and deflections obtained with the macromodel were close to FEM simulations for a CMUT with an embedded electrode. The forced vibration characteristics predicted with the macromodel also compared well with experimental data in which the primary resonance curve bends to the right because the CMUT is a hardening-type system.

8.2 Recommendations for Future Work

We recommend that the following work be done to advance the models presented in this Dissertation:

- The boundary conditions need to be updated to include nonlinear relationships between the plate forces and moments and boundary slope. Furthermore, the boundary should be allowed to deflect downward, perhaps linearly with forces and moments as a start of the investigation.

- Perhaps shear-deformation theory needs to be used, especially if models are desired that truly capture the details of how the CMUT frequencies change with electrode size.

- To account for electrostatic fringing fields, the parallel-plate approximation could be replaced by an approximation that accounts for fringing effects to the first order, which would allow the macromodel to better estimate CMUT behaviors for smaller electrodes.

- Experimental work needs to be conducted on CMUTs to establish the softening- and hardening-type regimes, characterize the static deflection, pull-in voltages and nonlinear vibrations, and collect data that can be used to update the macromodel.

- After the macromodel is significantly improved and the vibration response of one CMUT cell is better characterized, arrays of CMUTs should be investigated with the macromodel. The coupling of one cell to its neighbors could be achieved with linear approximations associated with behaviors at the plate boundaries. Consequently, non-axisymmetric boundary conditions could be included to account for CMUT neighbor-to-neighbor forcing.

- The first non-axisymmetric mode of vibration should be investigated, especially if the CMUTs are modeled as arrays, and any internal resonances should be taken into account with the method of multiple scales.

- The pressure difference across the composite plate should be coupled to the motion of the CMUT to investigate the coupling between the CMUT and its fluid environment.

Bibliography

Ahrens, O., Buhrdorf, A., Hohlfeld, D., Tebje, L., and Binder, J. Fabrication of gap-optimized CMUT. *IEEE Transactions on Ultrasonics, Ferroelectrics, and Frequency Control*, 49(9): 1321–1329, 2002.

Bayram, B., Yaralioglu, G. G., Ergun, A. S., and Khuri-Yakub, B. T. Influence of the electrode size and location on the performance of a CMUT. In *Proceedings of the 2001 IEEE Ultrasonics Symposium*, volume 2, pages 949–952, 2001.

Bayram, B., Hæggström, E., Yaralioglu, G. G., and Khuri-Yakub, B. T. A new regime for operating capacitive micromachined ultrasonic transducers. *IEEE Transactions on Ultrasonics, Ferroelectrics, and Frequency Control*, 50(9):1184–1190, 2003.

Bozkurt, A., Degertekin, F. L., Atalar, A., and Khuri-Yakub, B. T. Analytic modeling of loss and cross-coupling in capacitive micromachined ultrasonic transducers. In *Proceedings of the 1998 IEEE Ultrasonics Symposium*, volume 2, pages 1025–1028, 1998.

Bozkurt, A., Ladabaum, I., Atalar, A., and Khuri-Yakub, B. T. Theory and analysis of electrode size optimization for capacitive microfabricated ultrasonic transducers. *IEEE Transactions on Ultrasonics, Ferroelectrics, and Frequency Control*, 46(6):1364–1374, 1999.

Cadence Design Systems, Inc. *PSpice*. San Jose, CA.

Caliano, G., Galanello, F., Caronti, A., Carotenuto, R., and Pappalardo, M. Micromachined ultrasonic transducers using silicon nitride membrane fabrication in PECVD technology. In *Proceedings of the 2000 IEEE Ultrasonics Symposium*, volume 1, pages 963–968, 2000.

Caliano, G., Carotenuto, R., Caronti, A., and Pappalardo, M. cMUT echographic probes: design and fabrication process. In *Proceedings of the 2002 IEEE Ultrasonics Symposium*, volume 2, pages 1067–1070, 2002.

Caronti, A., Caliano, G., Iula, A., and Pappalardo, M. An accurate model for capacitive micromachined ultrasonic transducers. *IEEE Transactions on Ultrasonics, Ferroelectrics, and Frequency Control*, 49(2):159–168, 2002a.

Caronti, A., Majjad, H., Ballandras, S., Caliano, G., Carotenuto, R., Iula, A., Foglietti, V., and Pappalardo, M. Vibration maps of capacitive micromachined ultrasonic transducers by laser interferometry. *IEEE Transactions on Ultrasonics, Ferroelectrics, and Frequency Control*, 49(3):289–292, 2002b.

Caronti, A., Carotenuto, R., Caliano, G., and Pappalardo, M. The effects of membrane metallization in capacitive microfabricated ultrasonic transducers. *Journal of the Acoustical Society of America*, 115(2):651–657, 2004.

Cerjan, C., Kosloff, D., Kosloff, R., and Reshef, M. A nonreflecting boundary condition for discrete acoustic and elastic wave equations. *Geophysics*, 50(4):705–708, 1985.

Crescini, D., Marioli, D., and Taroni, A. Piezoelectric thick-film fluid density sensor based on resonance vibration. In *Proceedings of the 1998 IEEE Instrumentation and Measurement Technology Conference*, volume 2, pages 1368–1371, 1998.

Eccardt, P.-C., Niederer, K., Scheiter, T., and Hierold, C. Surface micromachined ultrasound transducers in CMOS technology. In *Proceedings of the 1996 IEEE Ultrasonics Symposium*, volume 2, pages 959–962, 1996.

Eccardt, P.-C., Niederer, K., and Fischer, B. Micromachined transducers for ultrasound applications. In *Proceedings of the 1997 IEEE Ultrasonics Symposium*, volume 2, pages 1609–1618, 1997.

Ergun, A. S., Cheng, C.-H., Demirci, U., and Khuri-Yakub, B. T. Fabrication and characterization of 1-dimensional and 2-dimensional capacitive micromachined ultrasonic transducer

(CMUT) arrays for 2-dimensional and volumetric ultrasonic imaging. In *Proceedings of the Oceans 2002 IEEE/MTS Conference*, volume 4, pages 2361–2367, 2002.

ESAOTE S.p.A. *Technos*. Genova, Italy.

Faris, W. F., Abdel-Rahman, E. M., and Nayfeh, A. H. Mechanical behavior of an electrostatically actuated micropump. In *Proceedings of the 43rd AIAA/ASME/ASCE/AHS/ASC Structures, Structural Dynamics, and Materials Conference*. AIAA Paper No. 2002-1303, 2002.

Haller, M. I. and Khuri-Yakub, B. T. A surface micromachined electrostatic ultrasonic air transducer. In *Proceedings of the 1994 IEEE Ultrasonics Symposium*, volume 2, pages 1241–44, 1994.

Haller, M. I. and Khuri-Yakub, B. T. A surface micromachined electrostatic ultrasonic air transducer. *IEEE Transactions on Ultrasonics, Ferroelectrics, and Frequency Control*, 43 (1):1–6, 1996.

Hansen, S. T., Turo, A., Degertekin, F. L., and Khuri-Yakub, B. T. Characterization of capacitive micromachined ultrasonic transducers in air using optical measurements. In *Proceedings of the 2000 IEEE Ultrasonics Symposium*, volume 1, pages 947–950, 2000.

Huang, Y., Ergun, A. S., Hæggström, E., and Khuri-Yakub, B. T. Fabrication of capacitive micromachined ultrasonic transducers (CMUTs) using wafer bonding technology for low frequency (10 kHz - 150 kHz) sonar applications. In *Proceedings of the Oceans 2002 IEEE/MTS Conference*, volume 4, pages 2322–2327, 2002.

Huang, Y., Ergun, A. S., Hæggström, E., Badi, M. H., and Khuri-Yakub, B. T. Fabricating capacitive micromachined ultrasonic transducers with wafer-bonding technology. *Journal of Microelectromechanical Systems*, 12(2):128–137, 2003a.

Huang, Y., Ergun, A. S., Hæggström, E., and Khuri-Yakub, B. T. New fabrication process for capacitive micromachined ultrasonic transducers. In *Proceedings of the 16th Annual IEEE International Conference on Micro Electro Mechanical Systems*, pages 522–525, 2003b.

Jin, X., Ladabaum, I., and Khuri-Yakub, B. T. The microfabrication of capacitive ultrasonic transducers. *Journal of Microelectromechanical Systems*, 7(3):295–302, 1998a.

Jin, X. C., Ladabaum, I., and Khuri-Yakub, B. T. Surface micromachined capacitive ultrasonic immersion transducers. In *Proceedings of the 11th Annual IEEE International Workshop on Micro Electro Mechanical Systems*, pages 649–654, 1998b.

Ladabaum, I., Khuri-Yakub, B. T., Spoliansky, D., and Haller, M. I. Micromachined ultrasonic tranducers (MUTs). In *Proceedings of the 1995 IEEE Ultrasonics Symposium*, volume 1, pages 501–504, 1995.

Ladabaum, I., Jin, X., Soh, H. T., Pierre, F., Atalar, A., and Khuri-Yakub, B. T. Microfabricated ultrasonic transducers: Towards robust models and immersion devices. In *Proceedings of the 1996 IEEE Ultrasonics Symposium*, volume 1, pages 335–338, 1996.

Ladabaum, I., Xuecheng Jin, Soh, H. T., Atalar, A., and Khuri-Yakub, B. T. Surface micromachined capacitive ultrasonic transducers. *IEEE Transactions on Ultrasonics, Ferroelectrics, and Frequency Control*, 45(3):678–690, 1998.

Larson, J. D. Non-ideal radiators in phased array transducers. In *Proceedings of the 1981 IEEE Ultrasonics Symposium*, pages 673–684, 1981.

Li, G. and Aluru, N. R. Linear, nonlinear, and mixed-regime analysis of electrostatic MEMS. *Sensors and Actuators A: Physical*, 91(3):278–291, 2001.

Lohfink, A., Eccardt, P.-C., Benecke, W., and Meixner, H. Derivation of a 1D CMUT model from FEM results for linear and nonlinear equivalent circuit simulation. In *Proceedings of the 2003 IEEE Ultrasonics Symposium*, volume 1, pages 465–468, 2003.

Mason, W. P. *Electromechanical Transducers and Wave Filters*, pages 181–184. Van Nostrand, New York, 2nd edition, 1948.

Mills, D. M. and Smith, L. S. Real-time *in-vivo* imaging with capacitive micromachined ultrasound transducer (cMUT) linear arrays. In *Proceedings of the 2003 IEEE Ultrasonics Symposium*, volume 1, pages 568–571, 2003.

Nayfeh, A. H. *Perturbation Methods*, pages 228–236. Wiley, New York, 1973.

Nayfeh, A. H. *Introduction to Perturbation Techniques*, pages 122–127. Wiley, New York, 1981.

Nayfeh, A. H. *Nonlinear Interactions: Analytical, Computational, and Experimental Methods*, page xvi. Wiley, New York, 2000.

Nayfeh, A. H. and Balachandran, B. *Applied Nonlinear Dynamics: Analytical, Computational, and Experimental Methods*, pages 449–454. Wiley, New York, 1995.

Nayfeh, A. H. and Mook, D. T. *Nonlinear Oscillations*, pages 366–367. Wiley, New York, 1979.

Nayfeh, A. H. and Pai, P. F. *Linear and Nonlinear Structural Mechanics*, pages 410, 502, 504, 505, 539. Wiley, New York, 2004.

Noble, R. A., Davies, R. R., King, D. O., Day, M. M., Jones, A. R. D., M^{c}Intosh, J. S., Hutchins, D. A., and Saul, P. Low-temperature micromachined cMUTs with fully-integrated analogue front-end electronics. In *Proceedings of the 2002 IEEE Ultrasonics Symposium*, volume 2, pages 1045–1050, 2002.

O'Neil, P. V. *Advanced Engineering Mathematics*, pages 252, 258, 261. Brooks/Cole Publishing, California, 1995.

Oppenheim, I. J., Jain, A., and Greve, D. W. Electrical characterization of coupled and uncoupled MEMS ultrasonic transducers. *IEEE Transactions on Ultrasonics, Ferroelectrics, and Frequency Control*, 50(3):297–304, 2003.

Osterberg, P. M. *Electrostatically Actuated Microelectromechanical Test Structures for Material Property Measurement*. PhD thesis, Massachusetts Institute of Technology, 1995.

Pelesko, J. A. Multiple solutions in electrostatic mems. In *Proceedings of the 2001 International Conference on Modeling and Simulation of Microsystems*, pages 290–293, 2001.

Perçin, G. and Khuri-Yakub, B. T. Piezoelectrically actuated flextensional MUTs. In *Proceedings of the 2001 IEEE Ultrasonics Symposium*, volume 2, pages 903–906, 2001.

Perçin, G. and Khuri-Yakub, B. T. Piezoelectrically actuated flextensional micromachined ultrasound transducers—I: Theory. *IEEE Transactions on Ultrasonics, Ferroelectrics, and Frequency Control*, 49(5):573–584, 2002.

Prak, A., Elwenspoek, M., and Fluitman, J. H. J. Selective mode excitation and detection of micromachined resonators. In *Proceedings of the 5th Annual IEEE International Workshop on Micro Electro Mechanical Systems*, pages 220–225, 1992.

Saggere, L., Hagood, N. W., Roberts, D. C., Li, H.-Q., Steyn, J. L., Turner, K., Carretero, J. A., Yaglioglu, O., Su, Y.-H., Mlcak, R., Spearing, S. M., Breuer, K. S., and Schmidt, M. A. Design, fabrication, and test of a piezoelectrically driven high flow rate micro-pump. In *Proceedings of the 12th IEEE International Symposium on Applications of Ferroelectrics*, volume 1, pages 297–300, 2000.

Suzuki, K., Higuchi, K., and Tanigawa, H. A silicon electrostatic ultrasonic transducer. *IEEE Transactions on Ultrasonics, Ferroelectrics, and Frequency Control*, 36(6):620–627, 1989.

Teng, M. F. and Hariz, A. J. Characterisation and modelling of MEMS ultrasonic transducers. In *Proceedings of the 2006 International MEMS Conference*, pages 949–954, 2006.

Ugural, A. C. and Fenster, S. K. *Advanced Strength and Applied Elasticity*, pages 194, 202, 219. Prentice-Hall PTR, New Jersey, 3rd edition, 1995.

Ventsel, E. and Krauthammer, T. *Thin Plates and Shells: Theory, Analysis, and Applications*, pages 7–8, 17, 40, 619. Marcel Dekker, Inc., New York, 2001.

Voorthuyzen, J. A., Sprenkels, A. J., Donk, A. G. H. V. D., Scheeper, P. R., and Bergveld, P. Optimization of capacitive microphone and pressure sensor performance by capacitor-electrode shaping. *Sensors and Actuators A: Physical*, 26:331–336, 1991.

White, F. M. *Fluid Mechanics*, pages 516, 701. McGraw-Hill, New York, 3rd edition, 1994.

Xuecheng Jin, Oralkan, Ö., Degertekin, F. L., and Khuri-Yakub, B. T. Characterization of one-dimensional capacitive micromachined ultrasonic immersion transducer arrays. *IEEE Transactions on Ultrasonics, Ferroelectrics, and Frequency Control*, 48(3):750–760, 2001.

Yaralioglu, G. G., Ergun, A. S., Bayram, B., Marentis, T., and Khuri-Yakub, B. T. Residual stress and Young's modulus measurement of capacitive micromachined ultrasonic transducer membranes. In *Proceedings of the 2001 IEEE Ultrasonics Symposium*, volume 2, pages 953–956, 2001.

Yaralioglu, G. G., Ergun, A. S., Bayram, B., Hæggström, E., and Khuri-Yakub, B. T. Calculation and measurement of electromechanical coupling coefficient of capacitive micromachined ultrasonic transducers. *IEEE Transactions on Ultrasonics, Ferroelectrics, and Frequency Control*, 50(4):449–456, 2003.

Younis, M. I., Abdel-Rahman, E. M., and Nayfeh, A. H. A reduced-order model for electrically actuated microbeam-based MEMS. *Journal of Microelectromechanical Systems*, 12(5):672–680, 2003.

Yu, M. and Balachandran, B. Sensor diaphragm under initial tension: Linear analysis. *Experimental Mechanics*, 45(2):123–129, 2005.

Vita

Gregory William Vogl received his B.S. and M.S. degrees in Engineering Science and Mechanics from Virginia Polytechnic Institute and State University in 2000 and 2003, respectively. He lived in Reston, Virginia most of his life, so attending Virginia Tech was only natural for this Virginian who wanted to learn and apply physics, mathematics, and engineering. No department felt like home for Gregory until he entered the Engineering Science and Mechanics Department.

For his Ph.D. degree in Engineering Mechanics, Gregory W. Vogl worked under the supervision of Dr. Ali H. Nayfeh in the areas of nonlinear dynamics and vibrations, with applications to microelectromechanical systems. His research interests include small-scale physics, nonlinear dynamics, and perturbation methods. Accordingly, Gregory W. Vogl will begin working in 2007 as a Postdoctoral Fellow under Dr. Jon R. Pratt at the National Institute of Standards and Technology (NIST) in Gaithersburg, Maryland. His postdoctoral research will focus on the nonlinear dynamics within atomic force microscopy.

Gregory W. Vogl considers his graduate work as a blessing and hopes that his future research will be even more rewarding.

AMDG